



HAL
open science

Use of mode coupling to enhance sound attenuation in acoustic ducts : effects of exceptional point

Lei Xiong

► **To cite this version:**

Lei Xiong. Use of mode coupling to enhance sound attenuation in acoustic ducts : effects of exceptional point. Acoustics [physics.class-ph]. Université du Maine, 2016. English. NNT : 2016LEMA1017 . tel-01402116

HAL Id: tel-01402116

<https://theses.hal.science/tel-01402116>

Submitted on 24 Nov 2016

HAL is a multi-disciplinary open access archive for the deposit and dissemination of scientific research documents, whether they are published or not. The documents may come from teaching and research institutions in France or abroad, or from public or private research centers.

L'archive ouverte pluridisciplinaire **HAL**, est destinée au dépôt et à la diffusion de documents scientifiques de niveau recherche, publiés ou non, émanant des établissements d'enseignement et de recherche français ou étrangers, des laboratoires publics ou privés.



FlowAirS



THÈSE DE DOCTORAT

Lei XIONG

Mémoire présenté en vue de l'obtention du
grade de Docteur de l'Université du Maine
sous le sceau de l'Université Bretagne Loire
École doctorale : SPIGA

Discipline : 60-Mécanique
Spécialité : Acoustique

Unité de recherche : Laboratoire d'Acoustique de l'Université du Maine - UMR CNRS 6613

Soutenue le 24^{er} mars 2016
Thèse N° : 84620

USE OF MODE COUPLING TO ENHANCE SOUND ATTENUATION IN ACOUSTIC DUCTS

Effects of exceptional point

JURY

Rapporteurs : **Jean-François MERCIER**, DR CNRS, Laboratoire POems (UMR 7231), ENSTA
Michel ROGER, Professeur, LMFA, Ecole Centrale de Lyon

Examineurs : **Emmanuel PERREY-DEBAIN**, Professeur, Laboratoire Roberval, UTC Compiègne
Hélène POSSON, Docteur, Airbus Operations S. A. S.

Directeur de thèse : **Yves AUREGAN**, DR CNRS, LAUM, Université du Maine

Co-encadrant de Thèse : **Wenping BI**, Maître de Conférences, LAUM, Université du Maine

ACKNOWLEDGEMENTS

I would like to thank my supervisors Yves Aurégan and Wenping Bi for the continuous support of my Ph.D study and related research. Their patience, enthusiasm, and guidance helped me a lot in the thesis work. Thanks to Bi's recommendation and Aurégan's acceptance, it was such a good luck for me to be a fellow in the European project : FlowAirS. This is how my journey begins! FlowAirS gave me the opportunity to meet people from different acoustic labs all over the Europe, and to have different trainings. Thanks also goes to all the FlowAirS fellows.

I am grateful to Jean-François MERCIER and Michel ROGER for having reviewed precisely this thesis and for their interests in this work. I would also like to thank other committee members : Emmanuel PERREY-DEBAIN and Hélène POSSON for their participation in my thesis defence. Their interesting questions and comments helped me to have a deeper understand about my work.

It was such a good opportunity for me to have the internship in Airbus, I greatly benefited from the support and encouragements of Hélène and Delphine, they guided me in the numerical investigations for the sound attenuation with metaporous, my sincere thanks also goes to all the group members.

The LAUM has provided the support and equipment I have needed to produce and complete my thesis. I also thank all the colleagues in LAUM. My special thanks goes to the director of the lab Joël Gilbert and the director of SPIGA Pierrick Lotton. I would like to express my special thanks to my previous colleague Balbine, who helped me a lot when I just arrived in France, and introduced me to French culture.

Professors Jun Fan and Qi Li have had an important presence in my Bachelor educational life, they encouraged me to seize the opportunity to study in France.

A special appreciation to my good friend and our good project manager Pauline Rasera, she helped me a lot for the complicated administrative papers, taught me French culture, and encouraged me to improve my French. Also, my sincere thanks to my dear friend Nanfei Wang, who continually and enormously encouraged and motivated me during my PhD study. I am also grateful to have the big Chinese family from Harbin in Le Mans, they helped me a lot during my stay in France.

Last but not the least, I would like to thank my family : my parents and to my brother for supporting me spiritually throughout my thesis work and my my life. I must acknowledge my boyfriend, Damien, who was always there supporting me and stood by me through the good times and bad.

Abstract

The central theme of this thesis is to use the mode coupling effects to enhance sound attenuation in acoustic ducts for potential applications, e.g. silencers for ventilation systems and wall treatments for aircraft engines. Two different strategies are presented.

The idea of the first strategy is to couple the incoming propagative mode in the waveguide with the mode localized in the scattering region. This strategy is presented and validated in an acoustic duct-cavity system and a waveguide partially lined with a locally reacting material. The R-matrix method is introduced to solve the propagation problems in the waveguides. It is shown that a zero in the transmission is present when a real resonance frequency of the open system, i.e. the cavity/lined portion (scattering region) which is coupled to the two semi-infinite rigid ducts, is equal to the incident frequency. This transmission zero occurs as a Fano resonance - due to the excitation of a trapped mode in the open system. This trapped mode is formed by the interferences of two neighbored modes with complex resonance frequencies. It is also linked to the avoided crossing of the eigenvalues and exceptional point (a point in a 2D parameter space, where not only the eigenvalues but also the eigenfunctions of a non-Hermitian operator coalesce). The scattering matrix is expressed in terms of a matrix H_{eff} which describes the complex resonances in the scattering region. With the aid of the eigenvalues and eigenfunctions of matrix H_{eff} , the traditional acoustic resonance scattering formula can be extended to describe the coupling effects between the scattering region and the rigid parts of the waveguide.

In the second strategy, a set of periodic rigid inclusions are embedded in a porous lining to enhance sound attenuation at low frequencies. The mode coupling is due to the presence of the embedded inclusions. Floquet-Bloch theorem is proposed to investigate the attenuation in a 2D periodic waveguide. Crossing is observed between the mode attenuations of two Bloch waves. The most important and interesting figure is that near the frequency where the crossing appears, an attenuation peak is observed. This phenomenon can be used to explain the transmission loss peak observed numerically and experimentally in a 3D waveguide with a portion of its wall lined by a porous material embedded with periodic inclusions.

Finally, the acoustical behaviours of a purely reacting liner in a rectangular duct in both absence and presence of flow are investigated. The results exhibit an unusual acoustical behaviour: for a certain range of frequencies, no wave can propagate against the flow. A negative group velocity is found in a certain range of frequencies, and it is demonstrated that the sound can be slowed down and even stopped.

Keywords

R-matrix method, Trapped mode, Fano resonance, Avoided crossing, Exceptional point, Sound attenuation, Bloch waves, Slow sound

Résumé

Le thème central de cette thèse est l'utilisation des effets de couplage de modes pour l'amplification de l'atténuation du son dans les conduits acoustiques. Les applications potentielles concernent les silencieux pour les systèmes de ventilation et les traitements de réacteurs pour l'aviation. Deux stratégies différentes sont présentées.

La première stratégie proposée est de coupler le mode incident propagatif dans le guide d'onde avec un mode localisé dans la région diffusivo. Cette stratégie est présentée et validée dans un système conduit-cavité et un guide d'onde partiellement traité en paroi avec un matériau à réaction locale. La méthode « R-matrix » est introduite pour résoudre le problème de propagation d'onde dans le guide d'onde. Une annulation de la transmission se produit quand un mode piégé est excité dans le système ouvert. Le zéro de transmission suivi immédiatement d'un pic de résonance forment une résonance de Fano. Ce mode piégé est formé par les interférences de deux modes voisins avec des fréquences de résonance complexes. Ce phénomène est aussi lié au croisement évité des valeurs propres et à un point exceptionnel (point dans un espace 2D où les valeurs propres et vecteurs propres d'un opérateur non-hermitien se confondent). La matrice de diffusion est exprimée en termes d'une matrice H_{eff} qui décrit les résonances complexes dans la région diffusivo. Avec l'aide des valeurs et fonctions propres de la matrice H_{eff} , la formule de diffusion résonante acoustique traditionnelle peut être étendue pour décrire les effets de couplage entre la région diffusivo et les parties rigides du guide d'onde.

Dans la seconde stratégie, un réseau d'inclusions rigides périodiques est intégré dans une couche poreuse pour améliorer l'atténuation du son à basse fréquence. Le couplage de modes est dû à la présence de ces inclusions. Le théorème de Floquet-Bloch est proposé pour analyser l'atténuation du son dans un guide d'onde périodique en 2D. Un croisement de l'atténuation de deux ondes de Bloch est observé. Au voisinage de la fréquence de croisement, un pic d'atténuation est observé. Ce phénomène est utilisé pour expliquer le pic de pertes en transmission observé expérimentalement et numériquement dans un guide 3D avec une portion de paroi traitée par un matériau poreux avec des inclusions périodiques.

Enfin, le comportement acoustique d'un liner purement réactif dans un conduit rectangulaire avec et sans écoulement est étudié. Les résultats montrent un comportement acoustique inhabituel : dans une certaine gamme de fréquence, aucune onde ne peut se propager à contre sens de l'écoulement. Par analyse des différents modes à l'aide de la relation de dispersion, il est démontré que le son peut être ralenti et même arrêté.

Mots-clés

Méthode R-matrix, Mode piégé, Résonance de Fano, Croisement évité, Point exceptionnel, Atténuation du son, Ondes de Bloch, Son lent

Contents

Nomenclature	iii
1 General introduction	1
1.1 Background	1
1.2 Trapped modes	3
1.3 Exceptional points and avoided crossings: a simple illustration example . .	5
1.4 Exceptional points and avoided crossings: applications in lined waveguides	9
1.5 Fano resonance	11
1.6 R-matrix method	17
1.7 Thesis organization	17
2 Fano resonance scattering in a duct-cavity system	25
2.1 Introduction	25
2.2 Formulation and method of the problem	27
2.2.1 R-matrix method	29
2.2.2 Matrix H_{eff}	30
2.3 Results and discussions	32
2.3.1 Degeneracy and avoided crossing	32
2.3.2 Trapped mode and Fano resonance	35
2.3.3 Multimodes interference	37
2.4 Conclusions	39
Appendices	40
2.A Derivation of Eqs.(2.9)(2.10)(2.12)	40
2.A.1 Derivation of Eq. (2.9)	40
2.A.2 Derivation of Eq. (2.10)	40
2.A.3 Derivation of Eq. (2.12)	41
3 Fano resonance scatterings in waveguides with impedance boundary conditions	47
3.1 Introduction	48
3.2 Model	49
3.3 Results and discussions	54

3.4	Conclusions	60
4	Use of metaporous materials in acoustic ducts	67
4.1	Introduction	67
4.2	Description of the problem	69
4.2.1	Experimental setup	69
4.2.2	Measuring technique	70
4.2.3	Description of the configurations	72
4.2.4	Numerical method	74
4.3	2D simple model analysis	74
4.3.1	Problem statement	74
4.3.2	Bloch waves and eigenvalue problems	76
4.3.3	Effects of inclusions and porous material	78
4.4	3D numerical and experimental results	84
4.4.1	Numerical results	85
4.4.2	Experimental results for the configurations with R1	87
4.4.3	Experimental results for the configurations with R2	92
4.4.4	Comparison between numerical and experimental results	96
4.5	Conclusions	97
	Appendices	98
4.A	Equivalent fluid model	98
4.B	Eigenvalue problem in a porous lined duct	98
4.C	Scattering matrix of a unit cell	100
5	Acoustical behavior of purely reacting liners	107
5.1	Introduction	107
5.2	Propagation in the reacting lined ducts without flow	108
5.2.1	Modes in the lined ducts without flow	108
5.2.2	Scattering matrix	113
5.3	Propagation in the lined ducts with uniform flow	115
5.3.1	Basic equations	115
5.3.2	Uniform flow	117
5.4	Propagation in the lined ducts with shear flow	119
5.4.1	Modes in the rigid duct with shear flow	121
5.4.2	Modes in the lined duct with shear flow	122
5.4.3	The effect of the boundary layer thickness	123
5.4.4	Transmission and reflection in the lined liner with shear flow . . .	125
5.5	Conclusion	127
	Appendices	127
5.A	The admittance of the liner	127
5.B	Scattering matrix S	129
5.C	Ingard-Myers boundary condition	130

6 Conclusions

Chapter 1

General introduction

1.1 Background

Acoustic liners [1] are widely used in ducts to reduce aircraft engine noise emission. Two main different acoustic liners are commonly used: the locally-reacting liner and the bulk-reacting liner. The locally reacting liners are generally made with a perforated sheet backed by honeycomb and permit propagation only in the direction normal to the duct wall. This kind of materials have good absorption properties only in a narrow frequency band but their main advantages are their mechanical robustness and their capability to resist to harsh conditions. Bulk-reacting liners may consist of isotropic or anisotropic porous material. They generally offer a wider absorption/attenuation band. However, they suffer from a lack of absorption efficiency at low frequencies, comparing to their efficiency at higher frequencies.

The use of uniform acoustic duct liners to suppress the noise is well established, research efforts have been focused on the prediction of the acoustic liner performances and the design of optimum liners. The minimum transmission (maximum attenuation) coefficient for each mode in an infinite uniform waveguide or in a duct lined with locally reactive impedance, is Cremer's optimum attenuation [2]. The corresponding lined impedance is called Cremer's optimum impedance. Each mode has one and only one corresponding optimum impedance [3, 4], in the absence of mean flow or with uniform flow [3]. Soon after, axially and circumferentially segmented liners have also been considered in the design of more effective noise-attenuation systems, for review, see for example Refs. [5, 6, 7] and references therein. The basic idea of these non-uniform liners is: one less attenuated mode may be scattered into higher attenuated modes at the non-uniform parts (interfaces) by mode couplings.

To date, due to the growth of fan diameter, the reduction of the rotation speed and of the number of blades, sound attenuation at low frequencies still represents a challenge. To solve that problem, other approaches must be investigated and new concepts of acoustic absorbers dedicated to the reduction of turbomachinery noise must be developed.

Motivated by this situation, the objective of this thesis is to use some new mechanisms to reduce sound transmission or improve the sound attenuation in acoustic ducts. Two different strategies will be presented.

For the first strategy, we will focus on the coherent mode couplings in a duct-cavity system and in a rigid duct partially treated with uniform locally reacting liner, and their effects on the sound propagation behaviours. The idea is to use the interference effect between the incoming propagative mode in the rigid regions and the trapped mode in the cavity/lined region, to produce a transmission zero or a narrow band of dip. This trapped mode localises in the lined/cavity region, which is regarded as an open cavity opened to the infinities through the rigid regions, in both transverse and axial directions, and it is also called (real or complex) resonance. We will use trapped mode(s) or resonance(s) alternatively in this thesis. In the point of view of resonance, the above mentioned interference effect is a resonance scattering process. In contrast to the usual resonance scattering (see, e.g., Uberall [8]), the interferences between the incoming wave and local resonance produce a Fano resonance. As trapped mode, Fano resonances are some relatively new concepts in acoustics, and we will show, in this thesis, that they are closely connected with “exceptional points” and “avoided crossings”. We will explain these concepts by some simple examples in the following sections.

In the second strategy, to improve the liner efficiency at low frequencies, material including periodic subwavelength resonators are studied in analogy to optical metamaterials [9, 10, 11]. In this view, metaporous materials, made of periodic rigid inclusions embedded in the porous medium, have been proposed to enhance the absorption properties at frequencies lower than the quarter wavelength frequency [12, 13]. The principle is that the energy is trapped between periodic rigid inclusions embedded in the porous medium and the rigid backing or in the inclusions themselves. In the second strategy, we deal with the bulk-reacting liner. The coupling of the modes due to the presence of the rigid inclusions embedded in the porous material is investigated and introduced to enhance the sound attenuation in the waveguide at low frequencies.

The use of periodic inclusion in the waveguide has also been studied by Nennig *et al.* [14]. The Floquet-Bloch theorem is used to reduce the computation on one periodic cell. It has been shown that open shape inclusions (e.g. U-shape) are able to enhance the attenuation when compared with a homogeneous liner. Thanks to Floquet-Bloch formalism assuming periodic heterogeneities [12, 13, 14, 15], very interesting results have been obtained in acoustics. The Floquet theorem is applicable to ordinary differential equations with periodic coefficients and shows that the solutions are such that

$$\psi(x + L_0) = e^{jk_B L_0} \psi(x),$$

where L_0 is the period of the coefficients, k_B is the Bloch wave number, and x is the propagation axis. Such functions are known as Bloch wave functions.

1.2 Trapped modes

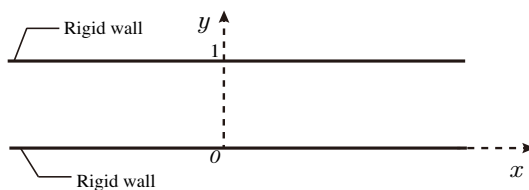


Figure 1.1: A 2D uniform rigid duct.

Transverse modes in a 2D uniform (coordinate (x, y)) normalized rigid duct (see Fig. 1.1) can be defined by

$$\frac{\partial \phi(y)}{\partial y} = -\alpha^2 \phi(y), \quad (1.1)$$

with boundary conditions

$$\left. \frac{\partial \phi(y)}{\partial y} \right|_{y=0,1} = 0. \quad (1.2)$$

The solutions are

$$\phi_n(y) = \Lambda \cos(\alpha_n y) \text{ and } \alpha_n = n\pi \text{ with } \Lambda = 1 \text{ if } n = 0, \text{ else } \sqrt{2}, \quad (1.3)$$

where $n = 0, 1, 2, \dots$, n labels the mode. In the infinite uniform waveguide ($x \rightarrow \pm\infty$), waves $p(x, y)$ with transverse modes $\phi_n(y)$ and wavenumber in x -direction k_n^x propagate as

$$p(x, y) = \phi_n(y) e^{-j\omega t \pm jk_n^x x}, \quad (1.4)$$

where $k_n^x = \sqrt{k^2 - \alpha_n^2}$.

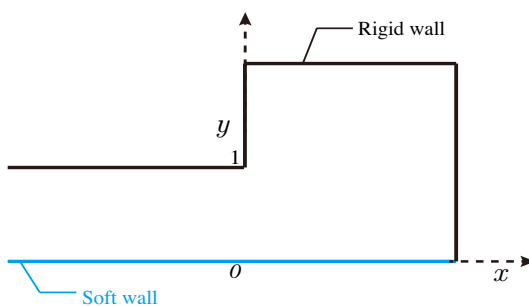


Figure 1.2: A 2D open system, where the bottom wall is soft and the others are rigid.

However, some open systems (see e.g. Fig. 1.2) may sustain such kind of mode, which mathematically corresponds to real eigenvalues of the relevant operator in an unbounded domain. In the literature, they are often called “trapped modes” to stress

their localization properties in open system. They are also called bound states in quantum mechanics [16]. If a part of energy is radiated to the infinity, the eigenvalues are complex, they are also called complex resonances in open cavities or leaky modes in waveguides [17]. Therefore, discrete trapped modes with eigenfunctions $\varphi(x, y)$ and *real* eigenvalues k , which satisfy eigenvalue problem

$$\partial^2 \varphi / \partial x^2 + \partial^2 \varphi / \partial y^2 = -k^2 \varphi \quad (1.5)$$

and boundary conditions along y and radiation conditions along x , and have finite energy,

$$\iint_s dy \int_{-\infty}^{\infty} dx |\varphi|^2 \text{ is finite,} \quad (1.6)$$

where s is waveguide cross section, in general do not exist. However, discrete trapped modes may exist below the first cut-off frequency of the transverse modes (e.g. in waveguides with pressure release boundary conditions (Dirichlet waveguides, see e.g. Fig. 1.3), or antisymmetric transverse modes in rigid waveguides (Neumann waveguides)), provided some kinds of defect or variations of geometry exist [17, 18]. Discrete trapped modes may also exist above the first cut-off frequency for specific parameter combinations, called embedded trapped modes or bound states in continuum (BIC) in quantum mechanics [19]. Here “continuum” means the eigenvalues (or spectrum in maths and quantum mechanics) k are distributed continuously and the corresponding eigenfunctions are in general not square integrable due to the radiation of energy to infinity. Although BIC are embedded in continuum spectrum, their eigenfunctions are still square integrable, i.e., their energy is finite. The basic mechanism of trapping is illustrated by using a simple model of the potential well by Pagneux [18].

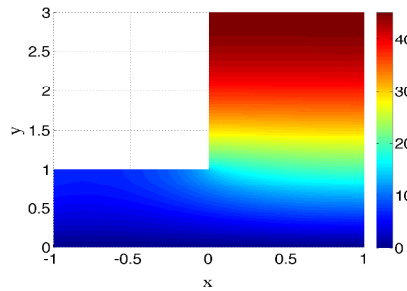


Figure 1.3: An example of trapped in a semi-infinite system (see Fig. 1.2), with Dirichlet condition on the bottom wall and rigid boundary conditions on the other walls.

The existence of trapped mode problem in the waveguides has been investigated by many authors in various physical contexts theoretically and experimentally. In locally-perturbed acoustic waveguides, it was first observed experimentally by Parker in 1966 [20],

who also made the first theoretical calculations of resonance frequencies (eigenvalues of trapped modes, in this thesis, we will use resonance or trapped mode alternatively) in the following year [21]. Since then, more investigations have been done, for example, embedded trapped mode frequencies for a variety of configurations have been calculated by Duan *et al.* [17]. Recently, S. Hein *et al.* [22] used the finite-element method to numerically compute the acoustic resonances in 2D acoustical duct-cavity systems. Three types of trapped modes are introduced: antisymmetric (about duct axis) trapped modes below the first cut-off frequency, embedded trapped modes linking with avoided crossings of resonances, and trapped modes associated with Fabry-Pérot interference between cavities. The second type of trapped mode is of our first interest, see chapters 2 and 3.

Trapped modes (resonances, or BIC) may be linked closely with avoided crossings of eigenvalues and Exceptional Points (EPs)[23, 24]. By Feshbach's theory of resonance, Friedrich and Wintgen [25] demonstrated that BICs in atomic physics can occur, due to the interference of resonance belonging to different channels. By varying a continuous parameter, avoided crossings of resonances are observed. At a particular value of the parameter, one resonance has exactly vanishing width and becomes a BIC, the same phenomena are also observed in acoustical duct-cavity system and acoustic lined duct, see Chap. 2 and Chap. 3, respectively. In quantum systems, Almas F. Sadreev *et al.* [26] showed that the BIC also appears in open quantum billiards by varying their shape continuously. They also found that the BICs are close to the points of *degeneracy* [27] of the closed quantum system, which are the points in a two-dimensional parameter space where only the eigenvalues coalesce, while the corresponding eigenfunctions are still orthogonal. When the system is opened by attaching to two infinite leads, the coupling of the two resonances is turned on, an *avoided crossing* occurs with the variation of the parameters [24]. This avoided crossing is associated with the *Exceptional Points*(EPs) in the parameter plane. At the EPs, the two resonances will coalesce, not only the eigenvalues but also the eigenfunctions [23, 24]. An example about the existence of EP in acoustics is the Cremer's optimum impedance, see Chap.1.4 in the following.

1.3 Exceptional points and avoided crossings: a simple illustration example

We consider the simple example (see Fig. 1.4), two pendulums with the same mass m are coupled through a spring k . The length l of the unperturbed pendulum is changed for the second pendulum to the value $l(1 + \sigma)$. The force on pendulum 1 in the direction of motion due to the coupling is $-kl(\theta_1 - (1 + \sigma)\theta_2)$ and the force on pendulum 2 due to the coupling is $-kl((1 + \sigma)\theta_2 - \theta_1)$. The differential equations for the angular motions

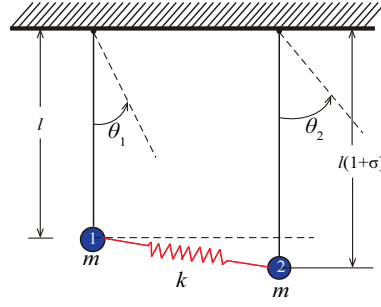


Figure 1.4: Schematic view of two coupled pendulums

θ_1 and θ_2 become

$$\begin{aligned} \frac{d^2}{dt^2}\theta_1 + \omega_1^2\theta_1 + \frac{k}{m}\theta_1 - \frac{k}{m}(1+\sigma)\theta_2 &= 0, \\ \frac{d^2}{dt^2}\theta_2 + \omega_2^2\theta_2 + \frac{k}{m}\theta_2 - \frac{k}{m}\frac{1}{(1+\sigma)}\theta_1 &= 0, \end{aligned} \quad (1.7)$$

where $\omega_1 = \sqrt{\frac{g}{l}}$ and $\omega_2 = \sqrt{\frac{g}{l(1+\sigma)}}$ are the natural frequencies of the two uncoupled pendulums. The differential equations can be written in a matrix form

$$\frac{d^2}{dt^2}\vec{\theta} + \mathbf{H}\vec{\theta} = 0, \quad (1.8)$$

where

$$\mathbf{H} = \mathbf{H}_0 + \frac{k}{m}\mathbf{H}_1 = \begin{bmatrix} \omega_1^2 & 0 \\ 0 & \omega_2^2 \end{bmatrix} + \frac{k}{m} \begin{bmatrix} 1 & -(1+\sigma) \\ -\frac{1}{1+\sigma} & 1 \end{bmatrix} \quad (1.9)$$

with \mathbf{H}_1 the coupling matrix due to the presence of the spring. The eigenvalues λ are the solutions of

$$\mathbf{H}\vec{\theta}_n = \lambda_n\vec{\theta}_n, \text{ i.e., } \Delta(\lambda, \sigma) = \det(\mathbf{H} - \lambda\mathbf{I}),$$

where $n = 1, 2$, $\lambda = \omega^2$, and \mathbf{I} is the identity matrix.

When there is no coupling between the two pendulums, i.e. $k = 0$, the two eigenvalues coalesce if

$$\Delta(\lambda, \sigma) = (\omega_1^2 - \lambda)(\omega_2^2 - \lambda) = 0 \text{ and } \partial\Delta(\lambda, \sigma)/\partial\lambda = 0.$$

We find that at $\sigma = 0$, $\lambda_{1,2} = \omega_1^2 = g/l$. This is called a degeneracy [27]. The two eigenvalues coalesce, while the two eigenfunctions, such as $\cos\omega_1 t$ and $\sin\omega_1 t$, are orthogonal.

When $k \neq 0$, there is coupling between the two pendulums, the eigenvalues are

$$\lambda_{1,2} = \frac{1}{2} \left[\omega_1^2 + \omega_2^2 + 2\frac{k}{m} \pm R_c \right], \quad \text{with } R_c = \sqrt{\omega_1^4 + \omega_2^4 - 2\omega_1^2\omega_2^2 + 4\left(\frac{k}{m}\right)^2}. \quad (1.10)$$

We can see that when $R_c \neq 0$, there exists avoided crossing between the two eigenval-

ues(see Figs. 1.5 and 1.6). However, the two eigenvalues will coalesce if $R_c = 0$, this occurs at the two complex conjugate σ (Here the $\sigma = \sigma_r + i\sigma_i$ has been assumed to be analytically continued in the complex plane). We can find that at

$$\sigma_{ep} = \frac{-4C^4 \pm j2C^2}{1 + 4C^4}, \quad (1.11)$$

we have

$$\lambda_{ep} = \frac{1}{2} \left[\omega_1^2 + \omega_2^2 + 2\frac{k}{m} \right], \quad (1.12)$$

where $C^2 = \frac{k/m}{g/l}$ is the coupling strength. σ_{ep} is an exceptional point (EP) in the complex parameter plane σ , where we have $\lambda_1 = \lambda_2 = \lambda_{ep}$.

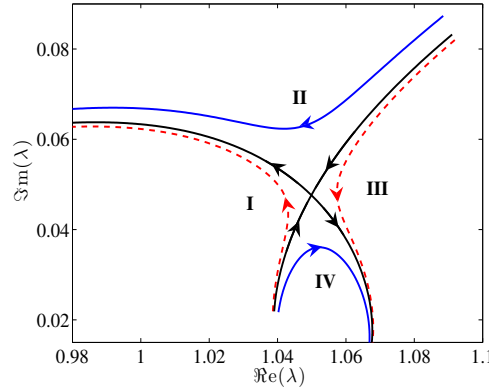


Figure 1.5: Trajectories of the eigenvalues in the complex plane with three different σ_i , i.e., -0.2 (II and IV), -0.19 (I and III), and $\Im\text{m}(\sigma_{ep})$ (crossing), respectively. Arrows indicate the increase with σ_r . The other parameters are $\omega_1 = 1$ and $k/m = 0.1$.

As an example, we choose $\omega_1 = 1$ and $k/m = 0.1$, leading to $\sigma_{ep} = -0.0385 \pm j0.1923$. We present a topological argument why either the real parts or the imaginary parts must cross when eigenvalue trajectories pass the vicinity of an EP [24]. When $\sigma_i (= -0.2) < \Im\text{m}(\sigma_{ep})$, crossing for the real parts and avoided crossing for the imaginary are observed, (II and IV in Fig. 1.5). While when $\sigma_i (= -0.19) > \Im\text{m}(\sigma_{ep})$, avoided crossing for the real parts and crossing for the imaginary are observed, (I and III in Fig. 1.5). Only in the special case ($\sigma_i = \Im\text{m}(\sigma_{ep})$) where the parameter σ moves straight through an EP will both, the real and imaginary part, cross. Using this crossing, we can divide the complex plane into four quadrants, labelled by I, II, III, and IV in Fig. 1.5, respectively.

The details of the crossings and avoided crossings in Fig. 1.5 are also considered again in Fig. 1.6, in which we plot the real and imaginary parts of the eigenvalues $\lambda_{1,2}$ as a function of the real parameter σ_r for two different values of σ_i (-0.2 (upper figure) and -0.19 (bottom figure), respectively). Crossing is observed for the real part with

$\sigma_i = -0.2$, while for the imaginary part with $\sigma_i = -0.19$. Other choices lead qualitatively to the same result. From Eq. (1.11), the σ_{ep} is a complex conjugate pair. The other σ_{ep} can also have the same effects on λ by taking $\sigma_i = 0.19$ and 0.2 .

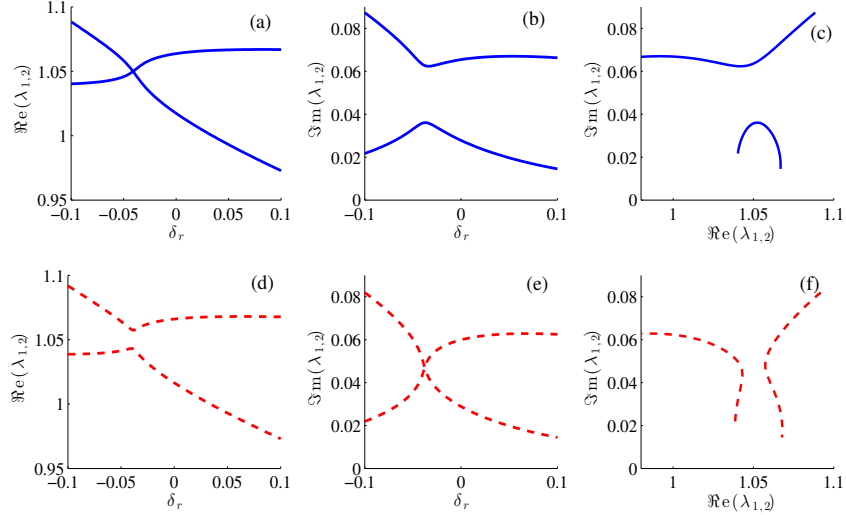


Figure 1.6: Eigenvalues $\lambda_{1,2}$ as a function of $\sigma_r (\in [-0.1, 0.1])$ with (a)(b)(c) $\sigma_i = -0.2$ and (d)(e)(f) $\sigma_i = -0.19$. The other parameters are $\omega_1 = 1$ and $k/m = 0.1$. Figures (c) and (f) give the trajectories of the eigenvalues in the complex plane.

Exceptional points were first introduced by Kato [28], and were extensively developed by Heiss [23, 24, 29], Rotter [30, 31, 32], and Berry [33]. Extensions of this concepts in acoustics is shown in [34]. The mathematically topological structures of Riemann sheets of an EP, which are a square root branch point of the coalescing eigenvalues and a fourth-order branch point of the coalescing eigenfunctions depending on a complex or two real parameters, have been proved physical reality [35]. EPs have attracted much attention in non-Hermitian Hamiltonian quantum and optical systems (see, e.g. Refs. 30, 36 and the references therein). They have been found in different domains: laser-induced ionization states of atoms [37], atom waves in crystals of light [38], electronic circuits [39], atoms in cross magnetic and electric fields [40], and in microwave billiards [41]. Experiments in laboratories have been carried out with resonances in microwave cavities [35, 41, 42].

EPs are closely related to avoided crossings of eigenvalue curves. If the parameter σ is real, the system \mathbf{H} in Eq. (1.9) is Hermitian. The typical behaviour of the eigenvalues of matrix \mathbf{H} as a function of real σ when they approach each other, is repulsion, or an avoided crossing. This is the famous rule of von Neumann and Wigner [43] in quantum mechanics who proved that in systems without any symmetry we have to vary two parameters in order to create a (conventional) degeneracy. The analytic continuation into the complex σ -plane yields a complex conjugate pair of EPs where the two coalescing

modes are analytically connected by a square root branch point [29]. Avoided crossings of eigenvalues play an important role in quantum mechanics [44]. They have been also found in the area of structural dynamics [45, 46, 47] and related to mode localization in disordered structures [48, 49]. In Chap. 4, we will see that they also play an important role in the sound attenuation in a waveguide lined by a porous material embedded with periodic inclusions. A maximum sound attenuation is observed near a crossing (or avoided crossing) of the mode attenuations between two Bloch waves.

1.4 Exceptional points and avoided crossings: applications in lined waveguides

In the following, we will see that for the applications in the lined intakes of an aero-engine, EP [34] exists in complex admittance (impedance) plane and plays an important role in the sound attenuation [34]. An example of the EPs in acoustics is the Cremer's optimum impedance. The Helmholtz equation

$$\frac{\partial^2 \psi}{\partial y^2} + k_y^2 \psi = 0 \quad (1.13)$$

of transverse eigenfunction $\psi(y)$ in an infinite lined duct of normalized height $h = 1$ with boundary conditions

$$\left. \frac{\partial \psi(y)}{\partial y} \right|_{y=0} = -jKY \psi(0) \text{ and } \left. \frac{\partial \psi(y)}{\partial y} \right|_{y=1} = 0 \quad (1.14)$$

is solved by Multimodal Method [50, 51], where k_y is the corresponding eigenvalue. Function $\psi(y)$ is projected in the basis of the rigid modes (Eq. (1.3))

$$\psi_y(y) = \sum A_n \phi_n(y).$$

Multiplying the Helmholtz equation of $\psi(y)$ by $\phi_n(y)$ on both sides, and then integrating with respect to y over $[0, 1]$, we can write the upper eigenvalue problem in a matrix form

$$k_y^2 \vec{A} = \Gamma \vec{A} - jKY \cdot \mathbf{M} \vec{A},$$

where $M_{mn} = \phi_m(0)\phi_n(0)$, and Γ is a diagonal matrix with elements α_n^2 . The eigenvalue problem of the lined waveguide can be regard as solving the eigenvalue problem of the matrix

$$\mathbf{H} = \Gamma - jKY \mathbf{M}. \quad (1.15)$$

By Eq. (1.15), we can study the influence of the admittance on the wavenumber k_y . For the simplification, we treat the product $K \cdot Y$ as one parameter KY . Referring to

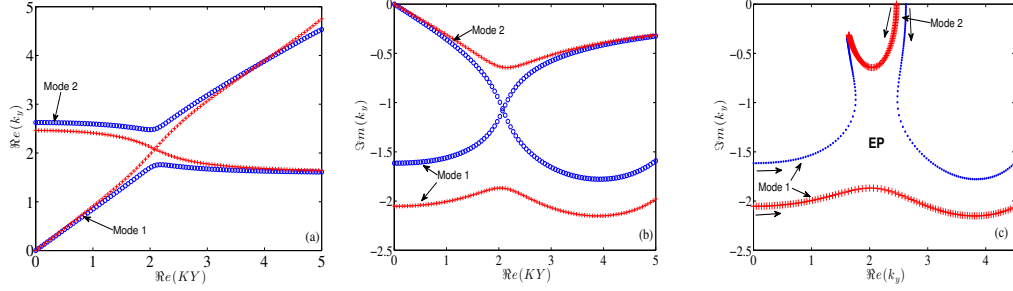


Figure 1.7: (a) Real and (b) imaginary part of wavenumbers k_y of the first 2 modes (labeled by “Mode1” and “Mode2”, respectively) as a function of $\Re e(KY)$ under two different values of $\Im m(KY) = -1.5$ (‘*’) and -2 (‘+’) respectively. (c) Trajectories of the wavenumber in complex plan, arrow shows the direction of the movements with increasing the real part of KY .

the work of F. P. Mechel [4], the first two exceptional points for the first three modes are $KY_{EP1} = 2.05998 - j1.65061$ and $KY_{EP2} = 5.33471 - j2.05785$, with $\exp(-j\omega t)$ considered. Here, the first point is investigated, i.e. the behaviours of the first two eigenvalues are considered. In Fig. 1.7, we show the motions of the first two eigenvalues k_y (labeled by “Mode1” and “Mode2”, respectively) as a function of $\Re e(KY)$ under two different values of $\Im m(KY)$. The amplitude of its eigenfunction from the decreases exponentially away from the lined wall, which is $\propto \exp(-|k_y|y)$. With increasing the absolute value of $\Im m(KY)$, the $|k_y|$ will increase, resulting in that the eigenfunction of transverse mode decreases faster from the lined wall, these properties are also discussed in Chap. 5 of this thesis.

Two corresponding different kind of avoided crossings are found in Fig. 1.7 for $\Im m(KY) = -1.5$ and -2 , respectively. The transition of the two types of avoided crossings indicates that there exist an exceptional value of $(\Re e(KY), \Im m(KY))$, at which the two eigenvalues curves will coalesce, this value is called the Exceptional Point (EP) in the complex KY parameter plane. To see the EP location in the parameter plane clearly, the real and imaginary parts of k_y as a function of both $\Re e(KY)$ and $\Im m(KY)$ are also given, see Fig. 1.8. We can see that the two eigenvalues are the values of one single analytical function on two Riemann sheets. The point $(k_{y1} = k_{y2})$ is called branch point singularity [23].

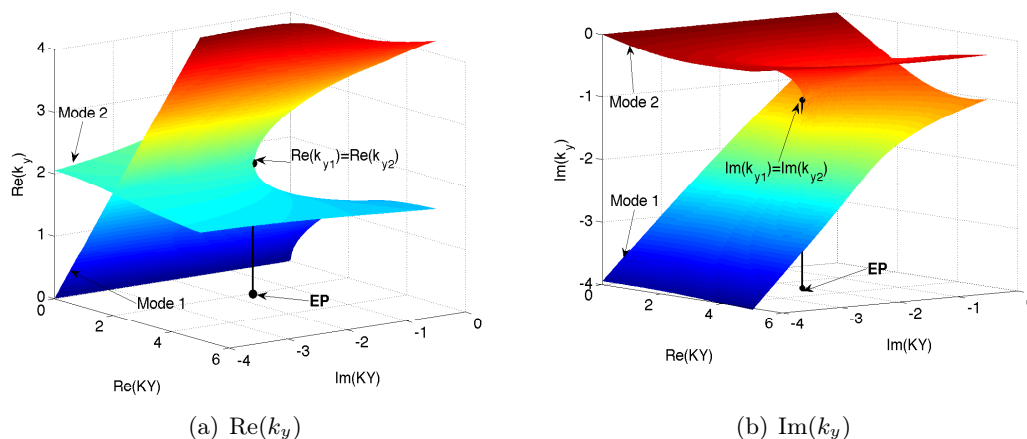


Figure 1.8: Eigenvalue surfaces of the first 2 in that complex KY plane: (a) real and (b) imaginary parts of k_y . The EP is located in the complex KY plane, at where the two eigenvalues coalesce.

1.5 Fano resonance

Fano resonance was firstly suggested by Ugo Fano [52] for the description of autoionizing atomic states. In contrast to the conventional isolated resonances, e.g., resonance in a harmonic oscillator with periodic forcing, for which the spectral dependence can be described by the Lorentzian or Breit-Wigner formula – a symmetric spectral line; Fano resonance was explained as a phenomenon of constructive and destructive interferences between a bound state and the continuum [52, 53]. The corresponding spectral lines are asymmetric. Since its discovery, Fano resonance has been attracting much attention in different research fields, for review articles see, for example, [54, 55] and the references therein. Fano resonances have been observed experimentally in different domains of physics [54, 55]. Extensive studies were carried out in Fano resonance induced by the interferences between bound states (or quasi-bound states, complex resonances) and the continuum, or between quasi-bound states through the continuum, for example, see Refs. 56, 57, 58, 59, 60, 61. Fano resonance in acoustic scattering and their relations with trapped modes in waveguides including obstacles or in duct-cavity systems have been studied by Hein *et al.* [22, 62].

Y. Joe *et al.* [53] gave a classical analogy of appearance of the Fano resonances based on a simple harmonic oscillator system model. In this section, the same system as used in Sec. 1.3 is applied here to give the explanation of the physical nature of Fano resonance. The equations of angular motion for the two coupled pendulums with an external driving

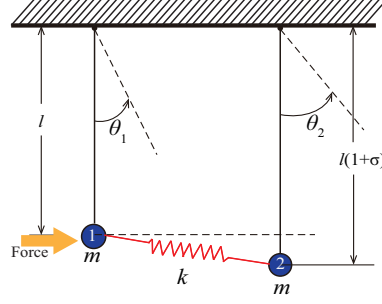


Figure 1.9: Schematic view of two coupled pendulums with a driving force applied to one of them.

force on pendulum 1 may be written as

$$\begin{aligned} \frac{d^2}{dt^2}\theta_1 + \omega_1^2\theta_1 + \frac{k}{m}\theta_1 - \frac{k}{m}(1+\sigma)\theta_2 &= a_1 e^{j\omega t}, \quad \text{and} \\ \frac{d^2}{dt^2}\theta_2 + \omega_2^2\theta_2 + \frac{k}{m}\theta_2 - \frac{k}{m}\frac{1}{(1+\sigma)}\theta_1 &= 0, \end{aligned} \quad (1.16)$$

where $a_1 e^{-j\omega t}$ written in a complex form is the term due to the external force. After some manipulation, one can obtain that the steady-state solutions for the angular of the pendulums are also harmonic such that

$$\theta_1 = c_1 e^{-j\omega t}, \quad \theta_2 = c_2 e^{-j\omega t}.$$

The amplitudes are

$$c_1 = \frac{(\omega_2^2 - \omega^2 + \frac{k}{m})}{(\omega_1^2 - \omega^2 + \frac{k}{m})(\omega_2^2 - \omega^2 + \frac{k}{m}) - (\frac{k}{m})^2} a_1, \quad (1.17)$$

$$c_2 = \frac{\frac{k}{m} \frac{1}{1+\sigma}}{(\omega_1^2 - \omega^2 + \frac{k}{m})(\omega_2^2 - \omega^2 + \frac{k}{m}) - (\frac{k}{m})^2} a_1. \quad (1.18)$$

The amplitudes of the two pendulums as a function of the frequency of an external force are shown in Fig.1.10(a) and (b), respectively, where we have used $\sigma = -0.1$, $k/m = 0.1$, and $a_1 = 0.1$. In the figure, the frequency ω is normalised by ω_1 . Two resonant peaks appear, the location of the resonant peaks corresponds to the real parts of the complex eigen-frequencies $\tilde{\omega}_{1,2} = \sqrt{\lambda_{1,2}}$ (Eq.(1.10)). In Fig.1.10(a), the reason why the second resonant peak is asymmetric is due to the existence of the zero-frequency at $\omega_{zero} = \sqrt{\omega_2^2 + \frac{k}{m}} = 1.0954$, which is right near the peak position(see the inset), and depends on the coupling strength k/m . The tendency of the resonance of the second pendulum as a function of the frequency is rather straightforward, see Fig. 1.10(b).

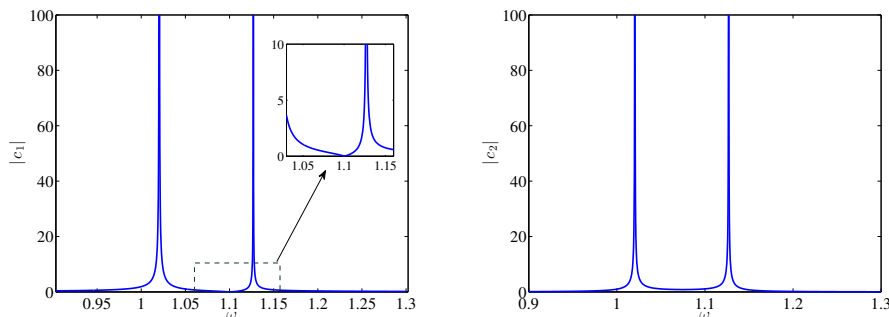


Figure 1.10: The amplitudes of the (a) pendulum 1 and (b) pendulum 2 as a function of frequency, where the frequency is in units of the natural frequency ω_1 . The other parameters are $\omega_1 = 1$, $\sigma = -0.1$, $a_1 = 0.1$, and $k/m = 0.1$.

Fano resonance in an acoustic waveguide with a single defect

Analogous to the single defect in a quasi-one-dimensional wire [53, 63, 64], we also consider a single defect with $Y(x) \in [0, x_1]$ in a acoustic duct with normalized height $h = 1$. The defect is introduced by a normalized admittance $Y(x)$ with very small length x_1 , see Fig. 1.11. When the length x_1 is very small and tends to be *zero*, the admittance can be expressed by a δ function, i.e., $Y(x) = Y_0\delta(x)$, with $\delta(x) = 1$ if and only if $x = 0$, else $\delta(x) = 0$.

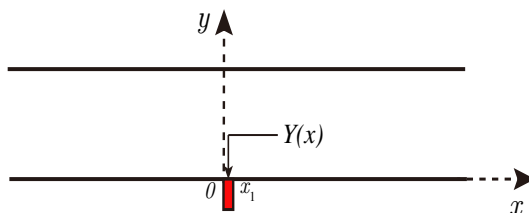


Figure 1.11: A single defect introduced by a normalized admittance $Y(x)$ in an acoustic waveguide. The length of the admittance is x_1 .

Here and in the following, all quantities are nondimensionalized. The sound $p(x, y)$ can propagate along x direction, the full wave equation is

$$\left(\frac{\partial^2}{\partial x^2} + \frac{\partial^2}{\partial y^2} + K^2 \right) p(x, y) = 0, \quad (1.19)$$

where $K = \omega h/c_0$ is the dimensionless frequency, ω is the circular frequency, and c_0 is

the ambient sound speed. The admittance boundary condition can be written as

$$\left. \frac{\partial p(x, y)}{\partial y} \right|_{y=0} = -jKY(x)p(x, 0), \quad (1.20)$$

with time dependence $e^{-j\omega t}$ used.

We will expand the solutions of the full scattering problem (Eq.(1.19)) in terms of the rigid transverse eigenfunctions $\phi_n(y)$ (see Eq. (1.3))

$$p(x, y) = \sum_{n=0}^{\infty} c_n(x)\phi_n(y). \quad (1.21)$$

Multiplying Eq.(1.19) by $\phi_m(y)$, integrating over y , and substituting Eq.(1.21) into the resulting equation, we can have

$$\frac{\partial^2 c_m(x)}{\partial x^2} + \left. \frac{\partial p}{\partial y} \phi_m(y) \right|_0^1 - p \left. \frac{\partial \phi_m}{\partial y} \right|_0^1 + \int_0^h p \frac{\partial^2 \phi_m(y)}{\partial y^2} dy + K^2 c_m(x) = 0. \quad (1.22)$$

Applying the boundary conditions Eq.(1.20) and the Eq.(1.3) into the above equation Eq.(1.22), we obtain

$$\frac{\partial^2 c_m(x)}{\partial x^2} + (K^2 - \alpha_m^2)c_m(x) = -jKY(x) \sum_n c_n(x)\phi_n(0)\phi_m(0). \quad (1.23)$$

The upper equation can be written in a matrix form

$$\frac{\partial^2 c_m(x)}{\partial x^2} + (K^2 - \alpha_m^2)c_m(x) = \sum_n M_{mn}^0 c_n(x), \quad (1.24)$$

where

$$M_{mn}^0 = -jKY(x)\phi_m(0)\phi_n(0).$$

In the regions where the admittance is zero, the solutions to Eq.(1.24) are

$$c_n(x) = \begin{cases} A_n e^{j\beta_n x} + B_n e^{-j\beta_n x}, & x < 0 \\ C_n e^{j\beta_n(x-x_1)} + D_n e^{-j\beta_n(x-x_1)}, & x > x_1 \end{cases} \quad (1.25)$$

for the propagating modes, where $\beta_n = \sqrt{K^2 - \alpha_n^2}$, and

$$c_n(x) = \begin{cases} A_n e^{-|\beta_n|x} + B_n e^{|\beta_n|x}, & x < 0 \\ C_n e^{-|\beta_n|(x-x_1)} + D_n e^{|\beta_n|(x-x_1)}, & x > x_1 \end{cases} \quad (1.26)$$

for the evanescent modes.

Let the δ -function admittance be

$$Y(x) = Y_0\delta(x). \quad (1.27)$$

Integrating Eq.(1.24) across the δ function gives

$$\left. \frac{\partial c_m(x)}{\partial x} \right|_{x=0^+} - \left. \frac{\partial c_m(x)}{\partial x} \right|_{x=0^-} = \sum_n M_{mn}^0 c_n(0), \quad (1.28)$$

we have used $c_m(0^+) = c_m(0^-)$.

We suppose that plane mode is incident, and $|KY_0| < |\alpha_0 - \alpha_1|$ and $K < \alpha_1$. In this case, only the plane mode is propagating, and it is sufficient to consider only one evanescent mode $n = 1$. We assume that the waves are incident from the left, resulting in $D_n = 0$ for all the modes, and $A_n = 0$ for all the evanescent modes. We can write

$$A_1 + B_1 = C_1, \quad B_2 = C_2,$$

$$j\beta_1 C_1 - j\beta_1(A_1 - B_1) = M_{11}^0 C_1 + M_{12}^0 C_2,$$

and

$$-|\beta_2|C_2 - |\beta_2|B_2 = M_{21}C_1 + M_{22}C_2.$$

We obtain

$$\begin{aligned} (2j\beta_1 - M_{11}^0)C_1 - M_{12}^0 C_2 &= 2j\beta_1 A_1, \text{ and} \\ M_{21}^0 C_1 + (M_{22}^0 + 2|\beta_2|)C_2 &= 0. \end{aligned} \quad (1.29)$$

From the above two equations, we can have the amplitudes for the transmitted modes

$$C_1 = \frac{2j\beta_1(M_{22}^0 + 2|\beta_2|)}{(2j\beta_1 - M_{11}^0)(M_{22}^0 + 2|\beta_2|) + (M_{12}^0)^2} A_1, \quad (1.30)$$

$$C_2 = \frac{-2j\beta_1 M_{21}^0}{(2j\beta_1 - M_{11}^0)(M_{22}^0 + 2|\beta_2|) + (M_{12}^0)^2} A_1. \quad (1.31)$$

From Eq.(1.30), the transmission and reflection coefficients for the plane mode are obtained as

$$t_{11} = \frac{C_1}{A_1} = \frac{2j\beta_1(M_{22}^0 + 2|\beta_2|)}{(2j\beta_1 - M_{11}^0)(M_{22}^0 + 2|\beta_2|) + (M_{12}^0)^2}, \quad (1.32)$$

$$r_{11} = \frac{B_1}{A_1} = \frac{M_{11}^0(M_{22}^0 + 2|\beta_2|) - (M_{12}^0)^2}{(2i\beta_1 - M_{11}^0)(M_{22}^0 + 2|\beta_2|) + (M_{12}^0)^2}. \quad (1.33)$$

We can see that if $M_{22}^0 + 2|\beta_2| = 0$, we have $t_{11} = 0$. Since

$$M_{22}^0 = -jKY_0\phi_2(0)\phi_2(0) = -2jKY_0,$$

we can have

$$-2jKY_0 + 2\sqrt{\alpha_2^2 - K^2} = 0,$$

this results in

$$K_{zero}^2 = \frac{\alpha_2^2}{1 - Y_0^2}. \quad (1.34)$$

If Y_0 is purely imaginary negative value, we can have $K_{zero} < \alpha_2$. Let us take a look at the reflection coefficient, if

$$M_{11}^0(M_{22}^0 + 2|\beta_2|) - (M_{12}^0)^2 = 0,$$

we will have reflection zero, namely, transmission is one, and because

$$M_{11}^0 M_{22}^0 - (M_{12}^0)^2 = 0,$$

so that if $|\beta_2| = 0$, namely, the incident frequency equals to cut-on frequency of the second mode, then the maximum transmission is reached. The transmission zero followed by a transmission one constructs the Fano resonance line-shape [53], see Fig.1.12(a). For the sake of simplification, we assume that the admittance $Y = -0.5i$ is independent of frequency. The wave functions $c_1(x)$ and $c_2(x)$ are plotted in Fig.1.12(b). We can see that wave $c_2(x)$ is localized at the defect position, and decreases to infinite.

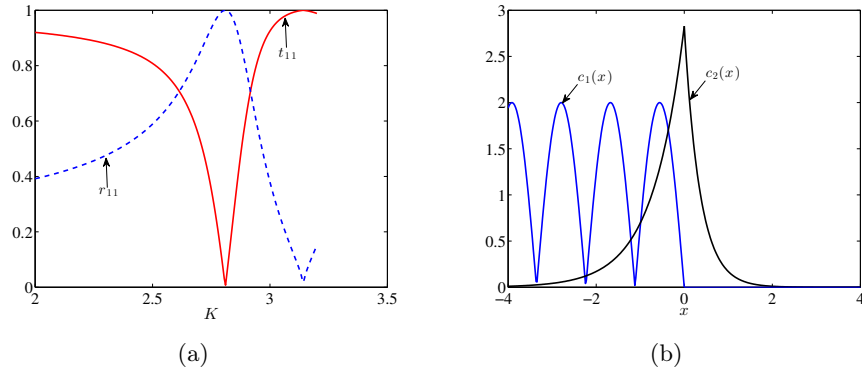


Figure 1.12: (a) Transmission and reflection coefficients of the first mode as a function of frequency. (b) The wave functions $c_1(x)$ and $c_2(x)$ when $|t_{11}| = 0$.

Comparing the two cases: an impedance in the acoustic waveguide and an attractive potential in the quantum waveguide [53], they both have the same form for the transmission and reflection coefficients when the impurity can be represented by a δ function.

1.6 R-matrix method

In this thesis, an efficient method, the Reaction matrix (R-matrix) method [65], is used to study the wave propagation in perturbed acoustic waveguide, the use of this method in this thesis can be found in chapters 2 and 3. The R-matrix method can treat easily the non-separable problem along transverse and axial directions. It was developed by Wigner and Eisenbud [65] in scattering processes in nuclear physics in the late 1940s. Recently, it was extended by Racec *et al* [66] to investigate the scattering phenomena in cylindrical nanowire heterostructures. The basic idea of this method is similar to the Multimodal method [50, 51]. For Multimodal method, the wave function is expanded in terms of a convenient transverse complete basis. The R-matrix method decomposes the whole system into a scattering region (cavity or acoustic liner in this thesis), and two semi-infinite rigid ducts. The wave function in the scattering region is expanded in terms of any convenient complete set of modes of a *closed cavity* with convenient boundary conditions. It is noted that the basis includes the transverse and axial components. Using the continuity conditions of the pressure and the normal particle velocity at the interfaces between the regions, we can write the scattering matrix \mathbf{S} in terms of the R-matrix. Similar studies using R-matrix to calculate \mathbf{S} matrix can be found in Refs. 67, 68, 69.

By the scattering matrix, the matrix \mathbf{H}_{eff} of the open system is derived [70]. Matrix \mathbf{H}_{eff} describes totally the properties of the open cavity/lined section. Its eigenvalues are complex and give the poles of the \mathbf{S} matrix. Its eigenfunctions are used for the calculation of the coupling matrix between the *open* cavity/lined section and uniform waveguide. There are some important advantages of this method. \mathbf{H}_{eff} is frequency dependent, therefore its eigenvalues or the complex poles of the \mathbf{S} matrix and its eigenfunctions or the coupling matrix are frequency dependent. The frequency dependence of poles may be not important in the case of isolated resonances, but it is very important when the resonances are overlapping [59, 70]. Another advantage of this method is that the \mathbf{S} matrix is related clearly to the coupling matrix between the *open* cavity/lined section and uniform waveguide as shown in Eq. (3.20) in Chap. 3. The calculation method is inspired by Stöckmann *et al.* [70], who developed a relation of \mathbf{S} matrix with an effective Hamiltonian for a microwave billiard with attached waveguide.

1.7 Thesis organization

The central theme of this thesis is to use the mode coupling effects to reduce the sound transmission in an acoustic duct for potential applications, for example silencers for ventilation systems, wall treatments for aircraft engines, and silencers for industrial gas turbines. This dissertation is organized into six chapters. Besides the current chapter (which intends to give a brief introduction of some basic and important concepts) and the last chapter with the conclusions, the other four chapters are organized as follows:

In chapter 2, the first strategy is first introduced and presented by using a simple duct-cavity system. The trajectories of the modes in a closed cavity with varying the cavity length are first reviewed. After the closed cavity is opened and attached to rigid duct, the R-matrix method is introduced to solve the wave propagation problem in the system. Trapped modes can be found at some particular parameter combinations and near the avoided crossing of eigenvalues between two neighbored modes.

In chapter 3, the same strategy introduced and presented in chapter 2 is applied here to an acoustic waveguide lined with locally reacting liner, in order to produce an additional transmission zero, besides the one due to the resonance frequency of the liner. The scattering matrix is also derived by using the R-matrix method. For that, we project the Helmholtz equation over the eigenfunctions of the rigid closed counterpart of the scattering region which form an orthogonal and complete function basis. We express the scattering matrix S in terms of an effective matrix H_{eff} . By using matrix H_{eff} , the traditional acoustic resonance scattering formula is extended to describe the coupling effects between the open lined section and the rigid parts of the waveguide.

In chapter 4, the second strategy is presented to deal with the porous material. A set of periodic rigid inclusions are embedded in a porous lining to enhance sound attenuation in an acoustic duct at low frequencies. Floquet-Bloch theorem is introduced to investigate the mode attenuation in an infinite waveguide lined with periodic inclusions embedded in porous material. An analysis is first given for a 2D infinite periodic waveguide, crossing is observed for the mode attenuations between two Bloch waves, resulting in the maximum attenuation. Experimental measurements and numerical simulations are performed to obtain the transmission loss for 3D configurations. The transmission loss can be enhanced by the embedment of the rigid inclusions.

In chapter 5, we investigate the the acoustical behaviours of a purely reacting liner in a rectangular duct in both absence and presence of flow. Multi-Model Method is proposed to solve the problem in the absence and presence of uniform flow. The classical Ingard-Myers boundary condition is used in the presence of flow. The results exhibit an unusual acoustical behaviour: for a certain range of frequencies, no wave can propagate against the flow. The effect of shear flow is investigated by the Chebyshev Spectral Method, which provides detailed information near the walls. The effects of the Mach number and the frequency on the eigenvalues of the modes are also studied.

Bibliography

- [1] R. A. Mangiarotty. Acoustic lining concepts and materials for engine ducts. *The Journal of the Acoustical Society of America*, 48(3C):783–794, 1970.
- [2] L. Cremer. Theory of sound attenuation in a rectangular duct with an absorbing wall and the resultant maximum attenuation coefficient. *Acustica*, 2:249–263, January 1953.
- [3] B. J. Tester. The optimization of modal sound attenuation in duct, in the absence of mean flow. *J. Sound Vib.*, 27:477–513, January 1973.
- [4] F. P. Mechel. Modal solutions in rectangular ducts lined with locally reacting absorbers. *Acustica*, 73:223–239, January 1991.
- [5] ALI H. NAYFEH, KAISER JOHN E., and TELIONIS DEMETRI P. Acoustics of aircraft engine-duct systems. *AIAA Journal*, 13(2):130–153, 1975.
- [6] H. H. Hubbard. *Aeroacoustics of Flight Vehicles: Theory and Practice, V. 1 and 2*. NASA Reference Publication, 1991.
- [7] WenPing Bi, Vincent Pagneux, Denis Lafarge, and Yves Aurégan. An improved multimodal method for sound propagation in nonuniform lined ducts. *The Journal of the Acoustical Society of America*, 122(1):280, 2007.
- [8] L. Flax, G. Gaunaurd, and H. Uberall. *Theory of Resonance scattering, in Physical Acoustics: Principles and Methods, Vol. XV, Eds., W. P. Mason and R. N. Thurston, Chap. 3, pp. 191–294*. Academic Press, January 1999.
- [9] Zhengyou Liu, Xixiang Zhang, Yiwei Mao, Y.Y. Zhu, Zhiyu Yang, C.T. Chan, and Ping Sheng. Locally resonant sonic materials. *Science*, 289(5485):1734–1736, September 2000.
- [10] Zhengyou Liu, C. Chan, and Ping Sheng. Analytic model of phononic crystals with local resonances. *Physical Review B*, 71(1), January 2005.
- [11] Nicholas Fang, Dongjuan Xi, Jianyi Xu, Muralidhar Ambati, Werayut Srituravanich, Cheng Sun, and Xiang Zhang. Ultrasonic metamaterials with negative modulus. *Nature Mater.*, 5(6):452–456, June 2006.

-
- [12] J.P. Groby, O. Dazel, A. Duclos, L. Boeckx, and L. Kelders. Enhancing the absorption coefficient of a backed rigid frame porous layer by embedding circular periodic inclusions. *J. Acoust. Soc. Am.*, 130(6):3771, 2011.
- [13] Benoit Nennig, Ygaäl Renou, Jean-Philippe Groby, and Yves Aurégan. A mode matching approach for modeling two dimensional porous grating with infinitely rigid or soft inclusions. *J. Acoust. Soc. Am.*, 131(5):3841–3852, 2012.
- [14] Benoit Nennig, Ygääl Renou, and Yves Aurégan. On the use of periodic inclusions embedded in porous lining to enhanced attenuation in waveguides. *Société Francaise d’Acoustique*, April 2012.
- [15] C. E. Bradley. Time harmonic acoustic bloch wave propagation in periodic waveguides. part i. theory. *The Journal of the Acoustical Society of America*, 96(3):1844–1853, 1994.
- [16] P. Exner, P. Seba, M. Tater, and D. Vanek. Bound states and scattering in quantum waveguides coupled laterally through a boundary window. *J. Math. Phys.*, 37:4867–4887, 1996.
- [17] Yuting Duan, Werner Koch, Chris M. Linton, and Maureen McIVER. Complex resonances and trapped modes in ducted domains. *Journal of Fluid Mechanics*, 571:119, January 2007.
- [18] V. Pagneux. Trapped modes and edge resonances in acoustics and elasticity. *CISM International Centre for Mechanical Sciences*, 547:181–223, January 2013.
- [19] von Neumann and E. P. Wigner. Uber merkwurdige diskrete eigenwerte. *Phys. Z.*, 30:465–467, 1929.
- [20] R. Parker. Resonance effects in wake shedding from parallel plates: Some experimental observations. *Journal of Sound and Vibration*, 4(1):62–72, July 1966.
- [21] R. Parker. Resonance effects in wake shedding from parallel plates: Calculation of resonant frequencies. *Journal of Sound and Vibration*, 5:330–343, 1967.
- [22] Stefan Hein, Werner Koch, and Lothar Nannen. Trapped modes and fano resonances in two-dimensional acoustical duct-cavity systems. *Journal of Fluid Mechanics*, 692:257–287, February 2012.
- [23] W D Heiss and A L Sannino. Avoided level crossing and exceptional points. *Journal of Physics A: Mathematical and General*, 23(7):1167–1178, April 1990.
- [24] W. Heiss. Repulsion of resonance states and exceptional points. *Physical Review E*, 61(1):929–932, January 2000.

-
- [25] H. Friedrich and D. Wintgen. Interfering resonances and bound states in the continuum. *Physical Review A*, 32(6):3231–3242, December 1985.
- [26] Almas Sadreev, Evgeny Bulgakov, and Ingrid Rotter. Bound states in the continuum in open quantum billiards with a variable shape. *Physical Review B*, 73(23), June 2006.
- [27] P. M. Morse and K. U. Ingard. *Theoretical acoustics*. McGraw-Hill Book Company, New York, January 1968.
- [28] T. Kato. *Perturbation Theory of Linear Operators*. Berlin: Springer, 1966.
- [29] W D Heiss. Exceptional points of non-hermitian operators. *Journal of Physics A: Mathematical and General*, 37:2455–2464, 2004.
- [30] Ingrid Rotter. A non-hermitian hamilton operator and the physics of open quantum systems. *Journal of Physics A: Mathematical and Theoretical*, 42(15):153001, April 2009.
- [31] U. Gunther, I. Rotter, and B. Samsonov. Projective hilbert space structures at exceptional points. *Journal of Physics A: Mathematical and Theoretical*, 40:8815–8833, 2007.
- [32] M. Muller and I. Rotter. Exceptional points in open quantum systems. *Journal of Physics A: Mathematical and Theoretical*, 41:244018, 2008.
- [33] M. V. Berry. Physics of nonhermitian degeneracies. *Czechoslovak J. of Phys.*, 54:1039–1047, 2004.
- [34] Wenping Bi and Vincent Pagneux. New insights into mode behaviours in waveguides with impedance boundary conditions. *ArXiv e-prints*, arXiv:1511.05508 [quant-ph], November 2015.
- [35] C. Dembowski, H.-D. Gräf, H. L. Harney, A. Heine, W. D. Heiss, H. Rehfeld, and A. Richter. Experimental observation of the topological structure of exceptional points. *Physical Review Letter*, 86:787, January 2001.
- [36] W. D. Heiss. The physics of exceptional points. *J. Phys. A: Math. There.*, 45:444016, 2012.
- [37] O. Latinne, N. J. Kylstra, M. Dörr, J. Purvis, M. Terao-Dunseath, C. J. Joachain, P. G. Burke, and C. J. Noble. Laser-induced degeneracies involving autoionizing states in complex atoms. *Physical Review Letter*, 74:46, 1995.
- [38] M. K. Oberthaler, R. Abfaltrerer, S. Bernet, J. Schmiedmayer, and A. Zeilinger. Atom waves in crystals of light. *Physical Review Letter*, 77:4980, January 1996.

-
- [39] T. Stehmann, W. D. Heiss, and F. G. Scholtz. Observation of exceptional points in electronic circuits. *J. Phys. A*, 37:7813, January 2004.
- [40] H. Cartarius, J. Main, and G. Wunner. Exceptional points in atomic spectra. *Phys. Rev. Lett.*, 99:173003, January 2007.
- [41] C. Dembowski, B. Dietz, H.-D. Gräf, H. L. Harney, A. Heine, W. D. Heiss, and A. Richter. Observation of a chiral state in a microwave cavity. *Physical Review Letter*, 90:034101, January 2003.
- [42] C. Dembowski, B. Dietz, T. Friedrich, H.-D. Gräf, A. Heine, C. Mejía-Monasterio, M. Miski-Oglu, A. Richter, and T. H. Seligman. First experimental evidence for quantum echoes in scattering systems. *Physical Review Letter*, 93:134102, January 2004.
- [43] von Neumann and E. P. Wigner. Uber das verhalten von eigenwerten bei adiabatischen prozessen. *Phys. Z*, 30:467–470, 1929.
- [44] L. D. Landau and I. M. Lifshitz. *Quantum Mechanics*. Oxford: Pergamon, January 1991.
- [45] A. W. Leissa. On a curve veering aberration. *J. Applied Math. and Phys. (ZAMP)*, 25:99–111, 1974.
- [46] J. R. Kuttler and V. G. Sigillito. On curve veering. *J. Sound and Vib.*, 75:585–588, 1981.
- [47] N. C. Perkins and C. D. Mote. Comments on curve veering in eigenvalue problem. *J. Sound and Vib.*, 106:451–463, January 1986.
- [48] C. Pierre. Mode localisation and eigenvalue loci veering phenomena in disordered structures. *J. Sound and Vib.*, 126:485–502, January 1988.
- [49] M. S. Triantafyllou and G. S. Triantafyllou. Frequency coalescence and mode localisation phenomena: a geometric theory. *J. Sound and Vib.*, 150:485–500, January 1991.
- [50] V. Pagneux, N. Amir, and J. Kergomard. A study of wave propagation in varying cross-section waveguides by modal decomposition. part i. theory and validation. *The Journal of the Acoustical Society of America*, 100(4):2034, 1996.
- [51] W.P. Bi, V. Pagneux, D. Lafarge, and Y. Aurégan. Modelling of sound propagation in a non-uniform lined duct using a multi-modal propagation method. *Journal of Sound and Vibration*, 289(4-5):1091–1111, February 2006.
- [52] U. Fano. Effects of configuration interaction on intensities and phase shifts. *Physical Review*, 124(6):1866–1878, December 1961.

-
- [53] Yong S Joe, Arkady M Satanin, and Chang Sub Kim. Classical analogy of fano resonances. *Physica Scripta*, 74(2):259, 2006.
- [54] Boris Luk'yanchuk, Nikolay I. Zheludev, Stefan A. Maier, Naomi J. Halas, Peter Nordlander, Harald Giessen, and Chong Tow Chong. The fano resonance in plasmonic nanostructures and metamaterials. *Nature Materials*, 9(9):707–715, September 2010.
- [55] Andrey E. Miroshnichenko, Sergej Flach, and Yuri S. Kivshar. Fano resonances in nanoscale structures. *Reviews of Modern Physics*, 82(3):2257–2298, August 2010.
- [56] Jens U. Nockel and A. Douglas Stone. Resonance line shapes in quasi-one-dimensional scattering. *Physical Review B*, 50, June 1994.
- [57] E. Tekman and P. F. Bagwell. Fano resonances in quasi-one-dimensional electron waveguides. *Physical Review B*, 48, June 1993.
- [58] Vassilios Vargiamidis and Hariton M. Polatoglou. Resonances in electronic transport through a quantum wire with impurities and variable cross-sectional shape. *Physical Review B*, 72, June 2005.
- [59] I. Rotter A. I. Magunov and S. I. Strakhova. Fano resonances in the overlapping regime. *Physical Review B*, 68, June 2003.
- [60] Arkady M. Satanin and Yong S. Joe. Fano interference and resonances in open systems. *Physical Review B*, 71, June 2005.
- [61] S. A. Gurvitz and Y. B. Levinson. Resonant reaction and transmission in a conducting channel with a single impurity. *Physical Review B*, 47, June 1993.
- [62] S. Hein, W. Koch, and L. Nannen. Fano resonances in acoustics. *J. Fluid Mech.*, 664:238–264, January 2010.
- [63] Philip F. Bagwell. Evanescent modes and scattering in quasi-one-dimensional wires. *Phy. Rev. B*, 41(15):10354, 1990.
- [64] Erkan Tekman and Philip F. Bagwell. Fano resonances in quasi-one-dimensional electron waveguides. *Phys. Rev. B*, 48:2553–2559, Jul 1993.
- [65] E. Wigner and L. Eisenbud. Higher angular momenta and long range interaction in resonance reactions. *Phys. Rev.*, 72(1):29–41, July 1947.
- [66] P. Racec, E. Racec, and H. Neidhardt. Evanescent channels and scattering in cylindrical nanowire heterostructures. *Physical Review B*, 79(15), April 2009.
- [67] E. R. Racec, U. Wulf, and P. N. Racec. Fano regime of transport through open quantum dots. *Physical Review B*, 82(8), August 2010.

-
- [68] G. B. Akguc and L. E. Reichl. Effect of evanescent modes and chaos on deterministic scattering in electron waveguides. *Phys. Rev. E*, 64:056221, January 2001.
 - [69] G. B. Akguc and L. E. Reichl. Direct scattering processes and signatures of chaos in quantum waveguides. *Phys. Rev. E*, 67:046202, January 2003.
 - [70] H.-J. Stöckmann, E. Persson, Y.-H. Kim, M. Barth, U. Kuhl, and I. Rotter. Effective hamiltonian for a microwave billiard with attached waveguide. *Physical Review E*, 65(6), June 2002.

Chapter 2

Fano resonance scattering in a duct-cavity system

In this chapter, the trapped mode due to the interaction of two neighbored modes in an open system is first investigated in a simple duct-cavity system. The eigenvalues of the modes depend on the geometry of the cavity. By varying one parameter continuously, two types of avoided crossings between the eigenvalues of two modes in the complex plane are observed under two different values of the other parameter. The transition between these two different avoided crossings indicates the existence of the exceptional point in the parameter plane. In the vicinity of the avoided crossing, a trapped mode with almost vanishing imaginary part is always found. This trapped mode couples with the incoming propagating mode, resulting in the Fano resonance which give raises to an asymmetric transmission line-shape. A transmission zero is observed in the vicinity of this asymmetric line-shape.

2.1 Introduction

A duct-cavity system is often used to study the scattering of sound due to the expansion chamber in an acoustic waveguide, especially with the presence of flow [1]. Typical applications are internal combustion engine exhaust silencers and silencers in industrial duct systems. Similar resonant-cavity configurations have also been used in other various wave propagation systems and led to important applications, see for example Refs. [2, 3, 4, 5, 6] .

The purpose of this chapter is to investigate the mechanism associated with trapped modes that cause transmission dips in acoustic waveguide when avoided crossings are formed between two modes, by using the simple duct-cavity system. S. Hein *et al.* [7]

used FEM to numerically compute the complex modes of the similar system. However, to our knowledge, there is no theory to describe the coupling of the modes of the closed system via the transverse modes of the attached ducts in acoustics. Motivated by this situation, in our work, a matrix \mathbf{H}_{eff} [8, 9] is derived to explicitly describe the coupling effects.

The existence of trapped mode problem in waveguides has been investigated by many authors in various physical contexts theoretically and experimentally. Trapped modes were introduced more than fifty years ago (see for example, Ursell [10] and Jones [11]), and since then have induced an important amount of works in acoustics, electromagnetism, elasticity, quantum mechanics and water waves, for review articles see, for example, Refs. 12, 13, and the references therein. In this work, we will focus on the discrete trapped modes existing above the first cut-off frequency for specific parameter combinations, which are called embedded trapped modes [13] or bound states in continuum (BICs) in quantum mechanics [14, 15]. By Feshbach's theory of resonance, Friedrich and Wintgen [16] demonstrated that BICs in atomic physics can occur, due to the interference of resonances (or modes in acoustic vocabulary) belonging to different channels. By varying the separation of the two resonances as a function of a continuous parameter, avoided crossings of resonances are observed. At a particular value of the parameter, one resonance has exactly vanished width (the imaginary part of the eigenvalue is zero), and becomes a BIC. In quantum systems, Almas F. Sadreev *et al.* [2] showed that the BIC also appears in open quantum billiards by varying their shape continuously. They also found that the BICs are close to the points of *degeneracy* [17] of the closed quantum system. When the system is opened, the coupling of the two resonances is turned on, an *avoided crossing* occurs with the variation of the parameters [18, 19]. The avoided crossing is associated with the *Exceptional Points*(EPs) [18, 19] in the complex plane. At the EPs, the two resonances will coalesce, not only the eigenvalues but also the eigenfunctions.

Trapped (quasi-trapped) modes or bound (quasi-bound) states are crucial ingredient of Fano resonance scatterings in waveguides with impurities [20] or quantum dots with an attractive potential [21, 22]. Fano resonance was firstly suggested by Ugo Fano [23] for the description of autoionizing atomic states. In contrast to the conventional isolated resonances, e.g., resonance in a harmonic oscillator with periodic forcing, whose spectral dependence can be described by the Lorentzian or Breit-Wigner formula – a symmetric spectral line; Fano resonance was explained as a phenomenon of constructive and destructive interferences between a bound state and the continuum [23]. The corresponding spectral lines are asymmetric. Since its discovery, Fano resonance has been attracting much attention in different research fields, for review articles see, for example, [24, 25] and the references therein.

Fano resonances scatterings in acoustics and their relations with trapped modes in waveguides including obstacles or in duct-cavity systems have been shown by Hein, Koch and Nannen [7, 26]. They use finite-element method to numerically compute the acoustic

modes as well as transmission and reflection for an incoming fundamental duct mode. For the resonance problem, they obtained complex resonance frequencies and corresponding eigenfunctions, i.e., the homogeneous solutions of the Helmholtz equation with a perfectly matched layer as absorbing boundary conditions. The complex resonance frequencies are the positions of the poles of scattering matrix of the corresponding scattering problem.

The Reaction matrix (R-matrix) method [27] is used to study the wave propagation in the duct-cavity system. The R-matrix formulation was developed by Wigner and Eisenbud [27] in scattering processes in nuclear physics in the late 1940s. Recently, it was extended by Racec *et al.* [28] to investigate the scattering phenomena in cylindrical nanowire heterostructures. The basic idea of this method is similar to the Multimodal method [29, 30]. For Multimodal method, the wave function is expanded in terms of a convenient transverse complete basis. The R-matrix method decomposes the whole system into a scattering region, and an asymptotic scattering region (here, two semi-infinite rigid ducts). The wave function in the scattering region is expanded in terms of any convenient complete set of modes of a *closed cavity* with convenient boundary conditions. It is noted that the basis includes the transverse and axial components. Using the continuity conditions of the pressure and the normal particle velocity at the interfaces between the regions, we can have the scattering matrix. Once the scattering matrix is obtained, the transmission and reflection coefficients can be obtained easily. By the scattering matrix, the matrix \mathbf{H}_{eff} of the open system is derived. Its eigenvalues are complex and give the poles of the \mathbf{S} matrix.

This chapter is organized as follows. In Chap.2.2, the formulation of the R-matrix method is described, the scattering matrix \mathbf{S} in terms of and matrix \mathbf{H}_{eff} are also derived. The relation between the eigenvalues of the matrix \mathbf{H}_{eff} and the poles of the matrix \mathbf{S} is also discussed. The conception of *exceptional point* is introduced by studying the motions of the eigenvalues of \mathbf{H}_{eff} with varying the cavity length. In Chap.2.3, we present that trapped modes are observed due to the coupling of two neighbored modes. The interaction of the trapped mode with the incoming propagating mode, results in the Fano resonance. We give the conclusion in the last section.

2.2 Formulation and method of the problem

We consider the acoustic scattering problem in a two-dimensional infinite duct-cavity system, see Fig. 2.1. The sound pressure $p(x, y)$ in the waveguide satisfies the non-dimensional governing equation

$$\left(\frac{\partial^2}{\partial x^2} + \frac{\partial^2}{\partial y^2} + K^2 \right) p(x, y) = 0, \quad (2.1)$$

with $K = (\omega^*/c_0^*)h^*$ the dimensionless incident frequency, where ω^* is the circular frequency, time dependence $\exp(-j\omega^*t^*)$ is applied. Here the asterisk denotes dimensional

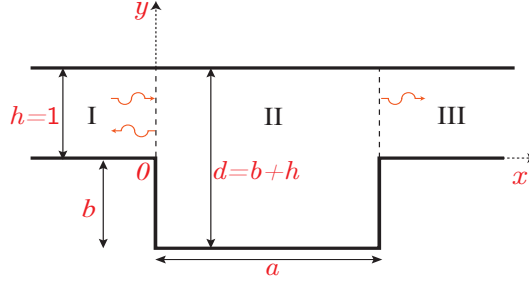


Figure 2.1: A 2D acoustical duct-cavity system, the lengths are normalized by the duct height h^* , i.e. $a = a^*/h^*$ and $b = b^*/h^*$.

quantities. All quantities are made dimensionless in the following: lengths with the uniform duct height h^* ($h = 1$ in the following), velocities with sound speed c_0^* , densities with the ambient density ρ_0^* , and pressures with $\rho_0^* c_0^{*2}$.

To solve the sound scattering problem, the whole waveguide is split into three regions: the two semi-infinite uniform ducts $x < 0$ and $x > a$ (Region I and III, respectively), and the corresponding scattering region $0 < x < a$ (Region II). The sound pressure in the whole waveguide system is then piecewise solved. Out of the scattering region, the sound pressure can be expressed as a sum over the transverse modes of uniform ducts with rigid boundary conditions. In the numerical example, only the plane mode will be incident, but the analysis presented here is more general by assuming that one single duct mode m is incident from the left side of the waveguide. For $x < 0$, the sound pressure is written as a sum of the incident and reflected modes, and only transmitted modes for $x > a$:

$$p_m(x, y) = \begin{cases} e^{jK_m x} \phi_m(y) + \sum_{m'=0}^{M-1} R_{m',m} e^{-jK_{m'} x} \phi_{m'}(y), & x \leq 0, \\ \sum_{m'=0}^{M-1} T_{m',m} e^{jK_{m'}(x-a)} \phi_{m'}(y), & x \geq a, \end{cases} \quad (2.2)$$

where

$$K_m^2 = K^2 - \alpha_m^2, \quad (2.3)$$

with $\Re\{K_m\} > 0$, $\Im\{K_m\} > 0$, $m(m') = 0, 1, 2, \dots, M-1$. M is the truncation number of the transverse modes in the uniform ducts, (α_m, ϕ_m) are the eigenvalues and the eigenfunctions of the transverse modes in the uniform duct with rigid boundary conditions, with $\alpha_m = m\pi$, and $\phi_m(y)$ satisfying the orthogonality relation

$$\int_0^1 \phi_m(y) \phi_n(y) dy = \delta_{mn}. \quad (2.4)$$

In the expression of the acoustic pressure, Eq. (2.2), \mathbf{R} and \mathbf{T} are matrices linking incoming and outgoing wave components. They are also used to define the scattering matrix \mathbf{S} , as given in Eq. (2.5),

$$\mathbf{S} = \begin{pmatrix} \mathbf{R} & \mathbf{T}' \\ \mathbf{T} & \mathbf{R}' \end{pmatrix}. \quad (2.5)$$

Matrices \mathbf{R} and \mathbf{T} (respectively, \mathbf{R}' and \mathbf{T}') correspond to wave incident from the left (respectively, from the right). In this work, due to the symmetry of the geometry $\mathbf{R} = \mathbf{R}'$, and due to the reciprocity $\mathbf{T} = \mathbf{T}'$.

2.2.1 R-matrix method

According to the R-matrix method [28], the sound pressure $p(x, y)$ in the scattering region (Region II) is projected on the complete basis of functions $\psi_{\mu\nu}(x, y)$

$$p_m(x, y) = \sum_{\mu=0}^{N_x-1} \sum_{\nu=0}^{N_y-1} a_{m,\mu\nu} \psi_{\mu\nu}(x, y), \quad 0 < x < a, \quad (2.6)$$

where the sums have been truncated by N_x and N_y . We choose the $\psi_{\mu,\nu}$ to be the eigenfunctions of *closed cavity* with length a and width d ($d = h + b$) defined by

$$\nabla^2 \psi_{\mu\nu} = -\gamma_{\mu\nu}^2 \psi_{\mu\nu}, \quad (2.7)$$

$$\left. \frac{\partial \psi_{\mu\nu}}{\partial x} \right|_{x=0,a} = 0, \quad \left. \frac{\partial \psi_{\mu\nu}}{\partial y} \right|_{y=-b,h} = 0. \quad (2.8)$$

The eigenvalues $\gamma_{\mu\nu}$ and eigenfunctions $\psi_{\mu\nu}(x, y)$ are classified by two integers (μ, ν) , where μ ($0, 1, 2, \dots, N_x - 1$) labels the longitudinal mode, and ν ($0, 1, 2, \dots, N_y - 1$) the transverse mode.

It is shown in Appendix 2.A.1 that a relation between the coefficients, $a_{m,\mu\nu}$, and the first derivative of the pressure with respect to x ($\partial p_m / \partial x$) at the interfaces can be written in the form of

$$\vec{a}_m \mathbf{K}_N = \int_0^h \frac{\partial p_m}{\partial x} \vec{\psi} \Big|_{x=a}^{x=0} dy, \quad (2.9)$$

where $\vec{a}_m = (a_{m,1}, a_{m,2}, a_{m,3}, \dots, a_{m,n}, \dots)$, $\vec{\psi} = (\psi_1, \psi_2, \psi_3, \dots, \psi_n, \dots)$, and \mathbf{K}_N is a $N \times N$ diagonal matrix with elements $K_n = K^2 - \gamma_n^2$. Here and in the following, $n = 1, 2, 3, \dots$ correspond to $(\mu, \nu) = (0, 0), (0, 1), (0, 2), \dots, (1, 0), (1, 1), (1, 2), \dots$, and $N = N_x \cdot N_y$ is the number of the eigenfunctions $\psi_{\mu\nu}$ taken into consideration.

To construct the scattering matrix \mathbf{S} , the continuity conditions of the pressure and the normal velocity at the discontinuity interfaces ($x = 0$ and a) are used. By Eqs. (2.9)

and (2.2), the scattering matrix S is given (see Appendix 2.A.2)

$$S^T = \left\{ I - 2 [I + jK_M Q]^{-1} \right\}, \quad (2.10)$$

where

$$Q = Q_1 K_N^{-1} Q_1^T, \quad (2.11)$$

Q_1 is the coupling matrix between the modes of the closed cavity and the transverse modes of the duct induced at the interfaces. Elements of Q_1 are shown in Appendix 2.A.2 Eq. (2.23). “ T ” indicates the transposition. K_M is a $2M \times 2M$ diagonal matrix with elements K_m , in which the upper M rows correspond to the situation when the mode is incident from the left side, the lower ones correspond to the opposite situation. Matrix K_M characterizes the uniform ducts.

2.2.2 Matrix H_{eff}

After attaching to the uniform ducts (Regions I and II), the modes of the closed cavity turn over in complex resonant modes. A matrix H_{eff} [8] is derived here to indirectly compute the eigenvalues K_R of the open system. From Eq. (2.27) in Appendix 2.A.3, the scattering matrix S is rewritten as

$$S = -I + 2jQ_1 \frac{1}{K^2 I - H_{\text{eff}}} Q_1^T K_M, \quad (2.12)$$

where

$$H_{\text{eff}} = H_{\text{cc}} - jQ_1^T K_M Q_1 \quad (2.13)$$

describes the closed cavity which is partially opened at $x = 0$ and a by attaching to the uniform ducts. Using the continuity conditions at interfaces $x = 0$ and a . H_{cc} denotes the closed cavity, it is a diagonal matrix with elements γ_n^2 . The second term of H_{eff} is due to the mode coupling introduced at the interfaces, and K_M is K dependent.

From Eq. (2.13), the matrix H_{eff} is complex, so do its eigenvalues (denoted by K_λ^2) and eigenvectors Ψ , which can be obtained by solving the eigenvalue problem

$$H_{\text{eff}} \Psi = K_\lambda^2 \Psi. \quad (2.14)$$

Due to the dependence of K_M on K in Eq. (2.13), matrix H_{eff} is also frequency dependent through the parameter, it also depends on the geometry size of the configuration. The coupling of the modes can be analyzed by using matrix H_{eff} .

For the duct-cavity system, the motions of the 3rd and the 4th K_λ as a function of cavity length a with $b = 1$ are investigated, as shown in Fig. 2.2. Two parameters, K and a , are used to control the movements of the two K_λ . Under different values of K , two different types of avoided crossings are observed (Figs. 2.2(c) and (f)), where

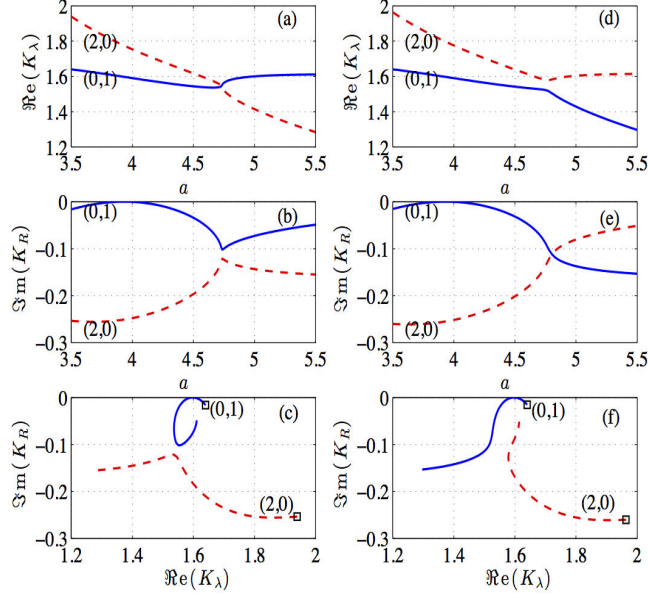


Figure 2.2: Real (a)(d) and imaginary (b)(e) parts of the 3rd (solid line) and the 4th (dashed line) eigenvalues K_λ as a function of length a for different values of K : (a)(b)(c) $K = 1.5$ and (d)(e)(f) $K = 1.6$, with $b = 1$, $M = 20$, $N = 30 \times 30$. The trajectories of the eigenvalues in the complex plane are shown in (c)(f). The “ \square ” in (c)(f) indicates the starting point.

quadrants change from (II, IV) to (I, III) (referring to Fig. 1.5 in Chap. 1). If we vary the two parameters a and K more precisely, at some critical values, a_{cri} and K_{cri} , the two eigenvalues and eigenvectors of \mathbf{H}_{eff} will *coalesce*. These critical values are called *exceptional point(s)* (EP(s)) [18, 19] in the parameter plane. In our example, $a_{cri} = 4.74$ and $K_{cri} = 1.51$ are found. If $K < K_{cri}$, crossing for the real (Fig. 2.2(a)) and avoided crossing for the imaginary (Fig. 2.2(b)) parts are observed; Inversely, avoided crossing (Fig. 2.2(d)) for the real and crossing (Fig. 2.2(e)) for the imaginary parts if $K > K_{cri}$. We can conclude that there always exists avoided crossing in the vicinity of the EP (see Figs. 2.2(c) and (f)). Re-examine the expression of \mathbf{H}_{eff} , Eq. (2.13), it is three parameters dependent, i.e. K , a , and b . If only two of them are used to control \mathbf{H}_{eff} , by fixing the third one, the EPs are isolated points in the plane of the two parameters, such as the example shown in Fig. 2.2. However, in the three-parameter space, the EPs will form a curve.

Based on the \mathbf{Q} matrix representation of the \mathbf{S} matrix, Eq. (2.10), the poles of the \mathbf{S} matrix are found as the solutions of the equation

$$\det[\mathbf{1} + j\mathbf{K}_M\mathbf{Q}] = 0. \quad (2.15)$$

If the above equation is satisfied, the singularities of the scattering matrix \mathbf{S} appear, which are also associated with the eigenvalues K_R of the open system. Instead of solving the eigenvalue problem of the open system directly, we return to locate the positions of the poles of matrix \mathbf{S} in the complex plane.

However, the representation of the \mathbf{S} matrix in terms of the matrix \mathbf{H}_{eff} , Eq. (2.12), has the advantage that it yields the positions of the poles, as well as K_R , by solving the eigenvalue problem of matrix \mathbf{H}_{eff} , with satisfying the fixed-point equation [8]

$$K_R = K_\lambda(K = \text{Re}(K_R)), \quad (2.16)$$

which can be solved numerically by using an iterative procedure. Due to the relation between K_R and K_λ , the EPs of modes K_R in the two-parameter plane is one isolate point from the EPs curve of K_λ in the three-parameter space.

In the following, the matrix \mathbf{H}_{eff} will be used to study the interference between the modes and to predict the parameter combinations of the trapped mode by making K approach to the trapped mode frequency.

2.3 Results and discussions

2.3.1 Degeneracy and avoided crossing

First, we would like to briefly review the eigenvalue problem of the corresponding closed cavity with vanishing normal velocity conditions toward the interfaces. The eigenvalues of the *closed cavity* with rigid boundary conditions can be obtained analytically,

$$\gamma_{\mu\nu} = \sqrt{\left(\frac{\mu\pi}{a}\right)^2 + \left(\frac{\nu\pi}{d}\right)^2}. \quad (2.17)$$

For a closed and conservative cavity, the eigenvalues $\gamma_{\mu\nu}$ show degeneracy [17] when the length a is varied, i.e. two modes have the same eigenvalues, meanwhile the eigenfunctions are still orthogonal. We assume that modes (p, q) and (m, n) have the same eigenvalues, which means that

$$\left(\frac{p\pi}{a}\right)^2 + \left(\frac{q\pi}{d}\right)^2 = \left(\frac{m\pi}{a}\right)^2 + \left(\frac{n\pi}{d}\right)^2.$$

We can have the condition on a/d ,

$$\frac{a}{d} = \sqrt{\frac{p^2 - m^2}{n^2 - q^2}}, \quad (2.18)$$

at which the two modes degenerate. We take mode $(m, n) = (0, 1)$ as an example, which results in

$$\frac{a}{d} = \frac{p}{\sqrt{1 - q^2}}.$$

a/d being real results in that the condition for modes (p, q) exist is $q = 0$, which demonstrates that there exists degeneracy between modes $(0, 1)$ and $(p, 0)$ when $a/d = p$. We will have degeneracies between the following modes (see Fig. 2.3):

$$\begin{aligned} (0, 1) \text{ and } (1, 0) \text{ if } \frac{a}{d} = 1, & \quad (0, 1) \text{ and } (2, 0) \text{ if } \frac{a}{d} = 2, \\ (0, 1) \text{ and } (3, 0) \text{ if } \frac{a}{d} = 3, & \quad (0, 1) \text{ and } (p, 0) \text{ if } \frac{a}{d} = p. \end{aligned}$$

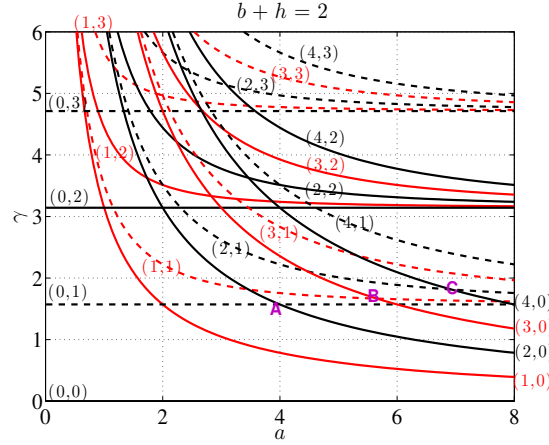


Figure 2.3: Motions of the eigenvalues of the closed rigid cavity as a function of cavity length $a(= a^*/h^*)$, the width of the cavity is $d = b + h = 2$. Degeneracies are found for two modes having the same eigenvalues, for example in the vicinity of crossing “A”, “B”, and “C” labeled in the figure.

However, once the closed system is opened by attaching to the ducts, the eigenvalues of the open system are generally complex. The trajectories of the eigenvalues of the two modes that have crossing in Fig. 2.3 will have avoided crossing in the complex plane. For the open system, we first calculated the K_λ of \mathbf{H}_{eff} as a function of cavity length a with $b = 1$ and $K = 1.6$, see Fig. 2.4(a). For the sake of comparison, Fig. 2.4(b) shows the motions of the real part of eigenvalues K_R of the open system by solving the fixed-point equation Eq. (2.16). Here and in the following, the indices (μ, ν) for the closed cavity are also used to identify the eigenvalues K_λ and K_R . In Figs. 2.4(a) and (b), solid lines label the modes which are symmetric in x , and symbols “◀” for the modes which are antisymmetric. Avoided crossings between the two modes who have the same symmetry in x are observed in both figures, for example between modes $(0,1)$ and $(2,0)$ (labelled by “A”), modes $(1,1)$ and $(3,0)$ (labelled by “B”), etc.. We have reviewed before that for the corresponding closed cavity, those modes will just cross without any coupling (“A”, “B”, and “C” in Fig.2.3). Only the same parity in x -direction has to be satisfied, it is

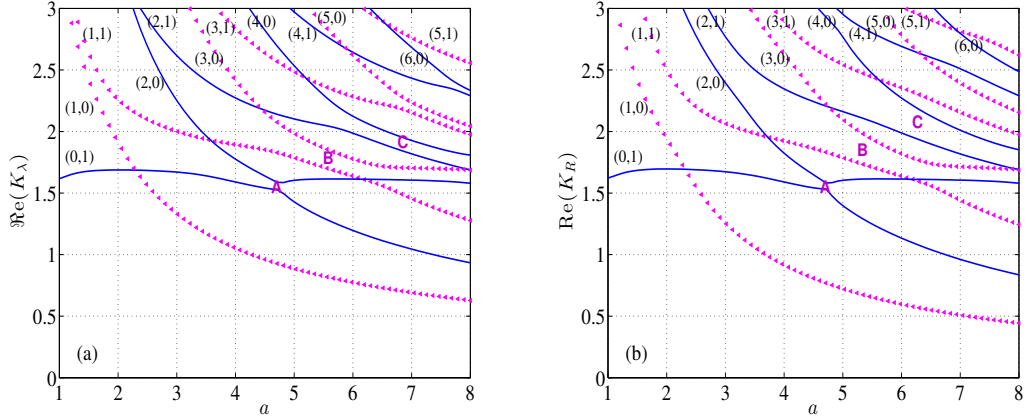


Figure 2.4: (a) Real part of eigenvalues of \mathbf{H}_{eff} , $\Re(K_\lambda)$, as a function of a with $b = 1$, $K = 1.6$. (b) Motions of $\Re(K_R)$ of the open system with varying a by solving the fixed-point equation Eq. (2.16). Solid lines mark x -symmetric modes; symbols “◀” mark x -antisymmetric modes.

because the system we considered is symmetric for $x = a/2$. By the comparison between Fig. 2.4(a) and (b), we can see that, with suitable value of K , the eigenvalues K_λ of \mathbf{H}_{eff} can be used to analyze the coupling effects between two neighbored modes of the open system, for example between mode (0,1) and mode (2,0) by taking $K = 1.6$. One of the advantages to use matrix \mathbf{H}_{eff} , instead of solving the fixed-point equation, is that the eigenvalues K_λ can be obtained easily by solving the eigenvalue problem of the matrix.

To study the interference between two modes, we take avoided crossing “A” in Fig. 2.4(a) as an example, the motions of modes (0,1) and (2,0) as a function of the geometry size are investigated. The results are summarized in Fig. 2.5. By varying cavity length a , crossing and avoided crossing of the real and imaginary parts of K_R for the two modes can be traced under different conditions, i.e. for different values of b . When $b = 0.95$, there exists crossing for the real and avoided crossing for the imaginary parts, see Figs. 2.5(a)(b). Inversely, avoided crossing for the real and crossing for the imaginary parts are observed in Figs. 2.5(d)(e) when $b = 1.05$. The figures also demonstrate that the degeneracy discussed before for the closed cavity now shows avoided crossing for the open system, see Figs. 2.5(c)(f). The similar duct-cavity system has also been investigated by Hein and Koch *et al.* [7], but only the second type of avoided crossing is found (see Fig. 4 [7]). The occurrences of the two types of avoided crossings indicate the existence of EP in the parameter plane (a, b) , i.e. a_{cri} and b_{cri} , at which the two modes will *coalesce*, not only the eigenvalues but also the eigenfunctions. It is exactly due to the shift of the value b from b_{cri} , there always exists avoided crossing in the vicinity of EP with varying the other parameter a , as shown in Figs. 2.5(c)(f).

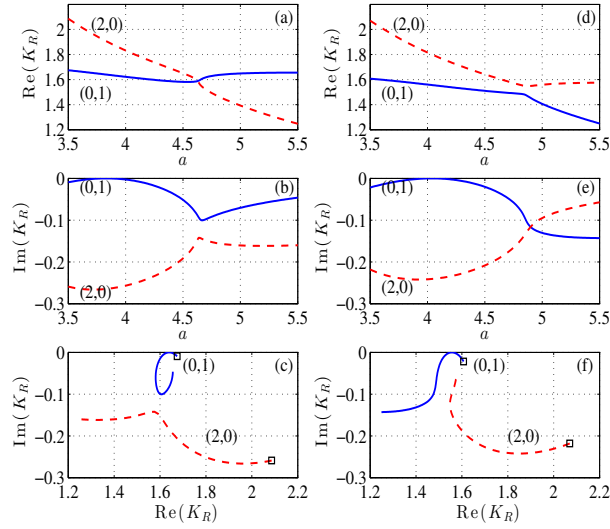


Figure 2.5: Real (a)(d) and imaginary (b)(e) parts of the modes (0, 1) (solid line) and (2, 0) (dashed line) as a function of length a for different values of b : (a)(b)(c) $b = 0.95$ and (d)(e)(f) $b = 1.05$. The trajectories of the modes in the complex plane are shown in (c)(f). The “ \square ” in (c)(f) indicates the starting point. The two modes are in the vicinity of avoided crossing “A” in Fig.2.4.

2.3.2 Trapped mode and Fano resonance

By looking at the trajectories of the eigenvalues of the two modes in the complex plane, we can see that before reaching the EP, the two modes move in a opposite direction and approach to each other; in the vicinity of the EP, a strong repulsion between the two modes is observed, which makes them avoid crossing and move away from each other. However, the important and interesting point is that before the repulsion, the imaginary part of one mode is almost *zero* (see Figs. 2.5(b)(e)), it means that this mode will not have radiation loss, which is the so-called *embedded trapped mode* [15] (we will just call it “trapped mode”).

In Fig. 2.6(a), we show the trajectories of K_R of mode (0,1) as a function of $a \in [3.73, 4.22]$ with $b = 1$ (circle with solid line). A trapped mode is observed at $a = 3.93$ with $b = 1$, marked by the “ \otimes ” in Fig. 2.6(a). For comparison, the motions of K_λ as a function of a with $b = 1$, $K = 1.597$ are also shown in Fig. 2.6(a) (square with dashed line). From the two curves, we can see that the matrix \mathbf{H}_{eff} can be well used to predict the appearances of the trapped modes. To qualitatively characterize the effects of the trapped mode on the sound propagation, the transmission coefficient for the plane wave as a function of K is computed, with $a = 3.93$ and $b = 1$. The results are plotted in Fig. 2.6(b). A transmission peak and dip is observed around $K = 1.597$, it first reaches to “1” and then decreases to “0” sharply (shown clearly in the inset of Fig. 2.6(b)). Smaller

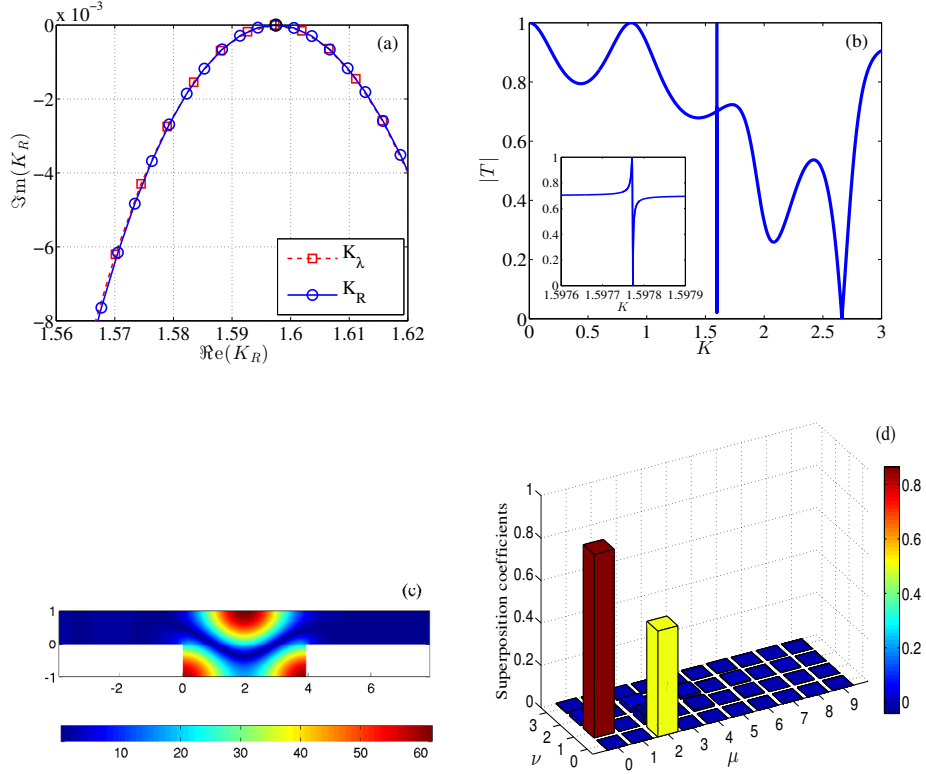


Figure 2.6: (a) Trajectories of resonance (0,1) (blue circle) as a function of a with $b = 1$. The resonance width vanishes at $a = 3.93$ (marked by “ \oplus ”). The motions of K_λ of H_{eff} with $K = 1.597$ is shown by red square. (b) Transmission coefficients as a function of incident frequency K with $a = 3.93$, $b = 1$. (c) The absolute value of the pressure field in the waveguide when the transmission coefficient is zero. (d) The superposition coefficients of the eigenfunctions $\psi_{\mu\nu}(x, y)$ for the trapped mode.

the absolute value of the imaginary part of the trapped mode is, sharper and faster the coefficient changes from “1” to “0”. This asymmetric line profile is one of the main features of the so-called Fano resonance [23], known from atomic physics. This phenomenon is due to the interaction of the trapped mode with the incoming propagating mode.

From the field distribution in the waveguide, Fig. 2.6(c), we see that the pressure field in the cavity is much higher than in the ducts, the trapped mode is confined in the scattering region, a similar pressure profile for the trapped mode is also given in Fig.7(a) by Hein and Koch *et al.* [7]. The eigenfunction of the trapped mode is a strong mixing of the eigenfunctions of mode (0,1) and mode (2,0) of the closed cavity with the superposition coefficients 0.865 and 0.498, respectively. The superposition coefficients of several eigenfunctions $\psi_{\mu,\nu}$, $0 \leq \mu \leq 9, 0 \leq \nu \leq 3$, for the trapped mode are shown in Fig. 2.6(d). The contributions of the other modes are much smaller than of the modes (0,1) and (2,0).

2.3.3 Multimodes interference

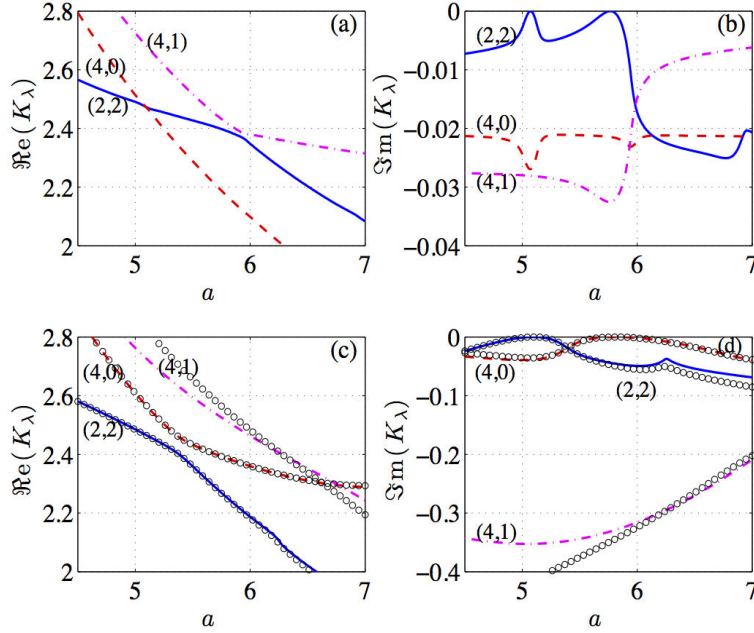


Figure 2.7: Real and imaginary parts of K_λ as a function of a with $b = 2$ for different K : (a)(b) $K = 0.4$ and (c)(d) $K = 2.4$. The resonance frequencies and widths of the system by solving the fixed-point equation are also shown in (c) and (d) by symbols “o”.

In order to have more modes in the frequency range of our interest, the motions of eigenvalues as a function of cavity length a with larger cavity depth, for example $b = 2$, are investigated. In Fig. 2.7, we show the motions of the modes (2,2), (4,0), and (4,1) by considering the eigenvalues of \mathbf{H}_{eff} with different values of K . From Figs. 2.7(a) and (b), crossing for the real and avoided crossing for the imaginary parts are found between modes (2,2) and (4,0), and the opposite phenomenon for modes (2,2) and (4,1). After K passes the critical value K_{cri} , the modes who have crossing (or avoided crossing) for the real part in Figs. 2.7(a)(b) will now have avoided crossing (or crossing), see Figs. 2.7(c)(d). In Figs.2.7(c)(d), the symbols “o” show the resonance frequencies of the open system as a function of the length a by solving Eq. (2.16). We can see from Fig. 2.7(c) that the eigenvalues of \mathbf{H}_{eff} well predict the resonance frequencies of modes (2,2) and (4,0) by taking $K = 2.4$. However for mode (4,1), it works well when the resonance frequency K_R is near 2.4, which exactly satisfies the fixed-point equation. From Figs. 2.7(c)(d), if we only know the resonances K_R of the open system, it is not easy to tell the interference of which modes the second trapped mode is due to. However, with the help of different avoided crossings of K_λ , we can have a more clear sight for the interference of modes (2,2) and (4,1), as shown in Fig. 2.7(a)(b). Looking at the motions of the imaginary parts, two trapped modes are formed, which is due to the interference of modes (2,2) and

(4,0), and of modes (2,2) and (4,1), respectively.

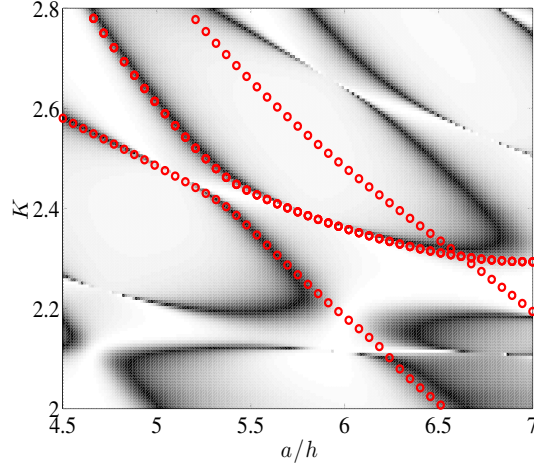


Figure 2.8: Transmission coefficients as a function of both frequency K and cavity length a , with $b = 2$. The dark areas correspond to low transmission coefficient. “ \circ ” indicates the eigenvalues of the open system.

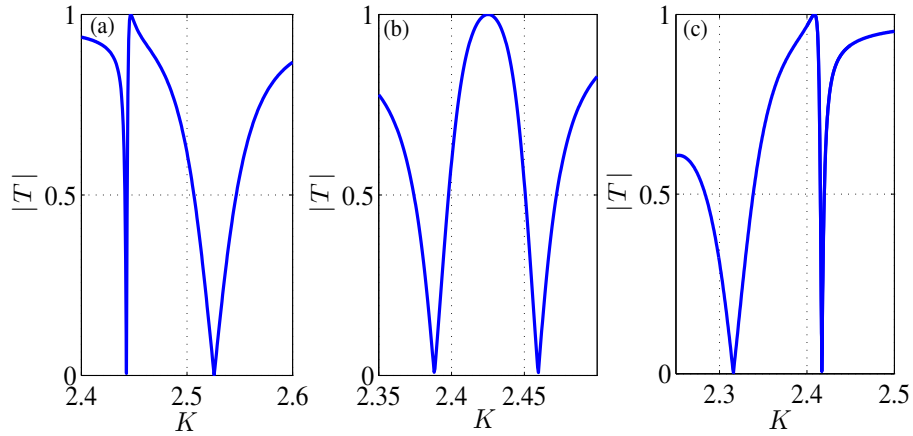


Figure 2.9: Transmission coefficients as a function of frequency K for different cavity lengths (a) $a = 5.2$, (b) $a = 5.4$, (c) $a = 5.6$, with $b = 2$.

In Fig. 2.8, we plot the transmission coefficient as a function of both frequency K and cavity length a , with $b = 2$. The eigenvalues of the resonance K_R of the open system are also given in the same figure, labelled by “ \circ ”. It is remarkable that near the avoided crossing, one can observe the abrupt changes of the transmission coefficients. They appear at the points where the imaginary parts of the modes are zero, see Fig. 2.7(d).

Figure 2.9 shows the transmission coefficients of the plane mode as a function of frequency K with different values of cavity length a , in order to investigate its effects on the transmission spectrum. In Figs. 2.9(a) and (c), two kinds of Fano antisymmetric line-shape in the transmission spectrum are observed. In Fig. 2.9(a), transmission coefficient $|T|$ decreases to “0” first and then increases to “1” sharply. However, it changes in the opposite way in Fig. 2.9(c). We can see from Fig. 2.7(d) that trapped modes are formed around $a = 5.2$, and 5.6 , respectively. Once the incoming propagating mode interferes with the trapped modes, the Fano resonances results. In Fig. 2.9(b), we show the transmission coefficients with the cavity length $a = 5.4$, where the interference between the modes is weak. We can see the sharp transmission dips disappear, while a symmetrical Breit-Wigner (BW) (or Lorentzian) line shape shows up near the frequency of mode (2,2).

2.4 Conclusions

In summary, the couplings of the modes in the open duct-cavity systems are investigated by means of varying a parameter continuously. Instead of computing the complex resonance frequencies of the systems directly, an effective matrix \mathbf{H}_{eff} is introduced to describe the coupling of the modes of the closed system via the attached ducts successfully and efficiently. Consequently, we have obtained various interesting avoided crossings for both the eigenvalues of \mathbf{H}_{eff} and the resonance frequencies of the open system which have the same parity in x -direction. We have shown that the avoided crossings are in the vicinity of the exceptional points.

By matrix \mathbf{H}_{eff} , we can predicts the parameter combinations of the trapped modes very well. Our computation on the transmission coefficients shows very interesting Fano asymmetric line-shape, due to the interference of the trapped modes and the incoming propagating mode. Strong localization of the pressure field in the scattering region is observed, it is a mixing of the eigenfunctions of the two resonances. We have also observed that the sharp dips disappear if the coupling of the modes becomes weak.

In the next chapter, the same mechanism is introduced in a waveguide lined with locally reactive liner, to produce another transmission zero at the frequency of the trapped mode, in addition to the transmission zero observed at the quarter-wavelength frequency of the liner.

Appendix

2.A Derivation of Eqs.(2.9)(2.10)(2.12)

2.A.1 Derivation of Eq. (2.9)

Multiplying Eq. (3.1) by $\psi_{\mu\nu}(x, y)$, integrating over the closed cavity, we obtain

$$\int_0^a \int_0^h \psi_{\mu\nu} \left(\frac{\partial^2 p}{\partial x^2} + \frac{\partial^2 p}{\partial y^2} \right) dx dy = -K^2 \int_0^a \int_0^h \psi_{\mu\nu} p dx dy, \quad (2.19)$$

Applying an integration by parts for the left side of Eq. (3.24), substituting Eq. (3.5) into the resulting equation, we obtain

$$\begin{aligned} & \int_0^h \left(\psi_{\mu\nu} \frac{\partial p}{\partial x} - \frac{\partial \psi_{\mu\nu}}{\partial x} p \right) \Big|_{x=0}^{x=a} dy + \int_0^a \left(\psi_{\mu\nu} \frac{\partial p}{\partial y} - \frac{\partial \psi_{\mu\nu}}{\partial y} p \right) \Big|_{y=0}^{y=h} dx \\ & = -(K^2 - \gamma_{\mu\nu}^2) \int \int \psi_{\mu\nu} p dx dy. \end{aligned} \quad (2.20)$$

The eigenfunctions $\psi_{\mu\nu}$ of the closed cavity satisfy the rigid boundary conditions on all the walls, Eq. (3.6). Substituting the rigid boundary conditions for both $p(x, y)$ and $\psi_{\mu\nu}$ into Eq. (3.25), results in the following equation

$$\int_0^h \left(\psi_{\mu\nu} \frac{\partial p}{\partial x} \right) \Big|_{x=a}^{x=0} dy = (K^2 - \gamma_{\mu\nu}^2) \int \int \psi_{\mu\nu} p dx dy, \quad (2.21)$$

Using the orthogonality property of eigenfunctions $\psi_{\mu\nu}$ and Eq. (3.4), the upper equation can be written in a matrix form, i.e. Eq. (2.9).

2.A.2 Derivation of Eq. (2.10)

By Eq. (2.2), the first derivative of the pressure with respect to x at the interfaces, $\partial p_m / \partial x$ is taken, and then substituted into the right side of the Eq. (2.9). The resulting equations are written in a matrix form,

$$\mathbf{A} \mathbf{K}_N = \mathbf{j} (\mathbf{I} - \mathbf{S}^T) \mathbf{K}_M \mathbf{Q}_1, \quad (2.22)$$

where \mathbf{A} is a $2M \times N$ matrix consisting of the vectors \vec{a}_m , the upper M rows correspond to wave incident from the left side, and the remaining from the right side. The elements

of matrix \mathbf{Q}_1 are

$$\mathbf{Q}_1 = \begin{pmatrix} \int_0^1 \phi_1(y') \psi_1(0, y') dy' \\ \vdots \\ \int_0^1 \phi_M(y') \psi_N(0, y') dy' \\ \int_0^1 \phi_1(y') \psi_1(a, y') dy' \\ \vdots \\ \int_0^1 \phi_M(y') \psi_N(a, y') dy' \end{pmatrix}. \quad (2.23)$$

By matrix \mathbf{A} , the pressure in the scattering region is then written in a vector form,

$$\vec{p}(x, y) = j(\mathbf{I} - \mathbf{S}^T) \mathbf{K}_M \mathbf{Q}_1 \mathbf{K}_N^{-1} \vec{\psi}(x, y). \quad (2.24)$$

where $\vec{p} = (p_1, p_2, \dots, p_m, \dots)^T$.

By the continuity condition of the pressure at the interfaces $x = 0, a$, results in two equations. Multiplying the two equations by ϕ_m , writing them in a matrix form, we have

$$j[\mathbf{I} - \mathbf{S}^T] \mathbf{K}_M \mathbf{Q}_1 \mathbf{K}_N^{-1} \mathbf{Q}_1^T = [\mathbf{I} + \mathbf{S}^T]. \quad (2.25)$$

By Eq. (2.25), we end up with the scattering matrix of Eq. (2.10).

2.A.3 Derivation of Eq. (2.12)

Due to the symmetry property of the matrix \mathbf{S} , Eq. (2.10) can be rewritten as

$$\mathbf{S} = -\frac{\mathbf{I} - j\mathbf{Q}\mathbf{K}_M}{\mathbf{I} + j\mathbf{Q}\mathbf{K}_M} = -\mathbf{I} + \frac{2j\mathbf{Q}\mathbf{K}_M}{\mathbf{I} + j\mathbf{Q}\mathbf{K}_M}. \quad (2.26)$$

Now we expand the denominator in Eq. (2.26) into a geometric series [8],

$$\begin{aligned} \mathbf{S} &= -\mathbf{I} + 2j\mathbf{Q}_1 \frac{1}{\mathbf{K}_N} \mathbf{Q}_1^T \mathbf{K}_M \sum_{q=0}^{\infty} \left(-j\mathbf{Q}_1 \frac{1}{\mathbf{K}_N} \mathbf{Q}_1^T \mathbf{K}_M \right)^q \\ &= -\mathbf{I} + 2j\mathbf{Q}_1 \frac{1}{\mathbf{K}_N} \sum_{q=0}^{\infty} \left(-j\mathbf{Q}_1^T \mathbf{K}_M \mathbf{Q}_1 \frac{1}{\mathbf{K}_N} \right)^q \mathbf{Q}_1^T \mathbf{K}_M \\ &= -\mathbf{I} + 2j\mathbf{Q}_1 \frac{1}{\mathbf{K}_N} \frac{1}{1 + j\mathbf{R}_1^T \mathbf{K}_M \mathbf{R}_1 \frac{1}{\mathbf{K}_N}} \mathbf{Q}_1^T \mathbf{K}_M \\ &= -\mathbf{I} + 2j\mathbf{Q}_1 \frac{1}{\mathbf{K}_N + j\mathbf{R}_1^T \mathbf{K}_M \mathbf{R}_1} \mathbf{Q}_1^T \mathbf{K}_M \end{aligned} \quad (2.27)$$

By the expression of \mathbf{K}_N , the upper equation results in the Eq. (2.12).

Bibliography

- [1] Y. Aurégan. Low frequency sound propagation in a coaxial cylindrical duct: Application to sudden area expansions and to dissipative silencers. *Journal of Sound and Vibration*, 243(3):461 – 473, 2001.
- [2] Almas Sadreev, Evgeny Bulgakov, and Ingrid Rotter. Bound states in the continuum in open quantum billiards with a variable shape. *Phys. Rev. B*, 73(23), June 2006.
- [3] Gonzalo Ordonez, Kyungsun Na, and Sungyun Kim. Bound states in the continuum in quantum-dot pairs. *Phys. Rev. A*, 73:022113, Feb 2006.
- [4] S. Rotter, F. Libisch, J. Burgdörfer, U. Kuhl, and H.-J. Stöckmann. Tunable fano resonances in transport through microwave billiards. *Phys. Rev. E*, 69:046208, Apr 2004.
- [5] Yong Xu, Yi Li, Reginald K. Lee, and Amnon Yariv. Scattering-theory analysis of waveguide-resonator coupling. *Phys. Rev. E*, 62:7389–7404, Nov 2000.
- [6] Shanhui Fan, M.F. Yanik, Zheng Wang, Sunil Sandhu, and M.L. Povinelli. Advances in theory of photonic crystals. *Lightwave Technology, Journal of*, 24(12):4493–4501, Dec 2006.
- [7] Stefan Hein, Werner Koch, and Lothar Nannen. Trapped modes and fano resonances in two-dimensional acoustical duct-cavity systems. *J. Fluid Mech.*, 692:257–287, February 2012.
- [8] H.-J. Stöckmann, E. Persson, Y.-H. Kim, M. Barth, U. Kuhl, and I. Rotter. Effective hamiltonian for a microwave billiard with attached waveguide. *Phys. Rev. E*, 65(6), June 2002.
- [9] Ingrid Rotter. A non-hermitian hamilton operator and the physics of open quantum systems. *J. Phys. A: Math.Theor.*, 42(15):153001, April 2009.
- [10] F. Ursell. Trapping modes in the theory of surface waves. *Proc. Camb. Phil. Soc.*, 47:347–358, January 1951.

-
- [11] D. S. Jones. The eigenvalues of $\nabla^2 u + \lambda u = 0$ when the boundary conditions are given in semi-infinite domain. *Proc. Camb. Phil. Soc.*, 49:668–684, January 1953.
- [12] V. Pagneux. Trapped modes and edge resonances in acoustics and elasticity. *CISM International Centre for Mechanical Sciences*, 547:181–223, January 2013.
- [13] C. M. Linton and P. McIver. Embedded trapped modes in water waves and acoustics. *Wave motion*, 45:16–29, January 2007.
- [14] von Neumann and E. P. Wigner. Über merkwürdige diskrete eigenwerte. *Phys. Z*, 30:465–467, 1929.
- [15] Yuting Duan, Werner Koch, Chris M. Linton, and Maureen McIVER. Complex resonances and trapped modes in ducted domains. *J. Fluid Mech.*, 571:119, January 2007.
- [16] H. Friedrich and D. Wintgen. Interfering resonances and bound states in the continuum. *Phys. Rev. A*, 32(6):3231–3242, December 1985.
- [17] P. M. Morse and K. U. Ingard. *Theoretical acoustics*. McGraw-Hill Book Company, New York, January 1968.
- [18] W D Heiss and A L Sannino. Avoided level crossing and exceptional points. *J. Phys. A: Math. Gen.*, 23(7):1167–1178, April 1990.
- [19] W D Heiss. Repulsion of resonance states and exceptional points. *Phys. Rev. E*, 61(1):929–932, January 2000.
- [20] G. Cattapan and P. Lotti. Fano resonances in stubbed quantum waveguides with impurities. *Eur. Phys. J. B*, 60:51–60, 2007.
- [21] Arkady M. Satanin and Yong S. Joe. Fano interference and resonances in open systems. *Phys. Rev. B*, 71, June 2005.
- [22] Yong S Joe, Arkady M Satanin, and Chang Sub Kim. Classical analogy of fano resonances. *Physica Scripta*, 74(2):259, 2006.
- [23] U. Fano. Effects of configuration interaction on intensities and phase shifts. *Phys. Rev.*, 124(6):1866–1878, December 1961.
- [24] Boris Luk'yanchuk, Nikolay I. Zheludev, Stefan A. Maier, Naomi J. Halas, Peter Nordlander, Harald Giessen, and Chong Tow Chong. The fano resonance in plasmonic nanostructures and metamaterials. *Nature Mater.*, 9(9):707–715, September 2010.
- [25] Andrey E. Miroshnichenko, Sergej Flach, and Yuri S. Kivshar. Fano resonances in nanoscale structures. *Rev. Mod. Phys.*, 82(3):2257–2298, August 2010.

-
- [26] S. Hein, W. Koch, and L. Nannen. Fano resonances in acoustics. *J. Fluid Mech.*, 664:238–264, January 2010.
- [27] E. Wigner and L. Eisenbud. Higher angular momenta and long range interaction in resonance reactions. *Phys. Rev.*, 72(1):29–41, July 1947.
- [28] P. Racec, E. Racec, and H. Neidhardt. Evanescent channels and scattering in cylindrical nanowire heterostructures. *Phys. Rev. B*, 79(15), April 2009.
- [29] V. Pagneux, N. Amir, and J. Kergomard. A study of wave propagation in varying cross-section waveguides by modal decomposition. Part I. Theory and validation. *J. Acoust. Soc. Am.*, 100(4):2034–2048, 1996.
- [30] W.P. Bi, V. Pagneux, D. Lafarge, and Y. Aurégan. Modelling of sound propagation in a non-uniform lined duct using a multi-modal propagation method. *J. Sound Vib.*, 289(4-5):1091–1111, February 2006.

Chapter 3

Fano resonance scatterings in waveguides with impedance boundary conditions

The first strategy we introduced in the previous chapter is now applied here to a waveguide lined with a locally reacting material.

In this chapter¹, the resonance scattering theory is used to study the sound propagation in a waveguide with a portion of its wall lined by a locally reacting material. The objective is to understand the effects of the mode coupling in the lined portion on the transmission. It is shown that a zero in the transmission is present when a real resonance frequency of the open system, i.e. the lined portion of the waveguide which is coupled to the two semi-infinite rigid ducts, is equal to the incident frequency. This transmission zero occurs as a Fano resonance - due to the excitation of a trapped mode in the open system. The trapped mode is formed by the interferences of two neighbored modes with complex resonance frequencies. It is also linked to the avoided crossing of eigenvalues of these two modes, which occurs near an exceptional point (a subject which has attracted much attention in recent years in different physical domains). The real and complex resonance frequencies of the open system are determined by an equivalent eigenvalue problem of matrix \mathbf{H}_{eff} , which describes the eigenvalue problem defined in the finite lined portion (scattering region). With the aid of the eigenvalues and eigenfunctions of matrix \mathbf{H}_{eff} , the usual acoustic resonance scattering formula can be extended to describe the coupling effects between the scattering region and the rigid parts of the waveguide.

1. This chapter in its current form has been recently accepted by J. Acous. Soc. Am..

3.1 Introduction

Acoustic liners are commonly used in noise control devices for duct systems. Typical applications include silencers for ventilation systems, wall treatments for aircraft engines, and silencers for industrial gas turbines, for review articles see, e.g., Refs. 1 and 2. To increase the liner efficiency, various strategies can be used. One is to find a new material design for which the impedance is close to its optimal value in the targeted range of frequencies [3, 4]. Another strategy is to take advantage of the acoustic impedance changes (like discontinuities) in axial [5, 6, 7] or circumferential [8, 9] segments, or both of them [10, 11, 12, 13]. The strategy used in this paper is different: The idea is to couple the incoming propagative mode in the waveguide with the modes localized in the lined region. As an example, a very simple 2D model with a portion of the waveguide lined by a uniform liner is analyzed in this paper.

Such interferences between resonances and scattering appear in Fano resonances (for review articles see, for example, Refs. 14 and 15, and the references therein). In contrast to the conventional isolated resonances scattering, Fano resonance is explained by constructive and destructive interferences between a resonance (trapped mode) or a complex resonance (quasi-trapped mode) and the background or nonresonant scattering [16, 17]. A transmission zero is produced when a real resonance frequency is equal to the incident frequency [18].

One of the crucial ingredients to form a Fano resonance is to have trapped mode with a real resonance frequency. Trapped modes are localized oscillations in unbounded media and do not radiate energy to infinity. They were first observed experimentally in acoustics by Parker in 1966 [19]. Discrete trapped modes may exist below the first cut-off frequency of the transverse modes, provided that some kinds of defect or variations of geometry exist [20, 21]. Discrete trapped modes may also exist above the first cut-off frequency for specific parameter combinations, they are called embedded trapped modes [20] or bound states in continuum (BIC) in quantum mechanics [22]. Friedrich and Wintgen [23] demonstrated that BIC is a natural feature of common physical situations, and can occur due to the interference of resonances. They have linked BICs directly to the phenomenon of an avoided crossing of neighbored resonance states (modes with complex eigenvalues). Recently, BICs in the vicinity of exceptional points were also found in open billiards [24]. Exceptional points are the points in a two-dimensional parameter space, where not only the eigenvalues but also the eigenfunctions of a non-Hermitian operator coalesce [25, 26, 27]. Sadreev *et al.* [24] found that the BICs are close to the points of degeneracy [28] of the closed system, which are the points in a two-dimensional parameter space where only the eigenvalues of the Hermitian operator coalesce, while the corresponding eigenfunctions are still orthogonal. When the system is opened, the degeneracies are lifted and avoided crossings occur.

Fano resonance scatterings in acoustics and their relations with trapped modes in waveguides including obstacles or in duct-cavity systems have been studied by Hein

et al. [18, 29]. They used a finite-element method to compute numerically the acoustic resonances as well as the transmission and reflection for an incoming duct mode. They obtained complex resonance frequencies and the corresponding eigenfunctions. The complex resonance frequencies are the positions of the poles of scattering matrix of the corresponding scattering problem. Fano resonance scatterings were related to three types of trapped modes: antisymmetric (about duct axis) trapped modes below the first cut-off frequency, embedded trapped modes linked to avoided crossings of resonances, and trapped modes associated with Fabry-Pérot interferences between cavities.

In this paper, we study the sound propagation in a waveguide lined on a portion with a locally reacting material by the resonance scattering theory [30]. The objective is to understand the effects of the mode coupling on the transmission of the lined portion. We show that by varying a control parameter (the section length or the product of the lined admittance and the frequency), two neighbored modes with complex resonance frequencies interfere in the scattering region: the lined portion opened to the two semi-infinite rigid waveguides. In the vicinity of an exceptional point, where the eigenvalues and eigenfunctions coalesce, one mode turns to be trapped, the corresponding resonance frequency (eigenvalue) is real. A transmission zero is present when the real resonance frequency is equal to the incident frequency. This transmission zero occurs as a Fano resonance, due to the excitation of a trapped mode in the open system (section 3.3).

In section 3.2, we derive the Scattering matrix (**S** matrix). For that, we project the Helmholtz equation over the eigenfunctions of the rigid closed counterpart of the scattering region which form an orthogonal and complete function basis. The used eigenfunctions include the transverse and axial components, thus this method generalizes the Multimodal method [11] in which the wave function is expanded only in terms of transverse eigenfunctions. We express the scattering matrix **S** in terms of an effective matrix \mathbf{H}_{eff} . The matrix \mathbf{H}_{eff} describes the complex resonances of the scattering region. Its eigenvalues are complex and give the poles of the **S** matrix. With the help of its eigenfunctions, we can extend the traditional acoustic resonance scattering formula [30] to describe the coupling effects between the scattering region and the rigid waveguide.

3.2 Model

We consider the acoustic scattering problem in a two-dimensional infinite waveguide lined over a finite length a^* with a locally reacting material, as shown in Fig. 3.1. The waveguide is decomposed into three parts: two semi-infinite rigid waveguides $x^* \leq 0$ and $x^* \geq a^*$ (regions I and III, respectively), and one scattering region (region II). Here, asterisk denotes dimensional quantities. In the following, all the quantities are non-dimensionalized. Sound pressure p and coordinates (x and y) are normalized by taking $p = p^*/(\rho_0^* c_0^{*2})$ and $(x, y) = (x^*/h^*, y^*/h^*)$, respectively, where ρ_0^* is the air density, c_0^* is the sound velocity, and h^* is the height of the waveguide. Time dependence is assumed as

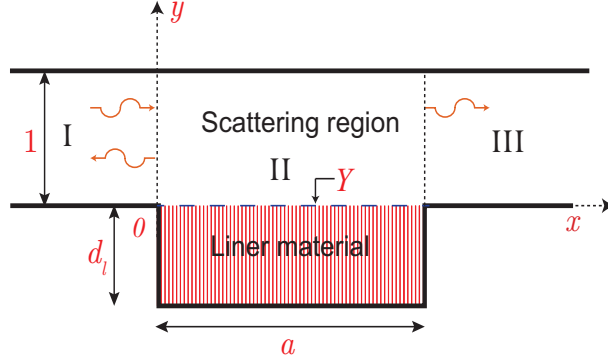


Figure 3.1: A two-dimensional infinite waveguide lined with a locally reacting material of normalized length a . Y refers to the normalized admittance. The closed counterpart of the scattering region is called *lined closed cavity*, with rigid conditions at $x = 0$ and $x = a$.

$\exp(-j\omega^*t^*)$ and will be omitted in the following, where ω^* is the circular frequency. The sound pressure $p(x, y)$ in the waveguide satisfies the non-dimensional Helmholtz equation

$$\left(\frac{\partial^2}{\partial x^2} + \frac{\partial^2}{\partial y^2} + K^2 \right) p(x, y) = 0, \quad (3.1)$$

where $K = (\omega^*/c_0^*)h^*$ refers to dimensionless frequency. The transverse boundary conditions in regions I, III, and II are

$$\frac{\partial p}{\partial y} \Big|_{y=0 \text{ and } 1} = 0 \quad (\text{for regions I and III}) \quad (3.2)$$

and

$$\frac{\partial p}{\partial y} \Big|_{y=0} = -jKYp \quad \text{and} \quad \frac{\partial p}{\partial y} \Big|_{y=1} = 0 \quad (\text{for region II}), \quad (3.3)$$

respectively, where Y is the normalized admittance of the liner material.

Inspired by the R-matrix method [32, 33], the sound pressure $p(x, y)$ in region II is expanded in terms of an orthogonal and complete set of functions $\psi_{\mu\nu}(x, y)$

$$p(x, y) = \sum_{\mu=0}^{N_x-1} \sum_{\nu=0}^{N_y-1} a_{\mu\nu} \psi_{\mu\nu}(x, y) = \boldsymbol{\psi}^T \mathbf{a}, \quad (3.4)$$

where the sums have been truncated by N_x and N_y , " T " refers to transpose, and $a_{\mu,\nu}$ are the expansion coefficients. $\boldsymbol{\psi}$ is a column vector, its elements are arranged as $(\mu, \nu) = (0, 0), (0, 1), \dots, (0, N_y - 1), (1, 0), (1, 1), \dots, (1, N_y - 1), \dots, (N_x - 1, 0), (N_x - 1, 1), \dots, (N_x -$

1, $N_y - 1$). We choose $\psi_{\mu,\nu}$ to be the eigenfunctions of *rigid closed cavity* defined by

$$\nabla^2 \psi_{\mu\nu} = -\gamma_{\mu\nu}^2 \psi_{\mu\nu}, \quad (3.5)$$

$$\frac{\partial \psi_{\mu\nu}}{\partial x} \Big|_{x=0 \text{ and } a} = 0, \quad \frac{\partial \psi_{\mu\nu}}{\partial y} \Big|_{y=0 \text{ and } 1} = 0. \quad (3.6)$$

By solving the eigenproblem of Eqs. (3.5) and (3.6), the eigenfunctions $\psi_{\mu\nu}$ and eigenvalues $\gamma_{\mu\nu}$ are given as $\psi_{\mu\nu} = (1/\sqrt{\Lambda_x \Lambda_y}) \cos(\mu\pi x/a) \cos(\nu\pi y)$ and $\gamma_{\mu\nu} = \sqrt{(\mu\pi)^2/a^2 + (\nu\pi)^2}$, respectively, where $\Lambda_x = \sqrt{2 - \delta_{0,\nu}}/\sqrt{a}$ and $\Lambda_y = \sqrt{2 - \delta_{0,\nu}}$ are normalization coefficients, with $\delta_{i,j} = 1$ if $i = j$, else $\delta_{i,j} = 0$.

It needs to be noted that the eigenfunctions $\psi_{\mu\nu}$ in Eq. (3.4) include the transverse and axial components, instead of only transverse component as used in Multimodal method [11], and that any complete set of functions can be used but the present choice defined in Eqs. (5) and (6) is one of the most convenient. In this paper, we use "modes" to refer to the 2D cavity modes, and "transverse modes" to refer to the 1D duct modes.

Multiplying Eq. (3.1) by ψ , integrating over x and y , applying Green's theorem, and using Eq. (3.5) and the boundary conditions Eq. (3.6), we obtain

$$p(x, y) = \int_0^1 \left[Q(x, y, 0, y') \frac{\partial p(x', y')}{\partial x'} \Big|_{x'=0} - Q(x, y, a, y') \frac{\partial p(x', y')}{\partial x'} \Big|_{x'=a} \right] dy', \quad (3.7)$$

(see Appendix I.1), where

$$Q(x, y, x', y') = \boldsymbol{\psi}^T(x, y) [K^2 \mathbf{I} - \mathbf{H}_{\text{lcc}}]^{-1} \boldsymbol{\psi}(x', y'). \quad (3.8)$$

In Eq. (3.8), \mathbf{I} refers to identity matrix, $\mathbf{H}_{\text{lcc}} = \boldsymbol{\Gamma} - jKY\mathbf{C}^{\text{lcc}}$, where $\boldsymbol{\Gamma}$ is a diagonal matrix with elements $\gamma_{\mu\nu}^2$, "lcc" refers to lined closed cavity, and \mathbf{C}^{lcc} is a block diagonal matrix, its elements can be calculated analytically by

$$C_{\mu\nu,\mu'\nu'}^{\text{lcc}} = \int_0^a \psi_{\mu\nu}(x', 0) \psi_{\mu'\nu'}(x', 0) dx'. \quad (3.9)$$

With the help of Eq. (3.26) in Appendix I.1, it is clear that the eigenvalue problem of matrix \mathbf{H}_{lcc} is equivalent to the eigenvalue problem of the *lined closed cavity* with the admittance on the bottom wall (defined in Appendix II for clarity).

Equation (3.7) links the sound pressure in the scattering region (II) with its first x -derivative at the interfaces between the scattering region and the other two regions (I and III).

The sound pressure is written as a sum of the incident (amplitudes c_m) and reflected

transverse modes for region I, and only transmitted transverse modes for region III

$$p(x, y) = \begin{cases} \sum_{m=0}^{M-1} c_m e^{jK_m^x x} \phi_m(y) + \sum_{m=0}^{M-1} \sum_{m'=0}^{M-1} R_{m,m'} c_m e^{-jK_{m'}^x x} \phi_{m'}(y), & x \leq 0, \\ \sum_{m=0}^{M-1} \sum_{m'=0}^{M-1} T_{m,m'} c_m e^{jK_{m'}^x (x-a)} \phi_{m'}(y), & x \geq a, \end{cases} \quad (3.10)$$

where $R_{m,m'}$ and $T_{m,m'}$ refer to the reflection and transmission coefficients, and M is the truncation number. $K_m^x = \sqrt{K^2 - \alpha_m^2}$ are axial wavenumbers of transverse mode m in the rigid ducts. α_m and ϕ_m are the eigenvalues and eigenfunctions of transverse modes in regions I and III, they are given as $\alpha_m = m\pi$ and $\phi_m = \Lambda \cos(\alpha_m y)$, with $\Lambda = \sqrt{2 - \delta_{0,m}}$ the normalization coefficients. Equation (4.22) is written in matricial form as

$$p(x, y) = \begin{cases} \phi^T E_0^+ \mathbf{c} + \phi^T E_0^- \mathbf{R} \mathbf{c}, & x \leq 0, \\ \phi^T E_a^+ \mathbf{T} \mathbf{c}, & x \geq a, \end{cases} \quad (3.11)$$

where E_0^+ , E_0^- , and E_a^+ are $(M \times M)$ diagonal matrices with the elements $e^{jK_m^x x}$, $e^{-jK_m^x x}$, and $e^{jK_m^x (x-a)}$, respectively. ϕ is a $(M \times 1)$ column vector, its elements are the eigenfunctions ϕ_m .

Substituting Eq. (3.11) into Eq. (3.7) at $x = 0$ and $x = a$, we obtain

$$\mathbf{l}_M + \mathbf{R} = j\mathbf{C}_0^T (K^2 \mathbf{I} - \mathbf{H}_{lcc})^{-1} (\mathbf{C}_0 \mathbf{K}^\times (\mathbf{l}_M - \mathbf{R}) - \mathbf{C}_a \mathbf{K}^\times \mathbf{T}), \quad (3.12)$$

$$\mathbf{T} = j\mathbf{C}_a^T (K^2 \mathbf{I} - \mathbf{H}_{lcc})^{-1} (\mathbf{C}_0 \mathbf{K}^\times (\mathbf{l}_M - \mathbf{R}) - \mathbf{C}_a \mathbf{K}^\times \mathbf{T}), \quad (3.13)$$

where \mathbf{K}^\times is a $(M \times M)$ diagonal matrix with elements K_m^x , and \mathbf{l}_M is a $(M \times M)$ identity matrix. The elements of matrices \mathbf{C}_0 and \mathbf{C}_a are

$$C_{0(a),\mu\nu,m} = \int_0^1 \psi_{\mu\nu}(x' = 0(a), y') \phi_m(y') dy', \quad (3.14)$$

where \mathbf{C}_0 and \mathbf{C}_a have dimensions $N \times M$ with $N = N_x \cdot N_y$. Due to the orthogonality between the term $\cos(\nu\pi y)$ in $\psi_{\mu\nu}$ and the function ϕ_m , elements $C_{0(a),\mu\nu,m}$ will be zero if $\nu \neq m$. From Eqs. (3.12) and (3.13), we obtain

$$\begin{bmatrix} \mathbf{R} \\ \mathbf{T} \end{bmatrix} = [\mathbf{l}_{2M} + j\mathbf{G}\mathbf{K}_{2M}^\times]^{-1} \{ -[\mathbf{l}_M, \mathbf{0}_M]^T + j\mathbf{C}_{0a}^T [K^2 \mathbf{I} - \mathbf{H}_{lcc}]^{-1} \mathbf{C}_0 \mathbf{K}^\times \}, \quad (3.15)$$

where $\mathbf{G} = \mathbf{C}_{0a}^T (K^2 \mathbf{I} - \mathbf{H}_{lcc})^{-1} \mathbf{C}_{0a}$, $\mathbf{C}_{0a} = [\mathbf{C}_0, \mathbf{C}_a]$ is a $(N \times 2M)$ matrix, \mathbf{l}_{2M} is a $(2M \times 2M)$ identity matrix, \mathbf{K}_{2M}^\times is a $(2M \times 2M)$ block diagonal matrix with two $(M \times M)$ diagonal matrices \mathbf{K}^\times on its main diagonal, and $\mathbf{0}_M$ is a $(M \times M)$ zero matrix.

If we assume that the problem is symmetric, the scattering matrix can be written

as

$$\mathbf{S} = \begin{bmatrix} \mathbf{R} & \mathbf{T} \\ \mathbf{T} & \mathbf{R} \end{bmatrix} = [\mathbf{I}_{2M} + j\mathbf{G}\mathbf{K}_{2M}^x]^{-1} [-\mathbf{I}_{2M} + j\mathbf{G}\mathbf{K}_{2M}^x]. \quad (3.16)$$

The scattering matrix \mathbf{S} can be expressed as [34]

$$\mathbf{S} = -\mathbf{I}_{2M} + 2j\mathbf{C}_{0a}^T [\mathbf{K}^2\mathbf{I} - \mathbf{H}_{\text{eff}}]^{-1} \mathbf{C}_{0a}\mathbf{K}_{2M}^x, \quad (3.17)$$

(see Appendix I.2), under the condition that $\mathbf{K}^2\mathbf{I} - \mathbf{H}_{\text{eff}}$ can be inverted, where

$$\mathbf{H}_{\text{eff}} = \mathbf{H}_{\text{Icc}} - j\mathbf{C}_{0a}\mathbf{K}_{2M}^x\mathbf{C}_{0a}^T. \quad (3.18)$$

The eigenvalues K_λ and eigenfunctions $\tilde{\varphi}_\lambda = \boldsymbol{\psi}^T \mathbf{V}_\lambda$ are defined by the eigenproblem of matrix \mathbf{H}_{eff} ,

$$\mathbf{H}_{\text{eff}} \mathbf{V}_\lambda = K_\lambda^2 \mathbf{V}_\lambda. \quad (3.19)$$

They describe the complex resonances of scattering region II, which is opened to infinities through regions I and III, and truncated at the interfaces, $x = 0$ and $x = a$. The elements of vector $\boldsymbol{\psi}$ are the eigenfunctions of the rigid closed cavity defined by Eqs. (3.5) and (3.6). Because the eigenfunctions $\tilde{\varphi}_\lambda$ in scattering region II are non-separable in x and y , we use only one index λ to describe the eigenvalues K_λ and the eigenfunctions $\tilde{\varphi}_\lambda$.

With the help of eigenvalues K_λ and eigenvectors \mathbf{V}_λ , Eq. (3.17) can be written as a resonance form

$$\begin{aligned} \mathbf{S} &= -\mathbf{I}_{2M} + 2j\mathbf{C}_{0a}^T \mathbf{V} [\mathbf{K}^2 \mathbf{V} \mathbf{V}^{-1} - \mathbf{V} \mathbf{H}_{\text{eff}} \mathbf{V}^{-1}]^{-1} \mathbf{V}^T \mathbf{C}_{0a} \mathbf{K}_{2M}^x \\ &= -\mathbf{I}_{2M} + 2j\tilde{\mathbf{C}}_{0a}^T [\mathbf{K}^2 \mathbf{I} - \mathbf{K}_\lambda]^{-1} \tilde{\mathbf{C}}_{0a} \mathbf{K}_{2M}^x, \end{aligned} \quad (3.20)$$

where \mathbf{K}_λ is a $(N \times N)$ diagonal matrix with K_λ^2 its main elements. \mathbf{V} is a $(N \times N)$ matrix with its columns the eigenvectors \mathbf{V}_λ of matrix \mathbf{H}_{eff} . \mathbf{H}_{eff} is a symmetric non-Hermitian matrix, its eigenvectors are bi-orthogonal. $\mathbf{V}^{-1} = \mathbf{V}^T$ has been used to obtain Eq. (3.20). Matrix $\tilde{\mathbf{C}}_{0a}$ is defined as

$$\begin{aligned} \tilde{\mathbf{C}}_{0a} = \mathbf{V}^T \mathbf{C}_{0a} &= \int_0^h \mathbf{V}^T [\boldsymbol{\psi}(x' = 0, y') \boldsymbol{\phi}^T(y'), \boldsymbol{\psi}(x' = a, y') \boldsymbol{\phi}^T(y')] dy' \\ &= \int_0^h [\tilde{\boldsymbol{\varphi}}(x' = 0, y') \boldsymbol{\phi}^T(y'), \tilde{\boldsymbol{\varphi}}(x' = a, y') \boldsymbol{\phi}^T(y')] dy', \end{aligned} \quad (3.21)$$

where $\tilde{\boldsymbol{\varphi}}(x' = 0, y')$ and $\tilde{\boldsymbol{\varphi}}(x' = a, y')$ are $(N \times 1)$ vectors with elements the eigenfunctions $\tilde{\varphi}_\lambda$ of scattering region II at $x' = 0$ and $x' = a$, respectively. Matrix $\tilde{\mathbf{C}}_{0a}$ describes the couplings of the scattering region II with regions I and III. Equation (3.20) is not valid at exceptional points at which the eigenvalues and eigenfunctions coalesce, and therefore \mathbf{V}^{-1} is singular.

Equation (20) shows that the poles K_{pole} of the scattering matrix \mathbf{S} are the eigen-

values of \mathbf{H}_{eff}

$$K_{\text{pole}} = K_{\lambda} \quad (3.22)$$

when $\Re(K_{\lambda}) = K$. It is well known [30, 31] that the poles of scattering matrix are precisely the complex resonance frequencies of the scatter. Therefore, using Eq. (20), we show that the original complex resonance problem of the open system defined in Fig. 3.1 and by Eqs. (3.1), (3.2), and (3.3) with the radiation conditions $p(x, y) \propto e^{\pm jK_m^z x}$ at $x \rightarrow \pm\infty$ is reduced to an eigenvalue problem of matrix \mathbf{H}_{eff} , which describes the eigenvalue problem defined in the scattering region (region II). It is noted that the complex resonances are calculated in Refs. 18 and 29 by finite element method with absorbing boundary conditions.

Equation (3.20) extends the traditional acoustic resonance scattering formula [30, 31], in which the complex eigenfrequencies of scattering region give the resonance poles, to include the coupling effects between scattering region and rigid waveguides.

3.3 Results and discussions

First, we show how the trapped modes with real resonance frequencies occur in the vicinity of exceptional points and how they are linked to avoided crossings of the eigenvalues of matrix \mathbf{H}_{eff} . Then, we show that a transmission zero is present when the real resonance frequency is equal to the incident frequency. Finally, we consider the effects of the dissipation in acoustic absorbing material. The liner can be described by an impedance model ($Y = 1/Z$):

$$Z = Re + j \cot(Kd_l), \quad (3.23)$$

where d_l is the normalized depth of the liner, and Re is the resistance. Z is assumed to be uniform. All the numerical results are computed with the truncation numbers $M = 30$, $N_x = 30$, and $N_y = 30$. Although Eqs. (3.17) and (3.20) are valid for multi-mode propagation in the waveguide, for the sake of simplicity, we assume that only the plane wave is propagative in regions I and III in the following. It is noted that there is multimode propagating in region II.

We first consider the mode behaviours in the lined closed cavity as defined in Appendix II. It can be described by the eigenvalues (denoted $\beta_{\mu,\nu}^2$) of matrix \mathbf{H}_{lcc} . Matrix \mathbf{H}_{lcc} depends on parameters a and KY when $Re = 0$, so do $\beta_{\mu,\nu}$. The trajectories of $\Re(\beta_{\mu,\nu})$ as a function of $|KY|$ are shown in Fig. 3.2 with $a = 4$ and $Re = 0$. Due to the fact that there is no dissipation in the liner ($Re = 0$), $\beta_{\mu,\nu}$ are either purely real (plot in Fig. 3.2) or purely imaginary. When the eigenvalue curves cross, the modes are degenerate [28]. At the degeneracies, the eigenvalues coalesce, while the eigenfunctions are still bi-orthogonal [28] and there is no interaction between the modes.

We then consider the mode behaviours when the region II is opened. It can be

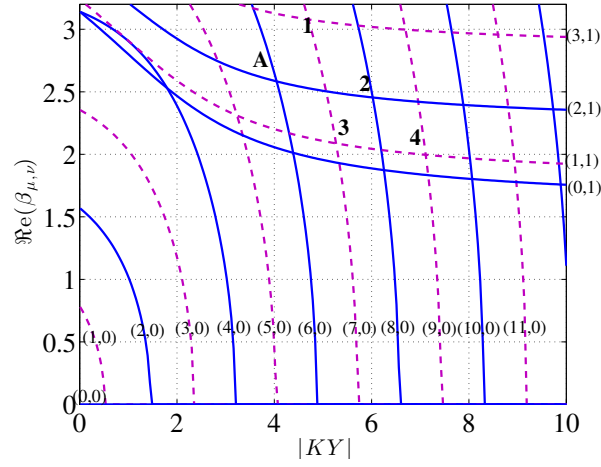


Figure 3.2: Trajectories of the real parts of eigenvalues $\beta_{\mu,\nu}$ of the lined closed cavity as a function of $|KY|$ with $Re = 0$ and $a = 4$. Solid lines label even modes in x -direction, dashed lines label odd modes in x -direction. The mode indices (μ, ν) are marked near each curve.

modelled by the matrix \mathbf{H}_{eff} which depends on parameters: a , KY , and K when $Re = 0$. In Fig. 3.3, we plot the eigenvalue trajectories as a function of $|KY|$ with $a = 4$, $K = 2.5$, and $Re = 0$. The curves with the same symmetry about x , which have crossings in Fig. 3.2, now have either crossings for the real and avoided crossings for the imaginary parts, e.g., A, 3, and 4 in Fig.3.3, or avoided crossings for the real and crossings for the imaginary parts, e.g., 1 and 2 in Fig.3.3. Due to the energy leakage in the rigid duct, the K_λ are now complex. The crossings and avoided crossings of the eigenvalues K_λ in Fig. 3.3, e.g., A, 1, 2, 3, and 4, occur in the vicinity of the degeneracies of the lined closed cavity, as labelled by A, 1, 2, 3, and 4, respectively in Fig. 3.2. Avoided crossings, already known in structural dynamics [35, 36, 37], are less used in cavities lined with impedance.

The above crossing and avoided crossing behaviours may be changed when we change the liner length a . Taking the two modes in the vicinity of “A” in Figs. 3.2 and 3.3 as an example, we decrease the liner length a , the results are shown in Fig. 3.4. When $a = 3.8$, there is a crossing for $\Re(K_\lambda)$ and an avoided crossing for $\Im(K_\lambda)$ (see Fig. 3.4 (a) and (b)), while for $a = 3.6$, there is an avoided crossing for $\Re(K_\lambda)$ and a crossing for $\Im(K_\lambda)$ (see Fig. 3.4 (d) and (e)). The trajectories of K_λ in the complex plane are also shown in Fig. 4 (c) and (f) with $a = 3.8$ and 3.6, respectively, where avoided crossings are always observed.

These findings and the type change of the avoided crossings from Fig. 3.4(c) to Fig. 3.4(f) show that there exists a critical value a_{cri}/h , for which the two curves of K_λ in the complex plane as a function of $|KY|$ will cross at a critical value $|KY|_{\text{cri}}$. These

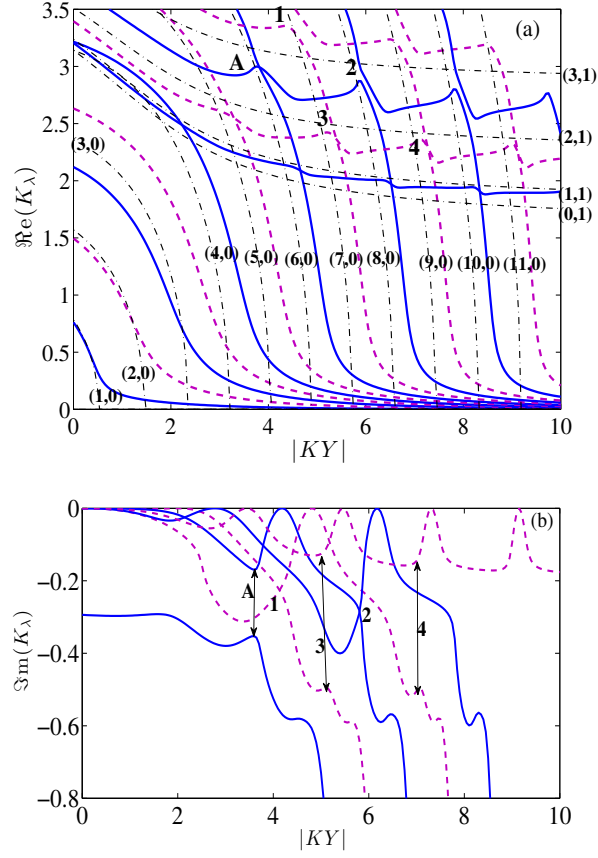


Figure 3.3: Trajectories of $\Re(K_\lambda)$ and $\Im(K_\lambda)$ of matrix \mathbf{H}_{eff} as a function of $|KY|$ with $K = 2.5$, $a = 4$, and $Re = 0$: (a) real parts and (b) imaginary parts. Solid lines and dashed lines correspond to different symmetries as shown in Fig. 3.2. For comparison, we plot also the trajectories of $\Re(\beta_{\mu,\nu})$ of the closed cavity by dash-dot lines.

critical values for the two eigenvalues in Fig. 3.4 are $|KY|_{\text{cri}} = 4.18$ and $a_{\text{cri}} = 3.7$ when $K = 2.5$. $(|KY|_{\text{cri}}, a_{\text{cri}})$ is called an Exceptional Point (EP) in the parameter plane $(|KY|, a)$ when K is fixed. In this case not only the eigenvalues but also the eigenfunctions of the two modes coalesce. A strong mixing of the eigenfunctions of the two modes occurs near the EP. The two modes which participate in the avoided crossing exchange their identities [35, 36].

Avoided crossing occurs in the vicinity of an EP. EPs were first introduced by Kato [38], and were extensively developed by Heiss [25, 26, 27], Rotter [39, 40, 41], and Berry [42]. The mathematically topological structures of Riemann sheets at an EP, depend on a complex parameter or on two real parameters. A typical EP distribution of \mathbf{H}_{eff} in the plane of $|KY|$ and a , with K fixed, is shown in Fig. 3.5. They occur

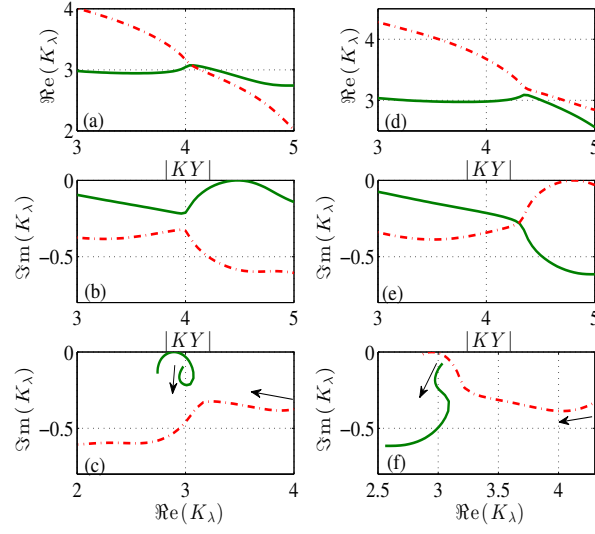


Figure 3.4: Crossings and avoided crossings of K_λ as a function $|KY|$ with $K = 2.5$ under different values of a : (a), (b) and (c) for $a = 3.8$; (d), (e) and (f) for $a = 3.6$. They are the two modes in the vicinity of “A” in Figs. 3.2 and 3.3. EP occurs at $|KY| = 4.18$ and $a = 3.7$, labelled by “ C_1 ” in Fig. 3.5. At (b) $|KY| = 4.5$ and (e) $|KY| = 4.8$, $\Im m(K_\lambda)$ goes to zero, K_λ turns to be a real resonance frequency.

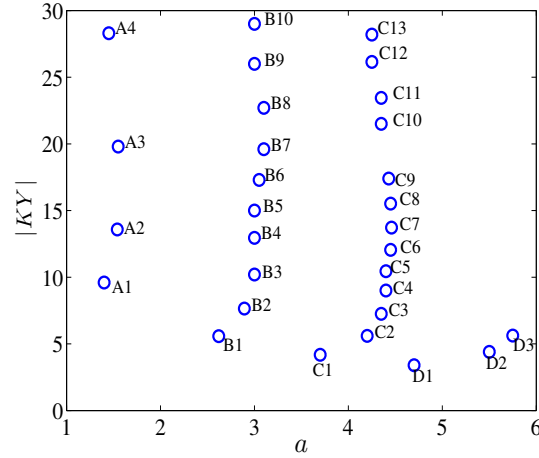


Figure 3.5: The distribution of EPs of H_{eff} in the $(a, |KY|)$ plane with $K = 2.5$. The branches A_i ($i = 1, 2, 3, \dots$) and C_i (B_i and D_i) correspond to the crossings between two modes in lined closed cavity with even (odd) symmetry about x . C_1 corresponds to EP ($|KY|_{\text{cri}} = 4.18, a_{\text{cri}} = 3.7$) when $K = 2.5$. It also corresponds to “A” in Figs. 3.2 and 3.3.

near the crossings between two modes in the lined closed cavity that have the same symmetry about x . The branches A and C (B and D) correspond to the crossings between two modes in the lined closed cavity with even (odd) symmetry about x . The EP at $(|KY|_{cri} = 4.18, a_{cri} = 3.7)$ with $K = 2.5$ corresponds to the C1 in Fig. 3.5.

It is remarkable that at $|KY| = 4.5$ in Fig. 3.4 (b) and $|KY| = 4.8$ in Fig. 3.4 (e), $\Im m(K_\lambda)$ goes to zero. They are real eigenvalues of \mathbf{H}_{eff} in the scattering region II. It is the same kind of mode that Friedrich *et al* [23] found in nuclear reaction, and Sadreev *et al.* [24] found in quantum billiards. The corresponding trapped modes play a crucial role in the transmission zeros in the lined waveguide.

To realize a practical design of transmission zero, we need to understand the mode behaviours in the parameters space (a, d_l, K) . We re-produce Fig. 3.4 in Fig. 3.6 using d_l as a varying parameter. It is quite surprising that the eigenvalue trajectories in the two different parameter spaces of Figs. 3.4 and 3.6 are very similar to each other. We find that at $(a = 3.8, d_l = 0.425)$ and $(a = 3.6, d_l = 0.436)$, real eigenvalues (trapped modes) occur, with $K = 2.5$.

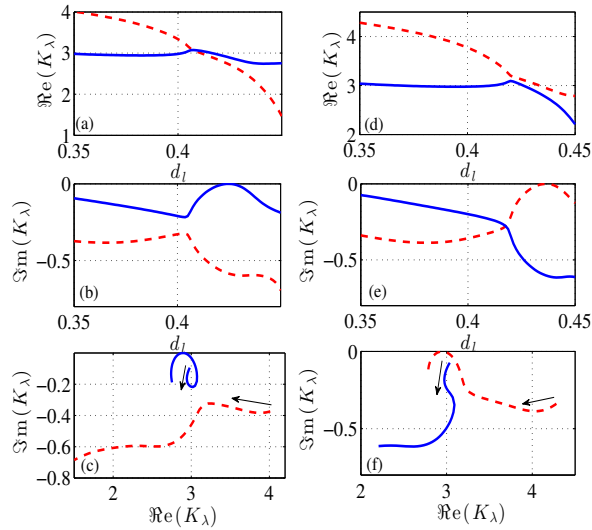


Figure 3.6: Re-plot Fig. 3.4 using d_l , the liner depth, as x-coordinate.

Having the above information, we can obtain the real resonance frequencies of the open system defined in Fig. 3.1 and by Eqs. (3.1)–(3.3) with the radiation conditions $p(x, y) \propto e^{\pm jK_m^x x}$ at $x \rightarrow \pm\infty$ by computing the real poles of the scattering matrix given in Eq.(3.17). The real resonance frequency we seek for corresponds to the point where the curves $y = K_\lambda(K, d_l, a = 3.8)$ cross the line $y = K$. We take the EP “C1” in Fig. 5 as an example. We find that at $d_l = 0.35$ and $a = 3.8$ with $K = 2.85$, a real resonance (trapped mode) occurs. This can be verified by Fig. 3.7, in which we plot

the motions of the eigenvalues K_λ as a function of d_l with $K = 2.85$, $a = 3.8$, and $Re = 0$. It is clear to show that at $d_l = 0.35$ the mode labelled by solid line in Fig. 3.7(b) has $\Im m(K_\lambda) = 0$. Using this group of parameters ($a = 3.8, d_l = 0.35, Re = 0$), we compute the transmission and reflection coefficients of the plane mode by Eq. (3.16), and we plot it in Fig. 3.8(a). A transmission zero occurs near $K = 2.853$, where the reflection coefficient has a corresponding resonance peak. It needs to stress that in the vicinity of this resonance peak, a reflection zero is also present. They clearly show the Fano resonance structure. The corresponding sound pressure field at the frequency of the transmission zero is shown in Fig. 3.8(b).

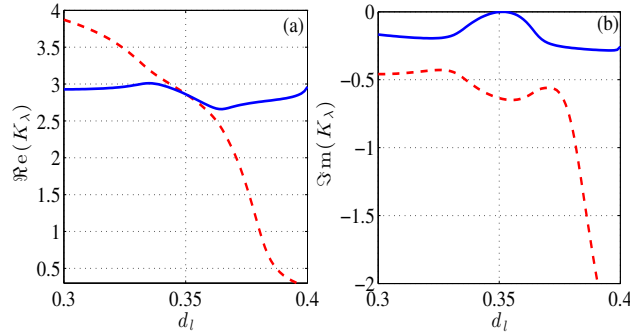


Figure 3.7: Trajectories of eigenvalues K_λ of matrix \mathbf{H}_{eff} as a function of d_l with $K = 2.85, a = 3.8$, and $Re = 0$: (a) real parts and (b) imaginary parts.

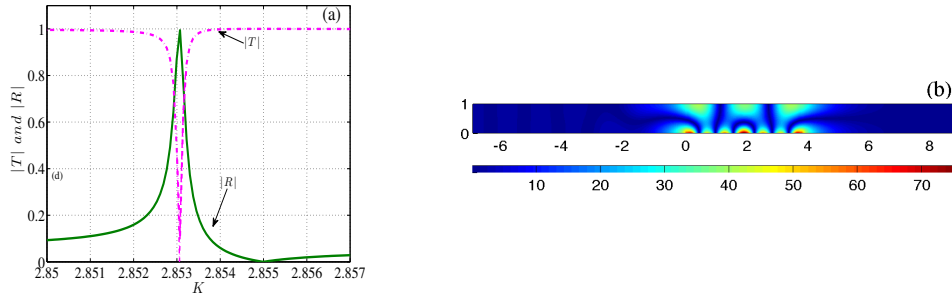


Figure 3.8: (a) Transmission and reflection coefficients as a function of K with $d_l = 0.35, a = 3.8$, and $Re = 0$. (b) The absolute value of sound pressure field in the waveguide when real resonance frequency is crossed, i.e., $|T| = 0$.

Now we consider the effects of dissipation. A small resistance Re is added in the impedance model Eq. (3.23). In Fig. 3.9, we plot the reflection and transmission coefficients as a function of K with $d_l = 0.35$ and $a = 3.8$ under different values of Re . The peaks of the reflection and transmission coefficients decrease rapidly with increasing Re .

The high sensitivity on the dissipation is due to the fact that the crucial ingredient to form Fano resonance in the transmission and reflection coefficients – the trapped mode

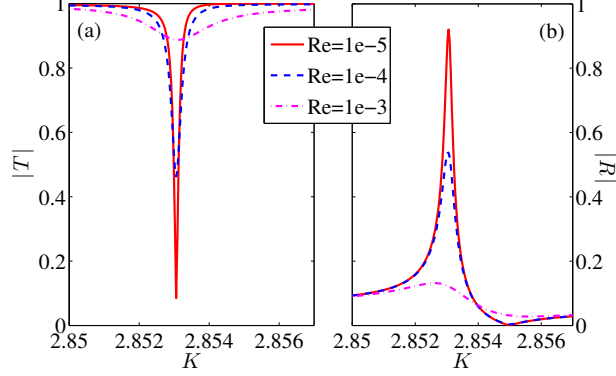


Figure 3.9: (a) Transmission and (b) reflection coefficients of the plane mode as a function of frequency under different values of resistance Re with $d_l = 0.35$.

with real resonance frequency, turns to be quasi-trapped mode with complex resonance frequency. The sharp asymmetric profile becomes smoother, as shown in Fig. 3.9.

3.4 Conclusions

We have shown that the acoustic scattering matrix in a waveguide with a portion of its wall lined by a locally reacting material can be efficiently described with the help of an effective matrix \mathbf{H}_{eff} , whose eigenvalues give the poles of the scattering matrix. The real poles are in the vicinity of the exceptional points of matrix \mathbf{H}_{eff} . Using this effective matrix, the original acoustic resonances problem of the lined portion in the infinite waveguide is reduced to an equivalent eigenvalue problem of matrix \mathbf{H}_{eff} , which describes the eigenvalue problem defined in the finite lined portion (scattering region).

There are an infinite number of exceptional points of \mathbf{H}_{eff} in the parameter plane $(|KY|, a)$ with K fixed, at which the eigenvalues and eigenfunctions of two modes coalesce. In the vicinity of each exceptional point, crossing or avoided crossing of the real and imaginary parts of the complex resonances (eigenvalues) occur. By varying one of the parameters, say $|KY|$, one mode turns to be a trapped mode, its resonance frequency becomes real. When a plane mode is incident, a transmission zero is present when the real resonance frequency is equal to the incident frequency. This transmission zero occurs as a Fano resonance, due to the excitation of a trapped mode in the open system.

EPs, real resonance frequencies, and transmission zeros can also be obtained for parameters (a, d_l, K) , which can suit the practical need of noise mitigation. We have

also shown that the transmission zeros and reflection peaks are highly sensitive to the dissipation.

With the aid of the eigenvalues and eigenfunctions of matrix \mathbf{H}_{eff} , the traditional acoustic resonance scattering formula is extended to include the coupling effects between the open lined portion and the rigid parts of the waveguide.

In this paper, the numerical calculations only show the situation where plane mode is propagating in the rigid ducts, and thus "zero transmission" means that the total sound field is stopped. However, the model is valid for multimode propagation in the waveguides. The possibility of stopping the total sound field when several modes propagate is still an open question.

Appendix I: Derivation of Eq. (3.7) and (3.17)

1. Derivation of Eq. (3.7)

Multiplying Eq. (3.1) by $\boldsymbol{\psi}$, integrating over the closed cavity, we obtain

$$\int_0^1 \int_0^a \boldsymbol{\psi} \left(\frac{\partial^2 p}{\partial x^2} + \frac{\partial^2 p}{\partial y^2} \right) dx dy = -K^2 \int_0^1 \int_0^a \boldsymbol{\psi} p dx dy. \quad (3.24)$$

Applying Green's theorem for Eq. (3.24), substituting Eq. (3.5) into the resulting equation, we have

$$\begin{aligned} & \int_0^1 \left[\boldsymbol{\psi} \frac{\partial p}{\partial x} - \frac{\partial \boldsymbol{\psi}}{\partial x} p \right]_{x=0}^{x=a} dy + \int_0^a \left[\boldsymbol{\psi} \frac{\partial p}{\partial y} - \frac{\partial \boldsymbol{\psi}}{\partial y} p \right]_{y=0}^{y=1} dx \\ & = -(K^2 \mathbf{l} - \Gamma) \int_0^1 \int_0^a \boldsymbol{\psi} p dx dy, \end{aligned} \quad (3.25)$$

where $[F]_{x=0}^{x=a} = F(a) - F(0)$ works for any function F , \mathbf{l} is an identity matrix, and Γ is a diagonal matrix with elements $\gamma_{\mu\nu}^2$. Substituting the boundary conditions, Eqs. (3.3) and (3.6), into Eq. (3.25), results in

$$\int_0^1 \left[\boldsymbol{\psi} \frac{\partial p}{\partial x} \right]_{x=a}^{x=0} dy - jKY \int_0^a \boldsymbol{\psi}(x, 0) p(x, 0) dx = (K^2 \mathbf{l} - \Gamma) \int_0^1 \int_0^a \boldsymbol{\psi} p dx dy. \quad (3.26)$$

Replacing the pressure function p inside the scattering region by Eq. (3.4), and using the orthogonality property of eigenfunctions $\psi_{\mu\nu}$, the expansion coefficients \mathbf{a} can be written as

$$\mathbf{a} = \left(K^2 \mathbf{l} - \Gamma + jKY \int_0^a \boldsymbol{\psi}(x, 0) \boldsymbol{\psi}^T(x, 0) dx \right)^{-1} \int_0^1 \left[\boldsymbol{\psi} \frac{\partial p}{\partial x} \right]_{x=a}^{x=0} dy. \quad (3.27)$$

Substitute the upper expression of \mathbf{a} into Eq. (3.4), we end up with Eq. (3.7).

2. Derivation of Eq. (3.17)

Due to the symmetry property of the matrix S , Eq. (3.16) can be rewritten as

$$S = -I_{2M} + \frac{2jC_{0a}^T(K^2I - H_{lcc})^{-1}C_{0a}K_{2M}^x}{I_{2M} + jC_{0a}^T(K^2I - H_{lcc})^{-1}C_{0a}K_{2M}^x}. \quad (3.28)$$

Now we expand the denominator in Eq. (3.28) into a geometric series [34],

$$\begin{aligned} S &= -I_{2M} + 2jC_{0a}^T \frac{1}{K^2I - H_{lcc}} C_{0a}K_{2M}^x \sum_{q=0}^{\infty} \left(-jC_{0a}^T \frac{1}{K^2I - H_{lcc}} C_{0a}K_{2M}^x \right)^q \\ &= -I_{2M} + 2jC_{0a}^T \frac{1}{K^2I - H_{lcc}} \sum_{q=0}^{\infty} \left(-jC_{0a}K_{2M}^x C_{0a}^T \frac{1}{K^2I - H_{lcc}} \right)^q C_{0a}K_{2M}^x \\ &= -I_{2M} + 2jC_{0a}^T \frac{1}{K^2I - H_{lcc}} \frac{1}{1 + jC_{0a}K_{2M}^x C_{0a}^T \frac{1}{K^2I - H_{lcc}}} C_{0a}K_{2M}^x \\ &= -I_{2M} + 2jC_{0a}^T \frac{1}{K^2I - H_{lcc} + jC_{0a}K_{2M}^x C_{0a}^T} C_{0a}K_{2M}^x. \end{aligned} \quad (3.29)$$

By the expression of K_N , the upper equation results in the Eq. (3.17).

Appendix II

The eigen-problem of the closed cavity with the admittance on the bottom wall, called *lined closed cavity* can be expressed by

$$\nabla^2 \varphi_{\mu\nu} = -\beta_{\mu\nu}^2 \varphi_{\mu\nu}, \quad (3.30)$$

$$\frac{\partial \varphi_{\mu\nu}}{\partial x} \Big|_{x=0,a} = 0, \quad \frac{\partial \varphi_{\mu\nu}}{\partial y} \Big|_{y=0} = jKY \varphi_{\mu\nu}, \quad \text{and} \quad \frac{\partial \varphi_{\mu\nu}}{\partial y} \Big|_{y=1} = 0. \quad (3.31)$$

Bibliography

- [1] A. H. Leskov, J. E. Kaiser, and D. P. Telionis, “Acoustics of Aircraft Engine-Duct Systems”, *AIAA J.* **13**, 130-153 (1975).
- [2] H. H. Hubbard (ed.), *Aeroacoustics of Flight Vehicles: Theory and Practice, Vol. 2, Noise Control* (NASA Reference Publication 1258) (1991), pp. 165–205.
- [3] B. Beck, N. Schiller, and M. Jones, “Impedance assessment of an acoustic metamaterial-inspired acoustic liner”, *J. Acoust. Soc. Am.* **134**, 4222–4222 (2013).
- [4] J.-P. Groby, W. Huang, A. Lardeau, and Y. Aurégan, “The use of slow waves to design simple sound absorbing materials”, *J. Appl. Phys.* **117**, 124903 (2015).
- [5] D. L. Lansing and W. E. Zorumski, “Effects of wall admittance changes on duct transmission and radiation of sound”, *J. Sound Vib.* **27**, 85–100 (1973).
- [6] J. F. Unruh, “Finite length tuning for low frequency lining design”, *J. Sound Vib.* **45**, 5–14 (1976).
- [7] W. Koch, “Attenuation of sound in multi-element acoustically lined rectangular ducts in the absence of mean flow”, *J. Sound Vib.* **52**, 459–496 (1977).
- [8] C. R. Fuller, “Propagation and radiation of sound from flanged circular ducts with circumferentially varying wall admittances, I: Semi-infinite ducts”, *J. Sound Vib.* **93**, 321–340 (1984).
- [9] W. R. Watson, M. G. Jones, T. L. Parrott, and J. Sobieski, “Assessment of Equation Solvers and Optimization Techniques for Nonaxisymmetric Liners”, *AIAA Journal* **42**, 2010–2018 (2004).
- [10] B. Regan and J. Eaton, “Modeling the influence of acoustic liner non-uniformities on duct modes”, *J. Sound Vib.* **219**, 859–879 (1999).
- [11] W. Bi, V. Pagneux, D. Lafarge, and Y. Aurégan, “Modelling of sound propagation in a non-uniform lined duct using a multi-modal propagation method”, *J. Sound Vib.* **289**, 1091–1111 (2006).

-
- [12] W. Bi, V. Pagneux, D. Lafarge, and Y. Aurégan, “An improved multimodal method for sound propagation in nonuniform lined ducts”, *J. Acoust. Soc. Am.* **122**, 280–290 (2007).
- [13] L. M. B. C. Campos, and J. M. G. S. Oliveira, “On the acoustic modes in a cylindrical duct with an arbitrary wall impedance distribution”, *J. Acoust. Soc. Am.* **116**, 3336–3347 (2004).
- [14] B. Luk’yanchuk, N. I. Zheludev, S. A. Maier, N. J. Halas, P. Nordlander, H. Giessen, and C. T. Chong, “The fano resonance in plasmonic nanostructures and metamaterials”, *Nature Mater.* **9**, 707–715 (2010).
- [15] A. E. Miroschnichenko, S. Flach, and Y. S. Kivshar, “Fano resonances in nanoscale structures”, *Rev. Mod. Phys.* **82**, 2257–2298 (2010).
- [16] U. Fano, “Effects of configuration interaction on intensities and phase shifts”, *Phys. Rev.* **124**, 1866–1878 (1961).
- [17] Y. S. Joe, A. M. Satanin, and C. S. Kim, “Classical analogy of Fano resonances”, *Phys. Scr.* **74**, 259–266 (2006).
- [18] S. Hein, W. Koch, and L. Nannen, “Trapped modes and fano resonances in two-dimensional acoustical duct-cavity systems”, *J. Fluid Mech.* **692**, 257–287 (2012).
- [19] R. Parker, “Resonance effects in wake shedding from parallel plates: Some experimental observations”, *J. Sound Vib.* **4**, 62–72 (1966).
- [20] Y. Duan, W. Koch, C. M. Linton, and M. McIVER, “Complex resonances and trapped modes in ducted domains”, *J. Fluid Mech.* **571**, 119–147 (2007).
- [21] V. Pagneux, “Trapped modes and edge resonances in acoustics and elasticity”, *CISM International Centre for Mechanical Sciences* **547**, 181–223 (2013).
- [22] von Neumann and E. P. Wigner, “Uber merkwurdige diskrete eigenwerte”, *Phys. Z* **30**, 465–467 (1929).
- [23] H. Friedrich and D. Wintgen, “Interfering resonances and bound states in the continuum”, *Phys. Rev. A* **32**, 3231–3242 (1985).
- [24] A. Sadreev, E. Bulgakov, and I. Rotter, “Bound states in the continuum in open quantum billiards with a variable shape”, *Phys. Rev. B* **73**, 235342 (2006).
- [25] W. D. Heiss and A. L. Sannino, “Avoided level crossing and exceptional points”, *J. Phys. A: Math. Gen.* **23**, 1167–1178 (1990).
- [26] W. D. Heiss, “Repulsion of resonance states and exceptional points”, *Phys. Rev. E* **61**, 929–932 (2000).

-
- [27] W. D. Heiss, “Exceptional points of non-hermitian operators”, *J. Phys. A: Math. Gen.* **37**, 2455–2464 (2004).
- [28] P. M. Morse and K. U. Ingard, *Theoretical acoustics* (McGraw-Hill Book Company, New York) (1968), Chap. 5, pp. 206.
- [29] S. Hein, W. Koch, and L. Nannen, “Fano resonances in acoustics”, *J. Fluid Mech.* **664**, 238–264 (2010).
- [30] L. Flax, G. Gaunaurd, and H. Überall, *Theory of Resonance scattering, in Physical Acoustics: Principles and Methods, Vol. XV, Eds., W. P. Mason and R. N. Thurston* (Academic Press) (1999), Chap. 3, pp. 191–294.
- [31] L. Flax, L. R. Dragonette, and H. Überall, “Theory of elastic resonance excitation by sound scattering”, *J. Acoust. Soc. Am.* **63**, 723 (1978).
- [32] P. Racec, E. Racec, and H. Neidhardt, “Evanescent channels and scattering in cylindrical nanowire heterostructures”, *Phys. Rev. B* **79**, 155305 (2009).
- [33] E. R. Racec, U. Wulf, and P. N. Racec, “Fano regime of transport through open quantum dots”, *Phys. Rev. B* **82**, 085313 (2010).
- [34] H.-J. Stöckmann, E. Persson, Y.-H. Kim, M. Barth, U. Kuhl, and I. Rotter, “Effective hamiltonian for a microwave billiard with attached waveguide”, *Phys. Rev. E* **65**, 066211 (2002).
- [35] A. W. Leissa, “On a curve veering aberration”, *J. Applied Math. and Phys. (ZAMP)* **25**, 99–111 (1974).
- [36] J. R. Kuttler and V. G. Sigillito, “On curve veering”, *J. Sound and Vib.* **75**, 585–588 (1981).
- [37] N. C. Perkins and C. D. Mote, “Comments on curve veering in eigenvalue problems”, *J. Sound and Vib.* **106**, 451–463 (1986).
- [38] T. Kato, *Perturbation Theory of Linear Operators* (Berlin: Springer) (1966), pp. 64.
- [39] I. Rotter, “A non-hermitian hamilton operator and the physics of open quantum systems”, *J. Phys. A: Math.Theor.* **42**, 153001 (2009).
- [40] U. Gunther, I. Rotter, and B. Samsonov, “Projective hilbert space structures at exceptional points”, *J. Phys. A: Math. Theor.* **40**, 8815–8833 (2007).
- [41] M. Muller and I. Rotter, “Exceptional points in open quantum systems”, *J. Phys. A: Math. Theor.* **41**, 244018 (2008).
- [42] M. V. Berry, “Physics of nonhermitian degeneracies”, *Czechoslovak J. of Phys.* **54**, 1039–1047 (2004).

Chapter 4

Use of metaporous materials in acoustic ducts

The second strategy is presented and validated in this chapter. A set of periodic rigid inclusions are embedded in a porous lining to enhance the sound attenuation in an acoustic duct at low frequencies. Floquet-Bloch theorem is introduced to investigate the sound attenuation in a 2D infinite waveguide lined with periodic inclusions embedded in porous material. Crossing is observed between the mode attenuations of two Bloch waves. Here the mode coupling is due to the presence of the inclusions embedded in the porous material. The most important and interesting figure is that near the frequency where the crossing of the mode attenuations appears, an attenuation peak is observed. This phenomenon can be used to explain the transmission loss peak observed numerically and experimentally in a 3D waveguide with a finite portion of its wall lined by a porous material embedded with periodic inclusions.

4.1 Introduction

The acoustic treatment we discussed in the previous chapter is generally made with a perforated sheet backed by honeycomb [1]. This kind of material has good absorption properties only in a narrow frequency band but their main advantages are their mechanical robustness and their capability to resist to harsh conditions i.e. they constitute the reference solution in a turbofan engine. For some other applications porous material are often used to reduce the noise emission, e.g., in the ventilation systems and the Auxiliary Power Units (APU) of aircrafts. They generally offer a wider absorption/attenuation band. However, they suffer from a lack of absorption efficiency at low frequencies, comparing to their efficiency at higher frequencies. To solve that problem, other approaches must be investigated and new concepts of acoustic absorbers dedicated to the reduction

of turbo-machinery noise at low frequencies must be developed.

To improve the liner capability at the low frequency range, in the applications of acoustic gratings and panels, the usual way is by multi-layering [2, 3, 4]. Another alternative solution, material including periodic subwavelength resonators, is studied in analogy to optical metamaterials [5, 6, 7]. In this view, metaporous materials, made of periodic rigid inclusions embedded in the porous medium, have been proposed to enhance the absorption properties at frequencies lower than the quarter wavelength frequency [8, 9, 10]. The principle is that the energy is trapped and dissipated between periodic rigid inclusions embedded in the porous medium and the rigid backing or in the inclusions themselves. A nearly total absorption can be obtained for a frequency lower than the quarter-wavelength resonance frequency due to the excitation of trapped modes. Local resonance and trapped modes are another possibility to localize the field. Using the trapped mode to produce additional transmission zero is also discussed in the previous two chapters.

In this chapter, the influence of the mode coupling due to the periodic embedment of rigid inclusions in porous material is studied for the waveguide applications instead of acoustic gratings [8, 9] numerically and experimentally. The use of periodic inclusion in the waveguide has also been studied by Nennig *et al.* [11], in which a finite element (FE) method, inspired from Ref. [12], was chosen to tackle a quadratic eigenvalue problem. The Floquet-Bloch theorem is used to reduce the computation on one periodic cell. It has been shown that open shape inclusions (e.g. U-shape) are able to enhance the attenuation when compared with a homogeneous liner. Thanks to Floquet-Bloch formalism assuming periodic heterogeneities [8, 9, 11, 13], very interesting results have been obtained in acoustics. The Floquet theorem is applicable to ordinary differential equations with periodic coefficients and shows that the solutions are such that

$$\psi(x + L_0) = e^{jk_B L_0} \psi(x),$$

where L_0 is the period of the coefficients, k_B is the Bloch wave number, and x is the propagation axis. Such functions are known as Bloch wave functions.

In this work, the Floquet-Bloch theorem is applied to analyse the sound attenuation in a 2D infinite periodic waveguide lined by a porous material embedded with rigid inclusions. The mode attenuation can be explicitly described by the imaginary part of the wave number k_B . The wave numbers and the wave functions of the Bloch waves in the given waveguide can be defined by the solutions of a generalized eigenvalue problem [14, 15]. The propagating mode of a periodic waveguide are given by the Bloch waves with unitary eigenvalues.

The present work is organised as follows. In Chap.4.2, the problem of a 3D waveguide partially lined with a porous material embedded with periodic inclusions is first described. The experimental and numerical methods to consider the transmission be-

haviours are also introduced. Floquet-Bloch theorem is proposed to investigate the sound attenuation in a similar 2D infinite waveguide lined with periodic inclusions embedded in porous material(Chap.4.3). In Chap.4.4, the experimental and numerical results for the 3D waveguide with different inclusion shapes and configurations are presented and discussed.

4.2 Description of the problem

4.2.1 Experimental setup

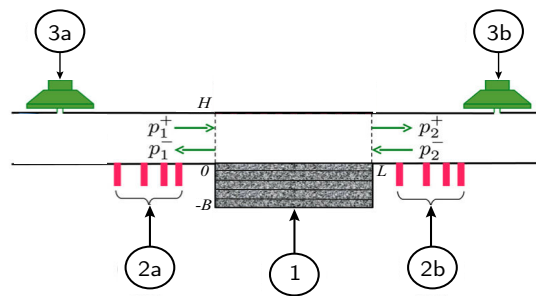


Figure 4.1: Schematic view of the experimental setup. 1: material, 2a: four upstream microphones, 2b: four downstream microphones, 2c: array of 11 microphones, 3a: upstream source, 3b: downstream source. It need to be noted that the test material is put in a big rigid cavity.

The test facility used in this study is schematically depicted in Fig. 4.1 [16]. A two sources method is used: the acoustic waves are produced by two loudspeakers 3a and 3b and propagate in a rectangular duct (width $W=100\text{mm}$ ×height $H=15\text{mm}$). Two anechoic terminations are used to avoid resonant conditions in the duct.

The acquisition of signals is performed by Agilent VXI 1432 hardware platform which drives the source excitation synchronously with the acoustic pressure signals recording. A swept-sine over the frequency range 30–3500 Hz is used with a frequency increment of 10 Hz. The test materials are put in position 1.

Two series of four microphones mounted in the upstream (2a) and downstream (2b) of the test material section are used to measure the acoustical pressure. Those microphones are located at the positions: $x_{u1} - x_{u2} = x_{d1} - x_{d2} = 63.5\text{mm}$, $x_{u1} - x_{u3} = x_{d1} - x_{d3} = 211.5\text{mm}$ and $x_{u1} - x_{u4} = x_{d1} - x_{d4} = 700\text{mm}$. The use of 2×4 microphones allows an over-determination of the transmitted and reflected waves on both sides of the test material and avoids the problems in the precision of measurement when the acoustic wavelength is close to half the distance between two microphones.

In the frequency range 30–3400Hz, only 2 acoustic modes can propagate in the rigid ducts: the plane wave and the first-order mode along dimension W . The microphones being located just at the centre of dimension W , this second mode is not measured and the microphones only capture the plane waves.

4.2.2 Measuring technique

The aim of the experimental apparatus is to measure the transfer matrix or the scattering matrix of a test material [17]. The scattering matrix for the plane wave relates the scattered pressure amplitudes p_2^+ and p_1^- (see Fig. 4.1) to the incident pressure amplitudes p_1^+ and p_2^- by

$$\begin{pmatrix} p_1^- \\ p_2^+ \end{pmatrix} = \begin{bmatrix} R^+ & T^- \\ T^+ & R^- \end{bmatrix} \begin{pmatrix} p_1^+ \\ p_2^- \end{pmatrix} = \mathcal{S} \begin{pmatrix} p_1^+ \\ p_2^- \end{pmatrix}, \quad (4.1)$$

where T^+ and T^- are the anechoic transmission coefficients, R^+ and R^- are the anechoic reflection coefficients, and superscripts \pm indicate the direction of wave propagation along the x axis, and the subscripts ‘1, 2’ indicate the upstream and downstream of the duct. The method of measurement used in the present study is called “the 2 sources method”. Two measurements are made in two different states of the system. These different states are obtained by switching on the upstream source, the downstream source being switched off (measurement I), and vice versa (measurement II).

The scattering matrix is calculated from the two measurements using the following relation:

$$\begin{bmatrix} (p_1^-/p_1^+)^{\text{I}} & (p_1^-/p_2^-)^{\text{II}} \\ (p_2^+/p_1^+)^{\text{I}} & (p_2^+/p_2^-)^{\text{II}} \end{bmatrix} = \mathcal{S} \begin{bmatrix} 1 & (p_1^+/p_2^-)^{\text{II}} \\ (p_2^-/p_1^+)^{\text{I}} & 1 \end{bmatrix}, \quad (4.2)$$

This calculation is meaningful only if the two measurements are independent, i.e., if the determinant of the second right side matrix does not vanish: $(p_2^-/p_1^+)^{\text{I}} \neq (p_1^+/p_2^-)^{\text{II}}$.

For the measurement I, the sound pressure in the waveguide is written (time dependence $e^{-j\omega t}$ is omitted):

$$p(x_1) = p_1^+ e^{jk^+ x_1} + p_1^- e^{-jk^- x_1} = p_1^+ \left(e^{jk^+ x_1} + R_1^+ e^{-jk^- x_1} \right), \quad (4.3)$$

where R_1^+ is the reflection coefficient from measurement I, and k^+ and k^- are the wavenumbers in the duct in the direction of $+x$ and in the reverse direction. Then the expressions of the pressure at microphones u_i and u_j are obtained by

$$p(u_i) = p_1^+ e^{jk^+ x_{u_i}} + p_1^- e^{jk^- x_{u_i}} = p_1^+ \left(e^{jk^+ x_{u_i}} + R_1^+ e^{-jk^- x_{u_i}} \right),$$

and

$$p(u_j) = p_1^+ e^{jk^+ x_{u_j}} + p_1^- e^{jk^- x_{u_j}} = p_1^+ \left(e^{jk^+ x_{u_j}} + R_1^+ e^{-jk^- x_{u_j}} \right),$$

respectively, where x_{u_i} is the position of the microphone u_i relatively to the inlet of the measured element, the same for microphone u_j .

The upper two equations result in

$$\frac{p(u_j)^I}{p(u_i)^I} = \frac{e^{jk^+x_{u_j}} + R_1^+ e^{-jk^-x_{u_j}}}{e^{jk^+x_{u_i}} + R_1^+ e^{-jk^-x_{u_i}}}. \quad (4.4)$$

A transfer function is defined to label the ratio of the pressure between microphones u_j and u_i ,

$$H_{u_j u_i}^I = \frac{p(u_j)^I}{p(u_i)^I}. \quad (4.5)$$

By Eq. (4.4), the reflection coefficient from measurement I can be found from the transfer function between two different microphones by a relation of the type

$$(p_1^-/p_1^+)^I = \frac{H_{u_j u_i}^I e^{jk^+x_{u_i}} - e^{jk^+x_{u_j}}}{e^{-jk^-x_{u_j}} - H_{u_j u_i}^I e^{-jk^-x_{u_i}}}. \quad (4.6)$$

All the other matrix elements can be found by the same way (see [18] for details). Thus, the wavenumbers k^+ and k^- have to be known to calculate the scattering matrix.

For measurement II, we have

$$p(d_i) = p_2^+ e^{jk^+x_{d_i}} + p_2^- e^{-jk^-x_{d_i}} = p_2^- \left(R_1^- e^{jk^+x_{d_i}} + e^{-jk^-x_{d_i}} \right),$$

and

$$p(d_j) = p_2^+ e^{jk^+x_{d_j}} + p_2^- e^{-jk^-x_{d_j}} = p_2^- \left(R_1^- e^{jk^+x_{d_j}} + e^{-jk^-x_{d_j}} \right).$$

The same as we did before, the upper two equations result in

$$(p_2^+/p_2^-)^{II} = \frac{H_{d_j d_i}^{II} e^{-jk^-x_{d_i}} + e^{-jk^-x_{d_j}}}{e^{jk^+x_{d_j}} - H_{d_j d_i}^{II} e^{jk^+x_{d_i}}}.$$

For the transmission coefficients $T_1^+ = \frac{p_2^+}{p_1^+}$ and $T_1^- = \frac{p_1^-}{p_2^-}$, the pressures at microphone u_i and d_i are applied,

$$\frac{p(d_i)}{p(u_i)} = \frac{p_2^+ \left(e^{jk^+x_{d_i}} + \frac{1}{R_1^-} e^{-jk^-x_{d_i}} \right)}{p_1^+ \left(e^{jk^+x_{u_i}} + R_1^+ e^{-jk^-x_{u_i}} \right)},$$

we define

$$H_{d_i u_i}^{21} = \frac{p(d_i)}{p(u_i)}, \quad H_{u_i d_i}^{12} = \frac{p(u_i)}{p(d_i)},$$

the upper equations can lead to

$$(p_2^+/p_1^+)^I = H_{d_i u_i}^{21} \frac{e^{jk^+ x_{u_i}} + R_1^+ e^{-jk^- x_{u_i}}}{e^{jk^+ x_{d_i}} + \frac{1}{R_1^-} e^{-jk^- x_{d_i}}},$$

$$(p_1^-/p_2^-)^{II} = H_{u_i d_i}^{12} \frac{R_1^- e^{jk^+ x_{d_i}} + e^{-jk^- x_{d_i}}}{\frac{1}{R_1^+} e^{jk^+ x_{u_i}} + e^{-jk^- x_{u_i}}}.$$

4.2.3 Description of the configurations

The porous material is a metallic foam that has been chosen to avoid any skeleton vibrations. It is supplied as plates (200mm×100mm) of thickness 5mm. Five layers of this porous material are assembled together to form the uniform porous material, it is labeled by “5P”. The parameters of the metallic foam used in the fluid equivalent model have been measured on another setup. The values are porosity $\Phi = 0.99$, tortuosity $\alpha_\infty = 1.17$, viscous length $\Lambda = 1 \times 10^{-4}$ m, thermal length $\Lambda' = 2.4 \times 10^{-4}$ m, and resistivity $\sigma = 6.9 \times 10^3 \text{ kg m}^{-3} \text{ s}^{-1}$.

In order to embed the inclusions in the porous material, holes are drilled in three of the porous material layers. Two types of inclusion shape are investigated: the first type is a metallic hollow cylinder with one closed end and one open end (labeled by “R1” in the following), the second (labeled “R2”) is a closed hollow cylinder with a slit on the side (Helmholtz resonator), see Fig. 4.2(a). The inclusions are filled with air. The external diameter of R1 is $D=22\text{mm}$, and the inner diameter is $d=21\text{mm}$. Three

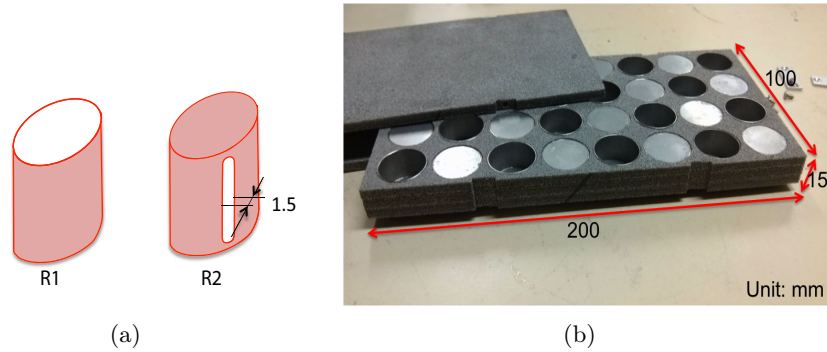


Figure 4.2: (a) Two different inclusion shapes: open cylinder(R1) and Helmholtz resonator(R2). (b) Picture of the measured sample.

different orientations of R1 in the three layers are considered. If the closed ends of all the cylinders are on the bottom and direct towards the rigid backing, it's called “R1_B”; inversely, “R1_T” for all the closed ends are on the top direct towards the duct (see Fig.4.3). Otherwise, if the cylinders are put in an alternated way, it's labeled by “R1_A”,

as shown in Fig. 4.2(b). With the addition of the other two layers of porous materials, different labels are used depending on the positions of the porous materials, the details can be found in Fig. 4.3. In Fig. 4.4, we give the distributions of the inclusions in the porous material.

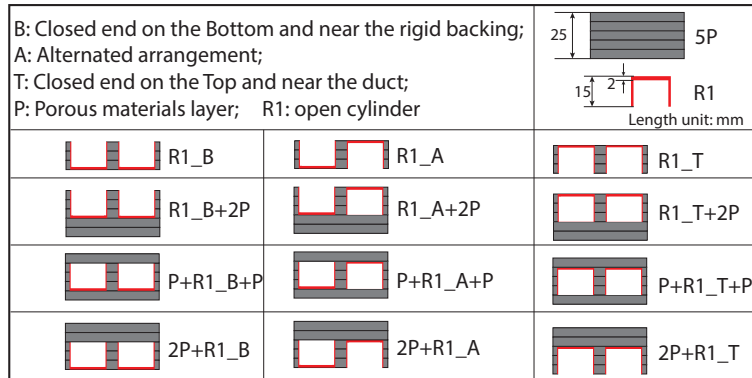


Figure 4.3: Vertical plane views and the definitions of the different configurations we considered. The inclusions R1 are embedded in 3 layers of porous material with three different arrangements (labeled by “R1_B”, “R1_A”, and “R1_T”, respectively). One or two layers of porous materials are also assembled in different ways to consider the effects. A picture of P+R1_A+P is shown in Fig. 4.2(b).

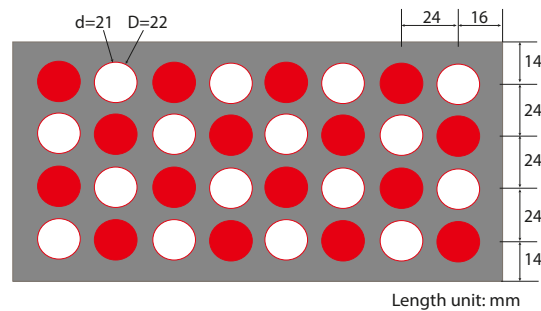


Figure 4.4: Distributions of the inclusions in the porous material. A horizontal plane of the porous material with inclusions.

For the second type of inclusion R2, as shown in Fig. 4.2(a), three orientations of the open slit are considered, see Fig. 4.5(a). When the open slits all orient towards the upstream of the duct, the configuration is labelled by R2_0°. By rotating the open slits of R2_0° counterclockwise 90°, the orientations of open slits are perpendicular to the propagation direction in the duct, which is now R2_90°. R2_A is used to consider the interaction of the slits between two neighbored inclusions, by putting the open slits 0° and 180° alternately. Those inclusions are embedded into three layers of porous

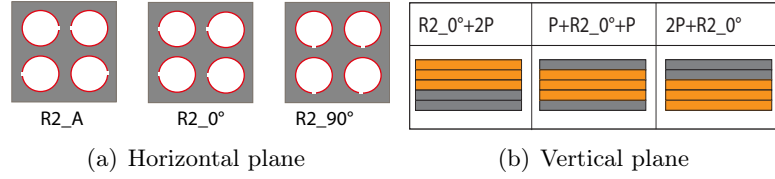


Figure 4.5: (a) Three different orientations of R2 in the porous materials (horizontal view). (b) The other two layers of porous material are assembled in three different ways.

material. As we did before for the R1, the other two layers of porous material can also be assembled in three different ways, e.g., as shown in Fig. 4.5(b).

4.2.4 Numerical method

Computations have been performed at Airbus using ACTIPOLE software developed by Airbus Group Innovations [19]. ACTIPOLE is designed to solve harmonic acoustic wave propagation problems by the Boundary Element Method. The parallel and out-of-core direct solver has been used in order to predict the transmission loss (TL) and the pressure field in the whole computational domain for each computed frequency, taking into account porous liners by assuming a fluid equivalent behavior. The higher the value of the TL, the better the attenuation of the porous medium.

To study the influence of the two different inclusions and the porous material on the transmission loss, five different configurations are considered, as defined in Table 4.1. For “Air+R1_A+Air” and “Air+R2_A+Air”, the inclusions are embedded in big rigid cavity filled with air.

Table 4.1: Definition of the configurations studied with Actipole

CONF	Inclusion	Porous material	Objective
P+R1_A+P	R1	×	Effect of R1
P+R2_A+P	R2	×	Effect of R2
Air+R1_A+Air	R1		The sole effect of R1 (without porous)
Air+R2_A+Air	R2		The sole effect of R2 (without porous)
5P	No inclusions	×	Reference with only porous material

4.3 2D simple model analysis

4.3.1 Problem statement

We consider here the acoustic wave propagation in a 2D infinite periodic waveguide lined with a porous material with embedded rigid inclusions, as described in Fig. 4.6.

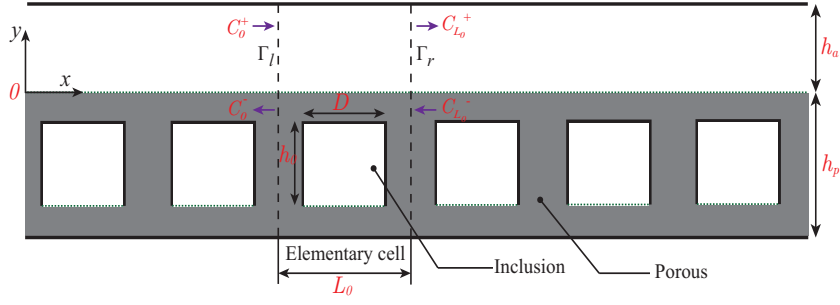


Figure 4.6: Periodic \sqcap -shape inclusions embedded in a porous material, with $h_a = 15\text{mm}$ and $h_p = 25\text{mm}$ in the following. $L_0 = 24\text{mm}$ is the length of the unit cell. $D = 22\text{mm}$ and $h_i = 15$ are the width and height of the rigid inclusion.

For the simplification, the shape of the inclusion is \sqcap -shape. In the air domain, i.e. $y \in [0, h_a]$, the sound pressure $p_a(x, y)$ satisfies the governing equation in the 2D Cartesian coordinates (x, y)

$$\left(\frac{\partial^2}{\partial x^2} + \frac{\partial^2}{\partial y^2} + \left(\frac{\omega}{c_a} \right)^2 \right) p_a(x, y) = 0, \quad (4.7)$$

where ω is the circular frequency, and c_a denotes the sound speed in the air. Time dependence is assumed as $\exp(-j\omega t)$ and will be omitted in the following. The acoustic velocity is obtained by

$$\rho_a \frac{\partial u_a}{\partial t} = -\nabla p_a,$$

where ρ_a is the air density.

In the porous material, i.e. $y \in [-h_p, 0]$, the skeleton of the porous material is considered as infinitely rigid, thus the Champoux-Allard-Johnson equivalent fluid model [20] is used to get the effective compressibility κ_{eq} and effective density ρ_{eq} (see Appendix 4.A for details). The phase velocity is given by $c_{eq} = \sqrt{\kappa_{eq}(\omega)/\rho_{eq}(\omega)}$. The sound pressure $p_p(x, y)$ in the porous material satisfies the wave equation

$$\left(\frac{\partial^2}{\partial x^2} + \frac{\partial^2}{\partial y^2} + \left(\frac{\omega}{c_{eq}(\omega)} \right)^2 \right) p_p(x, y) = 0. \quad (4.8)$$

The acoustic velocity in the porous can also be obtained by

$$\rho_{eq} \frac{\partial u_p}{\partial t} = -\nabla p_p.$$

On the rigid walls, the pressure satisfies the rigid boundary condition. At the surface $y = 0$ between the air and the porous material, the continuity of pressure and normal

velocity leads to

$$p_p(x, 0^-) = p_a(x, 0^+), \quad \frac{1}{\rho_{eq}} \frac{\partial p_p}{\partial y} \Big|_{y=0^-} = \frac{1}{\rho_a} \frac{\partial p_a}{\partial y} \Big|_{y=0^+}. \quad (4.9)$$

For an infinite duct lined with porous material, the eigenvalues can be solved by Finite Difference Method (FDM) (see Appendix 4.B for details). The eigenvalue problem is rewritten as

$$(\mathbf{D}_2 + k^2 \mathbf{I}) \mathbf{P} = k_x^2 \mathbf{P}, \quad (4.10)$$

where \mathbf{D}_2 is the 2nd order differential matrix, k contains the elements ω/c_a and ω/c_{eq} (see Appendix 4.B for details), \mathbf{I} is an identity matrix, and k_x is the wavenumber in x -direction.

By computing the eigenvalues of Eq.(4.10), the wavenumber k_x can be obtained, with $\Im(k_x) > 0$ for $+x$ -direction and $\Im(k_x) < 0$ for $-x$ -direction. With the help of the resulting wavenumbers k_x and eigenvectors \mathbf{P} , the pressure in $\pm x$ - direction can be expressed by

$$\mathbf{p}^\pm(x) = \sum_{n=1}^{n=N} C_n^\pm \mathbf{P}_n \exp(\pm j k_{x,n} x) = \mathbf{X} \mathbf{E}(\pm x) \mathbf{C}^\pm, \quad (4.11)$$

where n is the mode index, \mathbf{X} is a matrix in which the columns are the the eigenvectors \mathbf{P}_n , $\mathbf{E}(\pm x)$ are diagonal matrices with $\exp(\pm j k_{x,n} x)$ on the main diagonal, and \mathbf{C} is a vector with mode amplitudes C_n .

4.3.2 Bloch waves and eigenvalue problems

When the governing equations, the boundary conditions and the geometry are L_0 -periodic along x (see Fig. 4.6), it follows from the Floquet-Bloch theorem that the solution are Bloch waves [21]

$$p(x, y) = \hat{p}(x, y) e^{j k_B x}, \quad (4.12)$$

i.e. the pressure function $p(x, y)$ can be split into a L_0 -periodic function $\hat{p}(x, y)$ modulated by a plane wave with the Floquet-Bloch wavenumber k_B . It needs to be noted that the Bloch wavenumber is common for both media as the axial wavenumber for classical guided wave problems. The concept of mode can be extended to periodic system thanks to the Floquet-Bloch theorem.

On the right and left boundaries of the elementary cell, respectively on Γ_r and Γ_l , the pressure function satisfies the condition

$$\mathbf{p}(x + L_0, y) = \hat{\mathbf{p}}(x, y) e^{j k_B L_0}. \quad (4.13)$$

It follows from Eq. (4.13) that the real part of $k_B L_0$ measures the change in phase across the cell and its imaginary part the attenuation. In addition, it can be directly shown

from Eq. (4.12) that k_B is defined modulo $2\pi/L_0$. The smallest values belongs to the irreducible Brillouin zone.

Taking an arbitrary cell (see Fig. 4.6), the scattering matrix (denoted as \mathbf{S}) concept

$$\begin{pmatrix} C_0^- \\ C_{L_0}^+ \end{pmatrix} = \underbrace{\begin{bmatrix} R & t \\ T & r \end{bmatrix}}_{\mathbf{S}} \begin{pmatrix} C_0^+ \\ C_{L_0}^- \end{pmatrix} \quad (4.14)$$

remains valid, where $\mathbf{R}(\mathbf{r})$ and $\mathbf{T}(\mathbf{t})$ are the matrices containing reflection and transmission coefficients, C_0^\pm and $C_{L_0}^\pm$ are the amplitudes of $\pm x$ -direction waves for the pressures at $x = 0$ and L_0 , respectively. Due to the symmetry of the geometry, we have $R = r$, and due to the reciprocity $T = t$. The scattering matrix \mathbf{S} for an elementary cell can be obtained by using mode matching of the pressure and velocity at the discontinuity interfaces, the details are given in Appendix 4.C.

Moreover, the pressure functions obey the Bloch condition [22]

$$\begin{pmatrix} C_{L_0}^+ \\ C_{L_0}^- \end{pmatrix} = e^{jk_B L_0} \begin{pmatrix} C_0^+ \\ C_0^- \end{pmatrix}. \quad (4.15)$$

The upper two equations, Eqs. (4.14) and (4.15), lead to the following eigenvalue problem

$$\underbrace{\begin{bmatrix} T & r \\ 0 & I \end{bmatrix}}_{\mathbf{M}_1} \begin{pmatrix} C_0^+ \\ C_{L_0}^- \end{pmatrix} = \underbrace{e^{jk_B L_0}}_{\lambda} \underbrace{\begin{bmatrix} I & 0 \\ R & t \end{bmatrix}}_{\mathbf{M}_2} \begin{pmatrix} C_0^+ \\ C_{L_0}^- \end{pmatrix}, \quad (4.16)$$

where I and 0 are the identity and zero matrices. As the reflection and transmission matrices $\mathbf{R}(\mathbf{r})$ and $\mathbf{T}(\mathbf{t})$ are already known (see Appendix 4.C), the dispersion relation giving the solution for the Bloch wavenumbers k_B can be solved numerically [14, 15]. With the help of the eigenvalues λ from the generalized matrix eigenvalue problem, the Bloch wavenumber is obtained by

$$k_B = -j \ln(\lambda)/L_0. \quad (4.17)$$

The propagating Bloch waves are such that $|\lambda| = 1$; the other waves are evanescent and decay exponentially in the direction of propagation. With the help of the resulting eigenvectors $(C_0^+, C_{L_0}^-)^T$ from the eigenvalue problem of Eq. (4.16) and the scattering matrix \mathbf{S} , the amplitudes of the incoming and outgoing modes at the entrance and exit can be given. Using the Eq.(4.26) in Appendix 4.C, the amplitudes of the modes at different segments can be obtained. The wave functions of the Bloch waves then can be expressed by using Eq.(4.11) for each segment.

4.3.3 Effects of inclusions and porous material

The aim of this section is to illustrate the effects of the inclusions and the porous material on the sound attenuation. The properties of a uniform waveguide lined with pure porous material is first investigated. The effects of the porous material on the transmission loss of a plane wave in a rigid duct is also considered. Then the inclusions are embedded in the porous material to enhance the sound attenuation at low frequencies.

When there is no inclusion embedded in the porous material, the eigenvalue problem in an infinite waveguide lined with a pure porous material (called porous lined duct in the following) can be solved by Finite Difference Method, as detailed in Appendix 4.B. The wavefunction is separable and can be expressed by $\mathbf{p}(x, y) = \mathbf{P}e^{jk_x x}$.

For the sake of convenience, Bloch waves introduced in Sec. 4.3.2 are also applied here to find the Bloch wavenumbers in the porous lined duct, with the same period L_0 as in Fig. 4.6 considered. In this particular case, the Bloch wavenumbers k_B and the axial wavenumbers k_x are identical, and $\hat{\mathbf{p}}(x, y)$ in Eq. (4.13) is independent of x , which becomes the transverse eigen-modes.

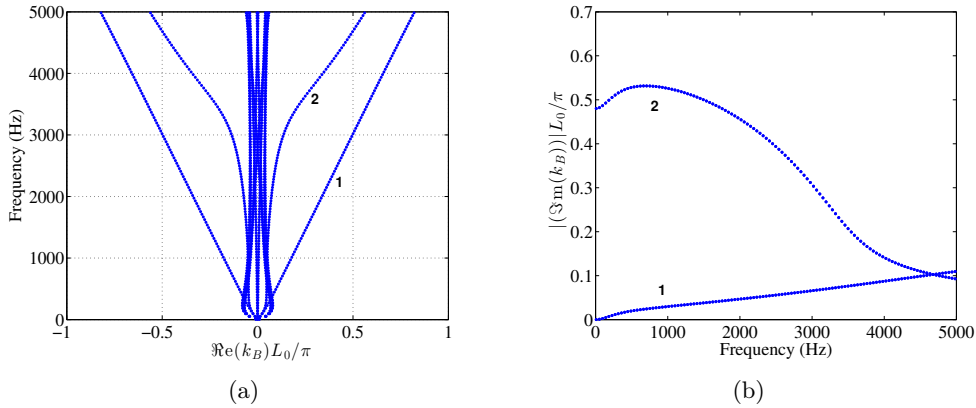


Figure 4.7: (a) Real and (b) imaginary parts of k_B as a function of frequency when there is no inclusions in Fig. 4.6.

In Fig.4.7, for this particular case, we plot the real and imaginary parts of Bloch wavenumbers k_B as a function of frequency. From the imaginary parts of k_B , we can have the sound attenuation of each mode along x as a function of frequency. Here we are only interested in the lower two modes. At low frequencies the distinction between the mode with the least attenuation and all other modes is fairly clear because the latter are, in general, highly attenuated cut-off modes. The fact that there is a mode with minimum attenuation is extremely useful because provided the source distribution does excite all the modes, then at some distance from the source the sound field will consist of just this one mode, and hence the sound attenuation at larger distances will be

entirely determined by this minimum value [23]. From Fig.4.7(b), we can see that around 4700Hz, the imaginary parts of the lower two waves cross. This is where the maximum attenuation of the least attenuated mode happens. For a waveguide lined with locally reacting liner, of special interest is the question of optimizing the sound attenuation by judiciously selecting the impedance characteristics of the liner. In this view, the concept of optimal liner was first defined and investigated by Cremer [24]. It has been shown that Cremer's optimum impedance is a branch point [23] and an Exceptional Point (EP) in complex admittance (impedance) plane (as we discussed in Chap. 1.4.) and EPs play an important role in the sound attenuation [25].

However, if a finite length ($L = 0.2$ m) of such porous material is attached to two semi-infinite rigid ducts, in which the porous liner is truncated by rigid walls at the two ends (see e.g. Fig. 4.1), the transmission loss (TL) peak is observed around 3800Hz. The results are given in Fig. 4.8, with only plane wave incident in the rigid duct. Similar as described in Appendix 4.C, the scattering matrix can be derived by using mode matching at the interfaces $x = 0$ and L . Good agreements can be seen from the comparisons between the computation and experimental results [16]. The oscillations in the reflection coefficient are linked to the wave reflection at the end of the material ($x = L$). The reflection coefficient oscillates around about a value of $|R| = 0.41$ which is close to the value $(1 - \alpha)/(1 + \alpha) = 0.45$, where $\alpha = H/(H + B)$, valid at low frequencies for an area expansion without porous material [16]. To have a comparison and to see the effects from the discontinuity interfaces, the TL (i.e. $e^{jk_B L}$) of the least attenuated mode with length $L = 0.2$ m is also plotted in Fig.4.8(b) by the dashed line. We can see that the frequency of the TL peak is smaller with the two semi-infinite rigid ducts, comparing with the one for the least attenuated mode.

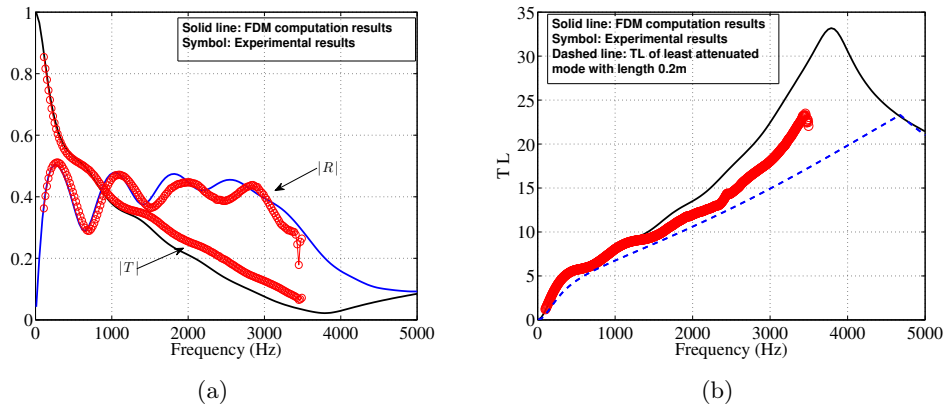


Figure 4.8: (a) Transmission and reflection coefficients and (b) transmission loss (TL) for the plane wave in a rigid duct partially treated with porous material (length $L=0.2$ m) as a function of frequency. The experimental measurements are also performed and compared with the computation results. The TL of the least attenuated mode with length 0.2m is also given by the dashed line.

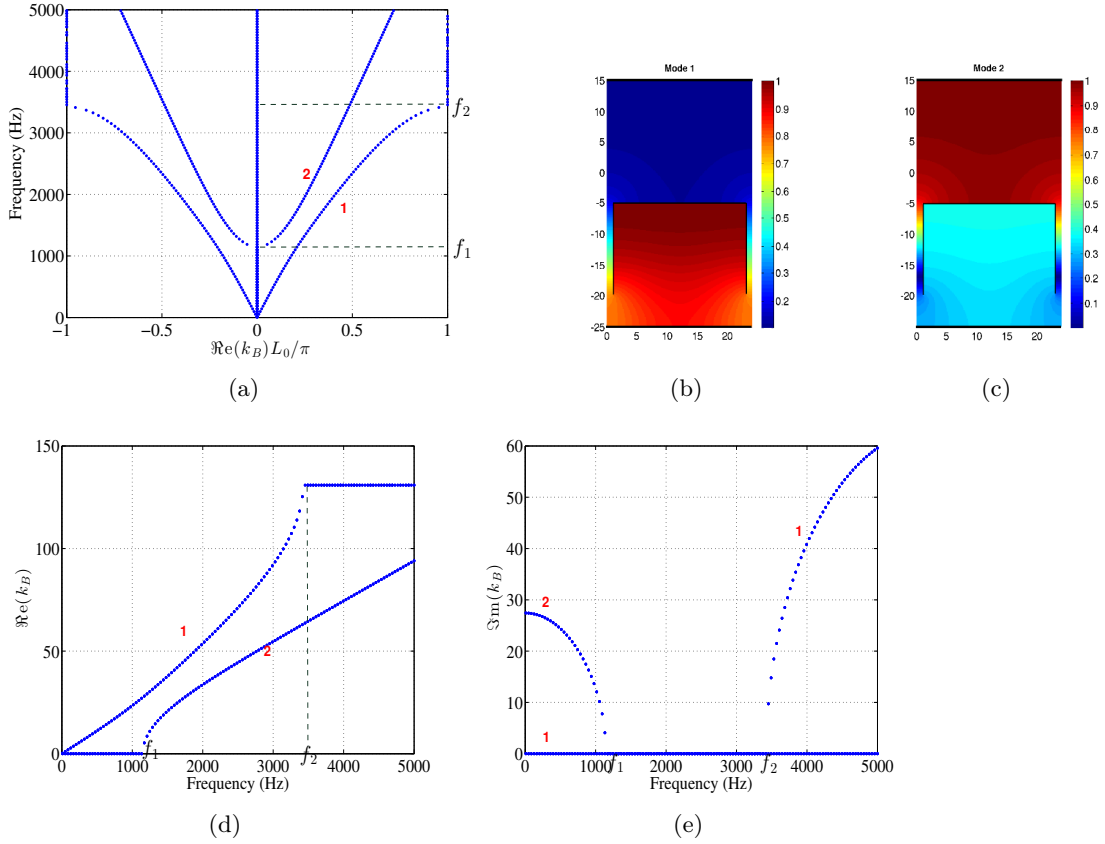


Figure 4.9: (a) Band diagram for the waveguide with inclusions embedded in the air, i.e. when there is no porous material in Fig. 4.6. (b) and (c) Absolute value of periodic function $\hat{p}(x, y)$ for the lower two Bloch waves (corresponding to “1” and “2” in Fig.4.9(a)) at 2000Hz, the unit of the axis is in millimetre. (d) Real and (e) imaginary parts of the lower two k_B (+x-direction) as a function of frequency.

To understand the mode coupling effects, we first analyse results without porous material. In Fig. 4.9(a), the band diagram is given for the waveguide with the \square -shape inclusions embedded in air (no dissipation is included). These scatterers are located at the centre of the periodic cell with the dimensions: width $D = 22\text{mm}$, height $h_0 = 15\text{mm}$ and periodic length $L_0 = 24\text{mm}$. For the sake of simplification, the inclusion thickness is neglected. At some point, the wavenumber k_B becomes complex due to the interference with the reflection at each discontinuity, and the wave function is attenuated along the propagation direction, for example the mode labelled by “1” in Fig. 4.9(a) becomes complex when $f > 3400\text{Hz}$. This can also be illustrated by Fig. 4.9(d)(e), where the real and imaginary parts of the two k_B as a function of frequency are given. There exist a frequency band $[f_1, f_2]$, in which modes 1 and 2 both can propagate. When $f < f_1$, only mode 1 can propagate, mode 2 is evanescent. Then when $f > f_2$, the

wavenumber of mode 1 becomes complex. The absolute value of the periodic functions $\hat{p}(x, y)$ for the lower 2 Bloch waves (labelled by 1 and 2 in Fig. 4.9(a)) at 2000Hz are plotted in Fig. 4.9(b)(c). From the function distribution in the unit cell, we can see that the pressure of mode 2 is mainly localized inside the inclusion with the help of the rigid backing, we will call it “Localized mode” in the following. While for mode 1, the pressure is mainly in the region $-5\text{mm} < y < 15\text{mm}$, which will be called “Acoustic mode”.

To have sound attenuation, the porous material has to be applied. The air filled inclusions are embedded in the porous material (see Fig. 4.6) to improve the sound attenuation at low frequencies. The mode attenuation in dB/m, given by

$$A(k_B) = 8.68 \cdot \Im m k_B, \quad (4.18)$$

can be shown in Fig. 4.12(a) for such configuration. The frequency (880Hz) of the first attenuation peak in a waveguide lined with periodic inclusions embedded in porous material (symbol “●”) is much lower than the one (4700Hz) in a porous lined duct (symbol “▲”). It indicates that due to the embedment of the rigid inclusions in the porous materials, the sound attenuation at 880Hz is enhanced.

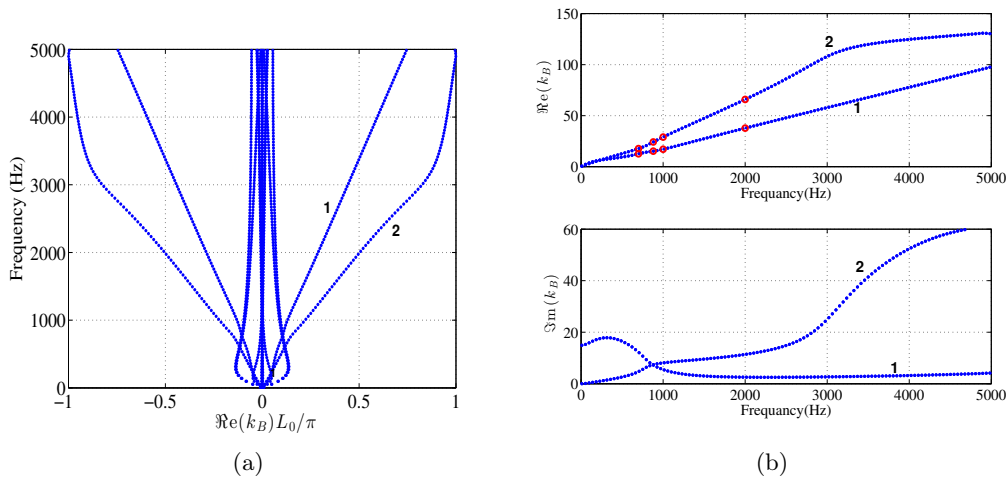


Figure 4.10: (a) Band diagram for the waveguide with inclusions embedded in the porous material. (b) Real (upper) and imaginary (bottom) parts of k_B as a function of frequency for the waveguide shown in Fig. 4.6. The periodic wave functions of the lower two modes at the frequencies 700Hz, 880Hz, 1000Hz, and 2000Hz (“○” in Fig. 4.10(b)(upper)) are plotted in Fig. 4.11.

To explain this behaviour, the band diagram for the waveguide lined with periodic inclusions embedded in porous material (see Fig. 4.6), obtained by plotting the Bloch wavenumbers k_B as function of the frequency, is presented in Fig. 4.10(a). We can see that due to the presence of the porous material, the wavenumbers become complex, and

they are very different with those without porous material(Fig.4.9). The imaginary parts of the lower two k_B as a function of frequency, which give the essential information about the sound attenuation, are also plotted (see the bottom figure in Fig. 4.10(b)). Crossing is observed between mode 1 and mode 2. The maximum attenuation of the least attenuated mode then can be found near 880Hz, where the crossing of the imaginary parts between the lower two modes is observed.

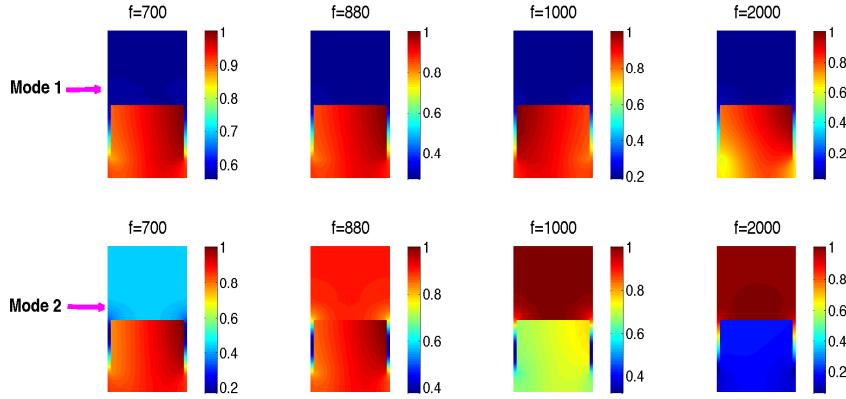


Figure 4.11: Absolute value of periodic function $\hat{p}(x, y)$ for the mode 1 (upper) and mode 2 (bottom) (modes 1 and 2 from Fig.4.10) at frequencies 700Hz, 880Hz, 1000Hz, and 2000Hz, respectively.

To study the behaviours of the Bloch waves near the maximum attenuation, the periodic function $\hat{p}(x, y)$ for the lower two modes (labelled by 1 and 2 in Fig. 4.10) at different frequencies (see the “o” in the upper figure of Fig. 4.10(b)) are computed in Fig. 4.11. First of all, we can see that the results verify $\hat{p}(x, y) = \hat{p}(x + L_0, y)$. Mode 1 is the so-called localized mode which is also observed in Fig. 4.9(b), the pressure field is mainly localized inside the inclusions. However, for the periodic function of mode 2, it is a mixing of the acoustic mode and localized mode at 880Hz, which indicates the existence of the coupling between the two different kinds of mode. The periodic waveguide can interfere in the homogeneous waveguide framework. It is worth noting that the first attenuation peak is strongly connected to this coupling effect and to the crossing observed for the imaginary parts. Indeed, modes avoid each other thanks to a modification of the k_B imaginary part leading to an enhancement of the attenuation.

To see the effect of the porous material embedded with inclusions on the transmission behaviours in a rigid waveguide, the transmission loss in a waveguide partially lined with such material, in which 8 cells are embedded in the centre of a porous material of length $L = 0.2\text{m}$, is computed, shown by the solid line in Fig. 4.12(b). The TL of the least attenuated Bloch waves is also plotted (symbol “•”) for length $L = 0.2\text{m}$. The TL peak observed at 880Hz can be explained by the crossing of the mode attenuation between

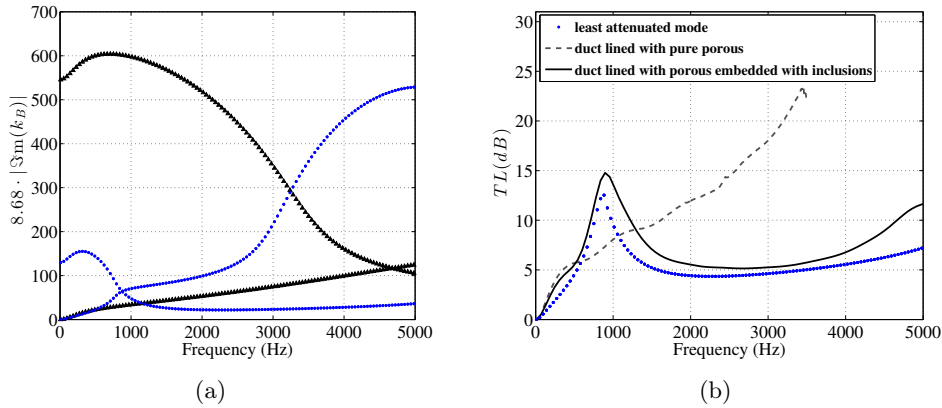


Figure 4.12: (a) Mode attenuations (dB/m) of the lower two Bloch waves in the uniform waveguides lined with periodic inclusions embedded in porous material (symbol “•”) and in the porous lined duct (without inclusions)(symbol “▲”). (b) Symbol “•”: TL of the lease attenuated Bloch mode with length $L = 0.2$ m (i.e. $e^{jK_B L}$). Solid line: TL of the plane mode in an acoustic waveguide with a portion of its wall lined by a porous material embedded with 8 inclusions, the total length of the lined portion is L . Dashed line: Measured TL for a waveguide partially lined with a pure porous material of length L .

the lower two Bloch waves (see “•” in Fig. 4.12(a)), due to the coupling of the two lower Bloch waves. The TL in the waveguide embedded with inclusions (solid line) is enhanced between 500Hz and 1300Hz, comparing to the one without inclusions (dashed line).

As already shown by Groby *et al.* [8] that the inclusion position in the periodic cell can be a sensitive parameter. The effects of the positions of the inclusions in the porous material on the TL with length $L = 0.2$ m of the least attenuated mode are also investigated, by moving the inclusions above (+ mm) or below (- mm) the current centre position. The results are shown in Fig. 4.13. The frequency of the first peak decreases when the inclusions are moved both above and below the centre position. The opposite effect is observed for the second TL peak. These effects are not so evident when the inclusions are moved above the centre poison.

It need to be noted that under different inclusion positions, the Bloch wave numbers k_B can move in a different way with varying the frequency. To illustrate this point, we plot the $\Re(k_B)$ and $\Im(k_B)$ as a function of frequency, see Fig. 4.14, with three different inclusions positions: the inclusions are in the centre 0 mm (Fig. 4.14(a)(b)), below the centre 4 mm (Fig. 4.14(c)(d)) and 4.9 mm (Fig. 4.14(e)(f)). We can see that for the $\Im(k_B)$, the crossing becomes avoided crossing with moving the inclusions below the centre. This might be related to the exceptional point(see Chaps. 2 and 3).

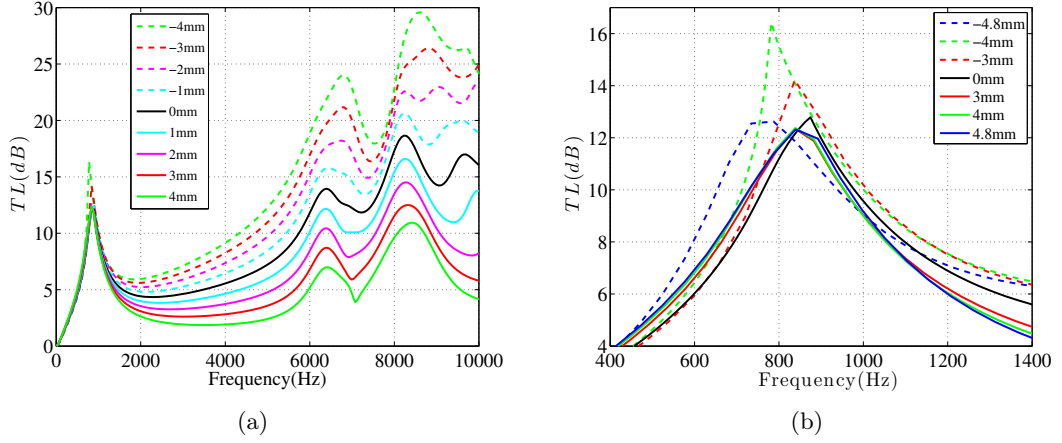


Figure 4.13: (a) The effect of the inclusion position in the porous material on the TL of the least attenuated Bloch wave with length $L = 0.2\text{m}$. “0 mm” indicates that the inclusions are embedded in the centre, as in Fig.4.6. “1mm” or “-1mm” means that the inclusions are moved of 1mm above or below the centre position. (b) A zoom of Fig.4.13(a) for the low frequencies.

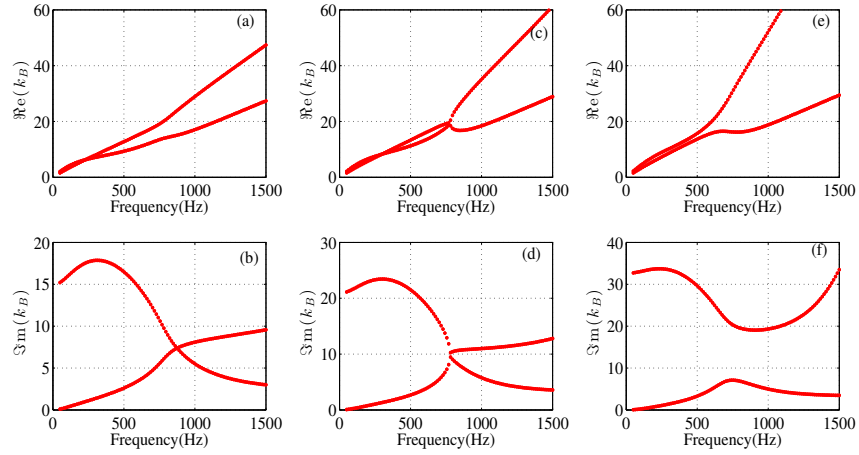


Figure 4.14: Real and imaginary parts of k_B as a function of frequency with different inclusion positions in the porous: the inclusions are (a)(b) in the centre (0 mm), (c)(d) below the centre (-4 mm), and (e)(f) below the centre (-4.9 mm).

4.4 3D numerical and experimental results

Numerical simulations and experimental measurements are carried out for the configurations described in Chap. 4.2.4 and Chap. 4.2.3, respectively. It needs to be noted that the material is put in a big rigid cavity.

4.4.1 Numerical results

Numerical calculations have been performed for various configurations which are reported in Table 4.1 and within the frequency range of the audible sound, particularly, at low frequencies. For all calculations, the top of the big cavity (which is used to put the porous material) as well as any non-rigid/empty surface (e.g. the surface between the open end of the inclusion and the porous material) are made of a resistive layer with very small resistivity: $Re = 1e-4$.

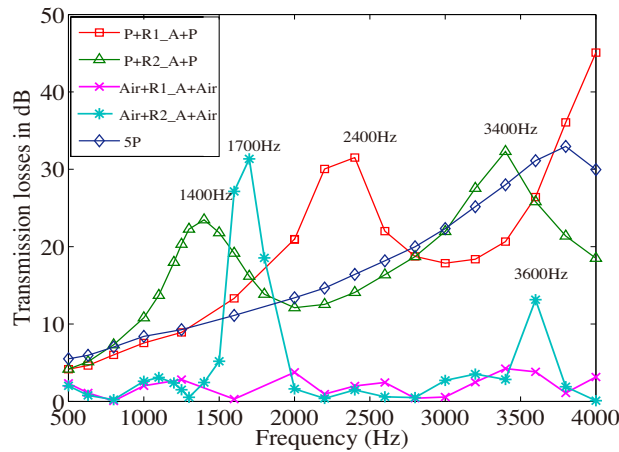


Figure 4.15: Transmission loss (dB) for the 5 configurations when the plane mode is incident.

The transmission loss (TL) for the 5 configurations given in Table 4.1 are shown in Fig. 4.15, when only the plane mode is incident. The numerical frequency range is 500Hz to 4000Hz. At very low frequencies (below 800 Hz), the results of the configurations with porous material are quite similar meaning that the inclusions do not have any effect in this frequency range. However, when the frequency increases, a mid-frequency peak (MFP) is observed in transmission losses for both P+R1_A+P and P+R2_A+P at 2400Hz and 1400Hz, respectively. The MFP of P+R2_A+P happens at a lower frequency than the MFP of P+R1_A+P. A second TL peak appears for P+R2_A+P at 3400Hz. It can be noted that due to the presence of the inclusions, the attenuation is increased around the MFP but there is a small negative effect on TL at frequencies below MFP, and a large negative effect on TL at frequencies above MFP.

Air+R1_A+Air and Air+R2_A+Air are used to consider the effects of the two different inclusions when no porous material is added. At low frequencies, $f < 1.2\text{kHz}$, the two TL curves are quite similar. They are also close to the results of an empty cavity (not shown here). Thus, in this frequency range, the inclusions have no significant effects on the TL. Two TL peaks are found at 1.7 kHz and 3.6 kHz for Air+R2_A+Air.

However, no obvious effects are found by correlating P+R1_A+P with Air+R1_A+Air, and the MFP of P+R1_A+P seems to be due to a more complex interaction of the inclusion R1 with the porous material. The porous material plays a very important role for the TL peak of P+R1_A+P. Comparing P+R2_A+P and Air+R2_A+Air, the TL of P+R2_A+P (porous material + inclusions R2) cumulates the resonant effects of inclusions (Air+R2_A+Air), with a shift of peaks to lower frequencies, and the effects of porous material (5P). Due to the presence of porous material, the TL increases, and the frequencies of the two TL peaks shift to lower frequencies. The objective for inclusions to improve the attenuation of the sole porous material in low frequency range (peak of attenuation can be tuned) seems to be reachable, at the price of a moderate degradation of the attenuation at other frequencies.

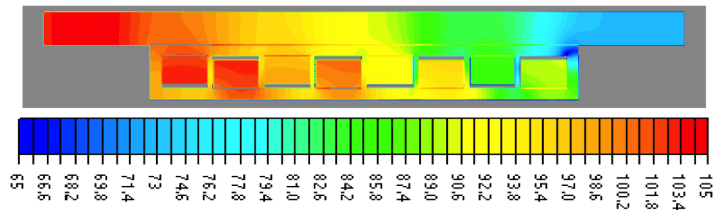


Figure 4.16: Pressure field distribution in the duct for P+R1_A+P at 2400Hz (scale in dB SPL), a plane mode is incident with an intensity of 100 dB.

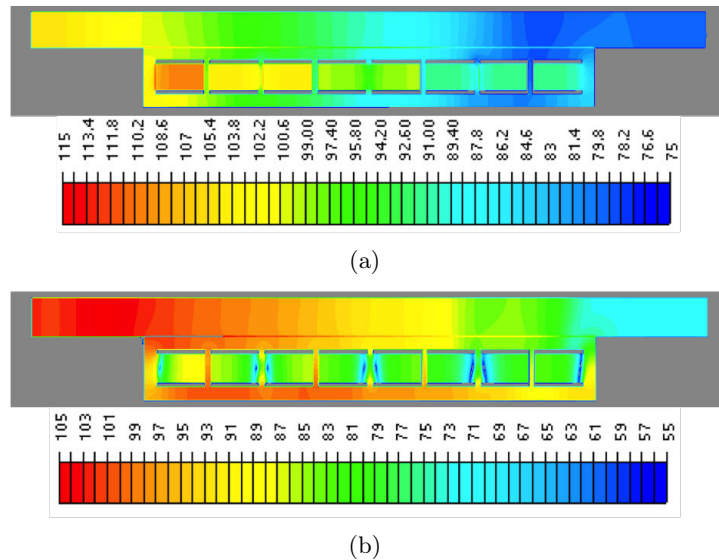


Figure 4.17: Pressure field distribution in the duct for P+R2_A+P at (a)1700Hz and (b)3400Hz (scale in dB SPL), a plane mode is incident with an intensity of 100 dB.

The computed pressure fields for P+R1_A+P and P+R2_A+P at the frequencies

of the TL peaks are given in Fig. 4.16 and Fig. 4.17, respectively. A plane wave is incident from the left side, the pressure decreases in the duct along the material. Large pressure is observed inside some inclusions for P+R1_A+P. Between the rigid bottom of R2 and the rigid backing, the pressure localization is observed at 3400Hz (Fig. 4.17(b)).

4.4.2 Experimental results for the configurations with R1

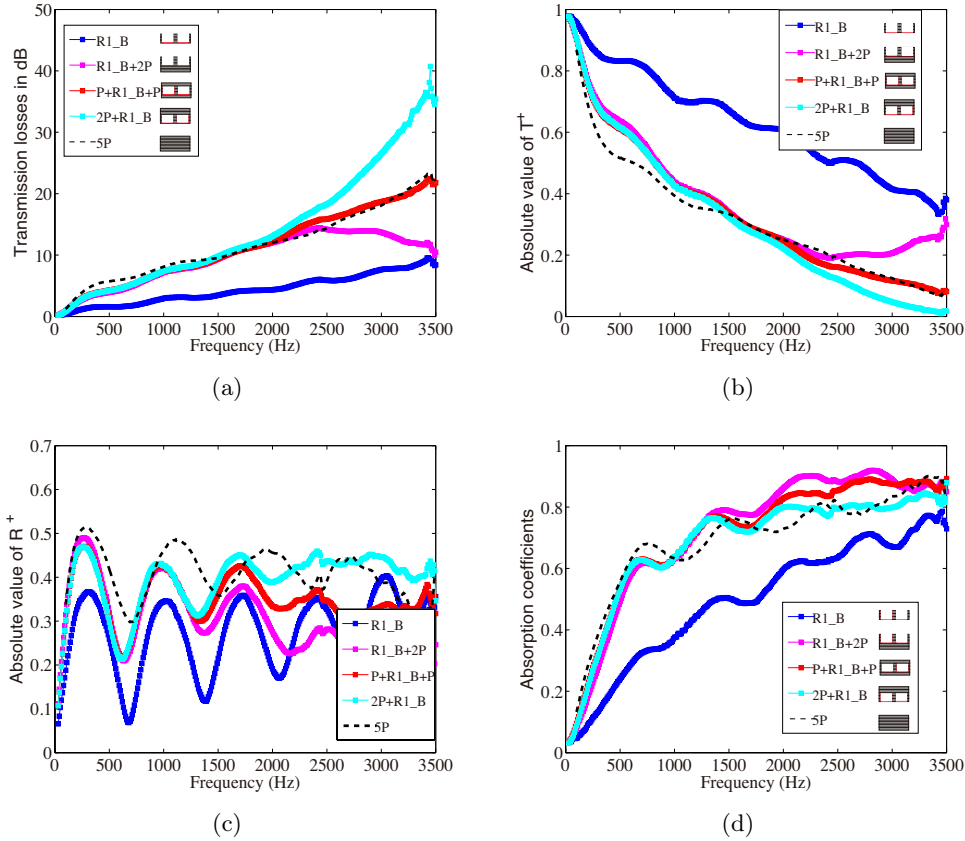


Figure 4.18: (a)Transmission loss, absolute value of (b) T^+ , (c) R^+ and (d) absorption coefficients when the closed send of all the R1 are on the bottom(R1_B) near the rigid backing, and also with the consideration of porous materials layers.

Fig. 4.18 shows the experimental results when the closed ends of all the inclusions R1 are on the bottom (R1_B) near the rigid backing, as illustrated in the inset of Fig. 4.18(a). When there are only three layers of porous material embedded with inclusions (R1_B), due to the reduction of the porous materials, its TL is the smallest at all the frequency range of interest comparing to the other configurations. For $f > 2400\text{Hz}$, more porous material layers are near the waveguide, higher transmission loss (TL) is observed, we have the following relation $\text{TL}(\text{R1_B}+2\text{P}) < \text{TL}(\text{P}+\text{R1_B}+\text{P}) < \text{TL}(\text{2P}+\text{R1_B})$

B). It means that for the configurations with R1_B, the porous material plays the main role on the transmission loss. For $f < 2400\text{Hz}$, the three configurations have similar transmission loss (transmission coefficient). For the reflection coefficient, big difference is observed when $f > 1200\text{Hz}$, see Fig. 4.18(c).

The TL of configuration P+R1_B+P is quite similar to the one of 5P, which means that such configuration has even no enhancement on the sound attenuation. This can also be verified and explained by the presence of the Bloch waves in the periodic waveguide, as we introduced in Sec. 4.3. A maximum attenuation can be observed near the frequency where the mode attenuations of the lower two modes have crossing (or avoided crossing). For this 3D configuration, the Bloch wave computation is carried out by using a finite element discretisation [11]. The 3D periodic waveguide is an infinite duct lined with configuration P+R1_B+P (see the right one in Fig. 4.20(c)), it need to be noted that the bottom of the liner is a rigid wall. The TLs of the lower two modes for this periodic waveguide with length $L = 0.2\text{m}$ as a function of frequency are shown by “□” in Fig. 4.20(a) [26]¹. At the frequency range we considered, there is no crossing between the two TLs. The TL of the least attenuated Bloch wave increases with the frequency slowly, leading to the slow increase of TL with frequency in a rigid duct partially lined with P+R1_B+P.

However, for configuration 2P+R1_B, the transmission loss is improved for $f > 2400\text{Hz}$ comparing with 5P and P+R1_B+P. It might be because the frequency of the crossing between the lower two mode attenuations are lower than the one for configuration P+R1_B+P, due to the different inclusion positions in the porous material. The effect of the inclusion position in the porous material on the sound attenuation has also been investigated in the 2D waveguide, see Fig. 4.13 .

By the following expression,

$$Ab = 1 - \left(|T^+|^2 + |R^+|^2 \right),$$

the absorption coefficients for the different configurations are also considered, as shown in Fig. 4.18(d). Biggest absorption is observed for R1_B+2P for frequencies $1500\text{Hz} < f < 3000\text{Hz}$, it is due to the smallest reflection coefficient, see Fig. 4.18(c), we have the opposite relation for absorption coefficient $Ab(\text{R1_B}+2\text{P}) > Ab(\text{P}+\text{R1_B}+\text{P}) > Ab(2\text{P}+\text{R1_B})$, comparing to the TL.

Figure 4.19 gives the results for the configurations in which the closed ends of all the inclusions are on the top (R1_T) near the air filled duct. It is remarkable that there is transmission loss peaks around $f = 2000\text{Hz}$ for configurations R1_T, R1_T+2P and P+R1_T+P. It means that the periodic waveguide with inclusions (R1_T) interferes in the porous lined duct at low frequencies, and results in the TL peak. From the TLs of the Bloch waves in a periodic waveguide with configuration P+R1_T+P (see the left on

1. Thanks to Benoit Nenning for the 3D Bloch waves computation [26].

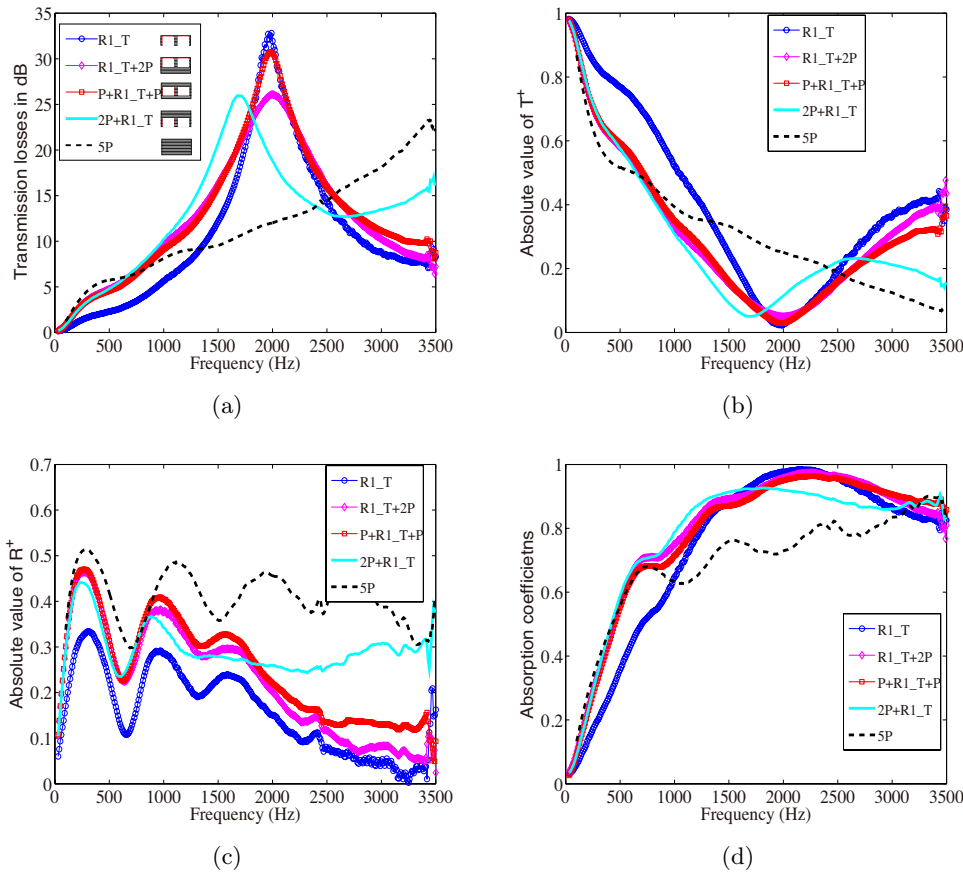


Figure 4.19: (a) Transmission loss, absolute value of (b) T^+ , (c) R^+ and (d) absorption coefficients when the inclusions are all closed on the top and open on the bottom (R1_T), and also with the consideration of different porous materials layers.

in Fig. 4.20(c)), labelled by “□” in Fig. 4.20(b), a crossing of the TLs between the two Bloch waves are observed. The most important is that the TL peak (solid line) of the lined duct appears just near this crossing. This is exactly what we discussed before in Sec.4.3 for a 2D configuration. The TL in a rigid duct partly lined with finite periodic liner is dominated by the mode attenuation of the least attenuated mode in the periodic waveguide. An attenuation peak is reached if there is a crossing for the mode attenuations between this least attenuated and the 2nd mode.

Taking a look at the results for R1_T in Fig. 4.19, the open ends were closed by the big rigid cavity when the measurements were performed. At the frequency range we considered, no resonance effect from the inside of the inclusions appears, which should be at higher frequency. Highest TL peak is observed for R1_T around 2000Hz, comparing with R1_T+2P and P+R1_T+P. It is due to the reduction of porous materials,

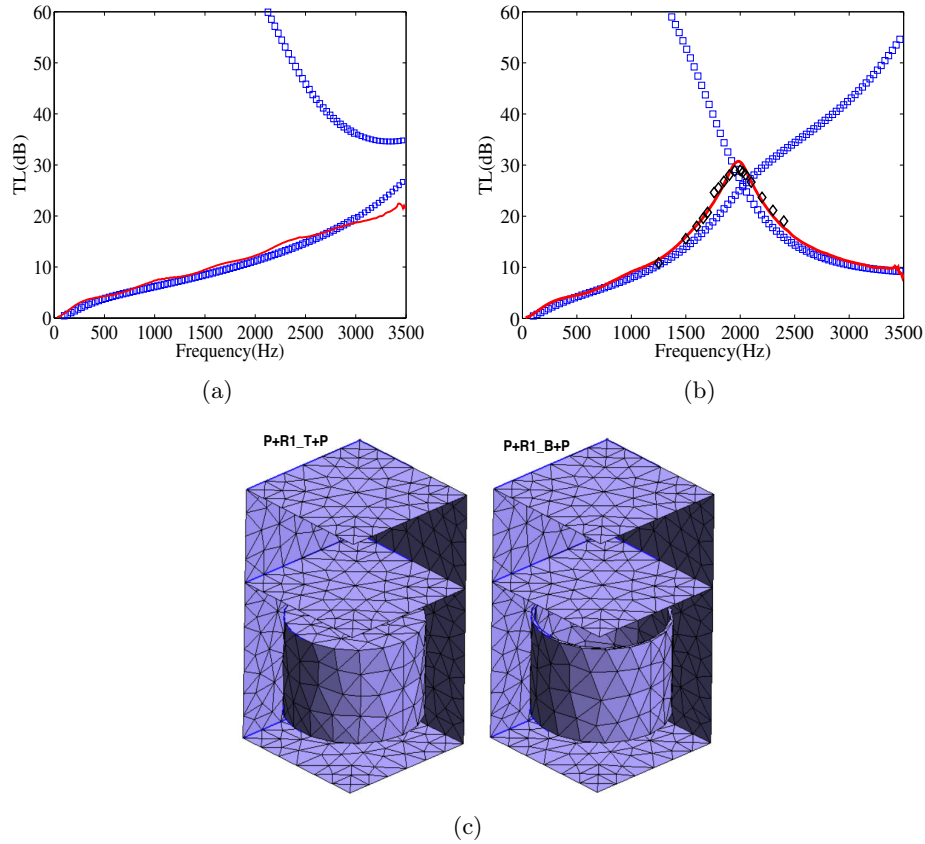


Figure 4.20: Measured transmission loss (solid line) for configurations configurations (a) P+R1_B+P and (b) P+R1_T+P. “ \square ” labels the TLs [26] of the lower two Bloch waves in a periodic waveguide (length $L = 0.2\text{m}$) lined with the two 3D configurations. The ACTIPOLE results are also given by “ \diamond ” in figure (b). (c) The 3D meshes for the two 3D periodic cell [26].

the amplitude of the TL peak is higher while the frequency band is narrower. Biggest absorption coefficient is observed for R1_T around 2200Hz, see Fig. 4.19(d).

A different TL peak is observed around 1700Hz for configuration 2P+R1_T, which is lower than 2000Hz for configurations R1_T+2P and P+R1_T+P. It is because the inclusions are moved below the centre position, leading to a lower frequency at which the crossing between two mode attenuations appears. The effects of the inclusion position embedded in the porous material on the TL peak are also investigated, by moving the inclusion above or below the centre position, the ACTIPOLE results are given in Fig. 4.21(a). We can see that, comparing with the centre position, by moving the inclusions away from the centre, the frequency of the TL peak becomes lower. The shift of the frequency is obvious when the inclusions are moved below the centre position. The

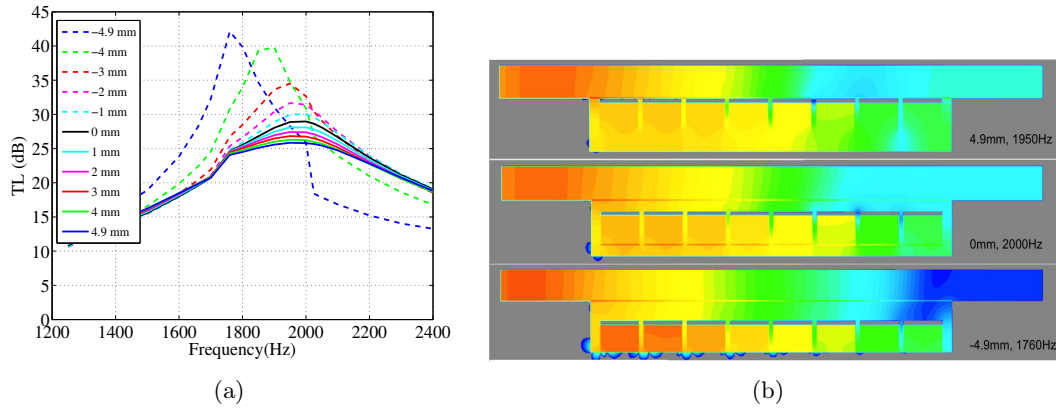


Figure 4.21: (a) The effects of the positions of the inclusions embedded in the porous material (ACTIPOLE results) on the TL. “0 mm” indicates that the inclusions are embedded in the centre, corresponding to P+R1_T+P. “1mm” or “-1mm” means that the inclusions are moved of 1mm above or below the centre position. (b) The pressure field distribution for three different positions of the inclusions at the frequencies of TL peaks.

same phenomenon is observed in Fig.4.13 for the 2D configuration. The amplitude of the TL increases, due to the fact that the pressure localization in the inclusions get stronger with the help of the rigid backing of the big cavity, which can be seen from Fig.4.21(b), where the pressure fields in the waveguides with three different inclusions positions at the frequencies of TL peaks are shown. The smaller the distance between the open ends of the inclusions and the rigid backing, the stronger the pressure localization is. However, for the extreme situation where the open ends of the inclusions reach and attach to the rigid backing, resulting in a closed cavity, no more sound can propagate inside the inclusions, the pressure localization does not exist anymore. That is why the amplitude of TL for 2P+R1_T is smaller.

Fig. 4.19(c) shows the reflection coefficient, due to the presence of the inclusions in the porous materials, the reflection coefficients are smaller than for the porous materials (5P). The absorption coefficient is given in Fig.4.19(d).

From the results in the Figs. 4.18 and 4.19, we can see that configuration 2P+R1_B can improve the TL at high frequency (2500Hz, 3500Hz), while 2P+R1_T at low frequency (1000Hz, 2400Hz), comparing with 5P. These combined effects lead to the global enhancement of the TL at (1000Hz, 3500Hz) for the configuration 2P+R1_A, the results are shown in Fig.4.22(a). It takes the advantages of the closed bottom (2P+R1_B) and the closed top (2P+R1_T), the first peak of 2P+R1_A is due to the maximum TL of 2P+R1_T near 2000Hz, and the TL enhancement for $f > 2500$ Hz is due to the high TL of 2P+R1_B. On one hand, the TL of 2P+R1_A takes the benefits of better TL of the two different arrangements at some frequencies, on the other hand,

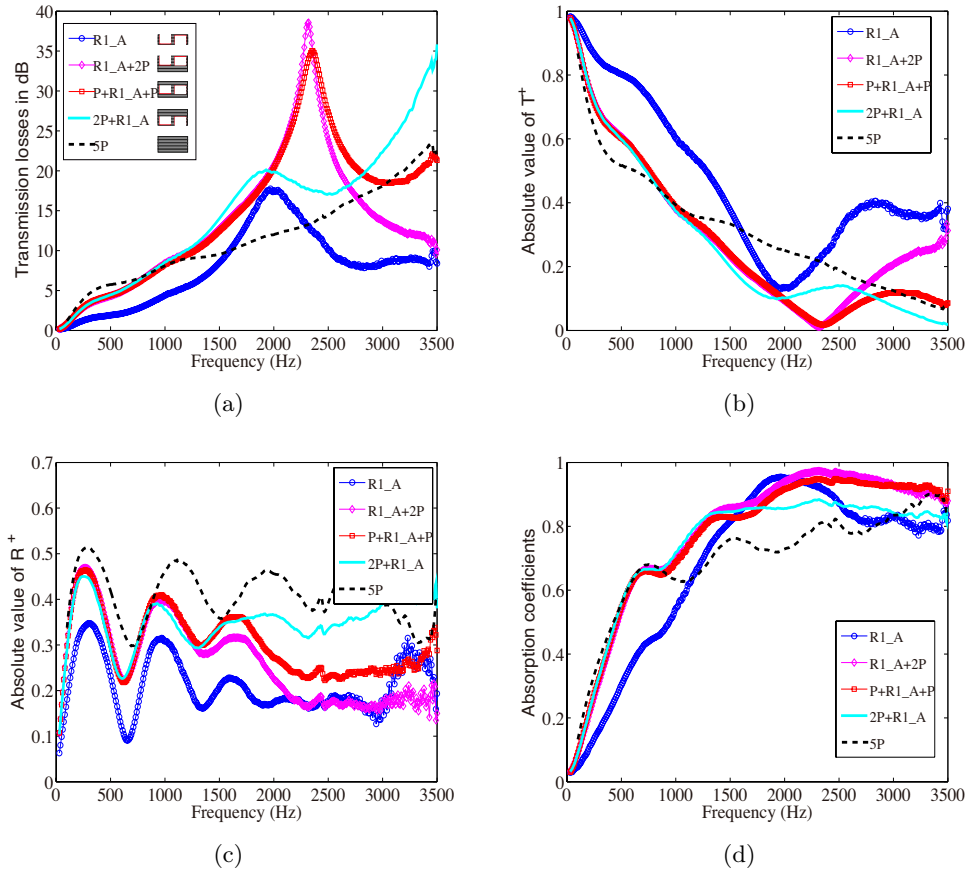


Figure 4.22: (a) Transmission loss, absolute value of (b) T^+ , (c) R^+ , and (d) absorption coefficients when the inclusions are alternated, arrangement (R1_A), and also with the consideration of porous materials layers.

the amplitude of TL decreases. Fig. 4.22 shows the results for the configurations where the inclusions are arranged in an alternated way (R1_A). Different resonant frequencies of TL are observed for different configurations. R1_A+2P and P+R1_A+P have the resonant frequency around 2350 Hz, while 2000 Hz for R1_A and 2P+R1_A. This can also be explained by the sensitivity of the inclusion position in the porous material on the TL peak frequency. Between R1_A and 2P+R1_A, the addition of two layers of porous material makes obvious improvement for the TL of 2P+R1_A.

4.4.3 Experimental results for the configurations with R2

The effect of the second type of inclusion R2 on the transmission loss is also considered. The experimental results for different configurations with R2 are shown in Figs. 4.23, 4.24, and 4.25. For all the three figures, two transmission loss peaks are ob-

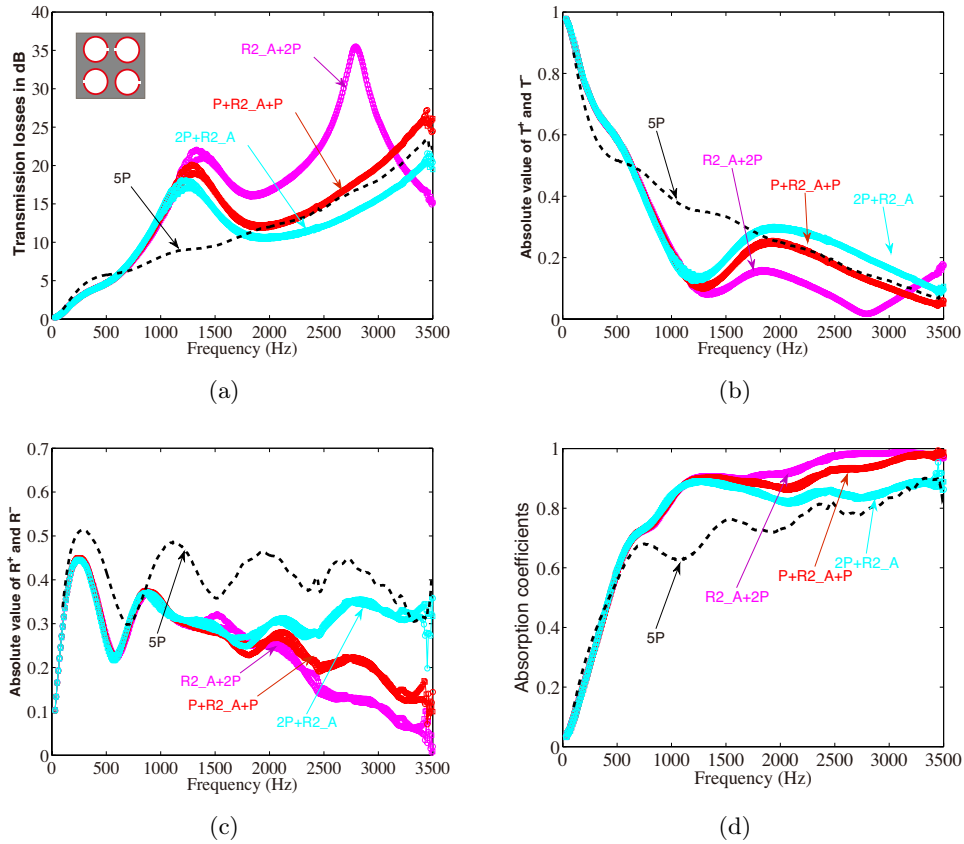


Figure 4.23: (a) Transmission loss, absolute value of (b) T^+ and T^- , (c) R^+ and R^- , and (d) absorption coefficients when the resonators 2 are embedded as R2_A in Fig.4.5(a), and also with different porous material layer arrangements.

served for the configurations R2_A+2P, R2_0°+2P, and R2_90°+2P. To see the effect of the orientation of the resonators on the frequency of the TL peaks, we compare the results in the same figure, see Fig. 4.26. By modulating the orientation of the resonators, the frequency of the first TL peak decreases slightly, while the amplitude of the TL becomes smaller. The frequency of the second TL peak does not change with varying the orientation of R2.

Taking Fig. 4.23(a) as an example, the effect of the other two layers of porous material on the sound propagation can also be seen, by arranging the porous material in different positions (see Fig. 4.5(b)). Fig. 4.23(a) shows the TL of the three different configurations R2_A+2P, P+R2_A+P and 2P+R2_A. The first TL peak is observed for all the three configurations. With increasing the number of porous material layer on the top near the waveguide, the frequency of the first TL peak decreases slightly, which is the same phenomenon we discussed before for R1.

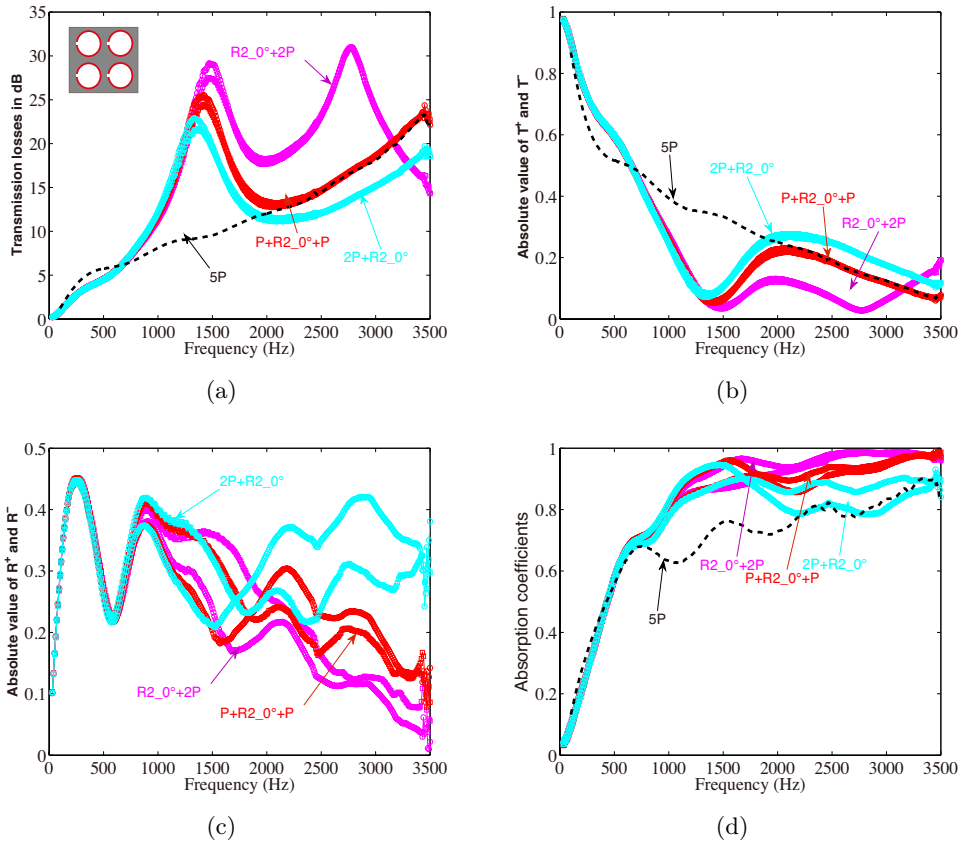


Figure 4.24: The results for the configurations when the resonators 2 are embedded as $R2_{0^\circ}$ in Fig.4.5(a), and also with different porous material layer arrangements.

The second TL peak around 2800Hz is observed only for $R2_A+2P$. From the Actipole results (see Fig. 4.15), the second TL peak for $P+R2_A+P$ ($P+R2_A+P$ here) is at 3400Hz. It means that the porous material has the opposite effects on the second TL peak, comparing with the first TL peak. Bigger the distance between the bottom of the $R2$ and the rigid backing, lower the frequency of the second TL peak is. The second TL peaks is closely related to the mode localization existing between the rigid bottoms of $R2$ and the rigid backing, this can be observed in Fig. 4.17(b). The same effects have also been discussed in Refs. [8, 9], which is explained by the presence of the “underlying” periodic array formed by the inclusions images with respect to the rigid backing. The appearances of the two TL peaks for $R2_A+2P$ lead to a globally enhancement of TL at the frequency range we considered.

Figs.4.23(b)(c) give the absolute values of the transmission and reflection coefficients from both upstream and downstream. The inclusion distribution in the porous material is symmetrical about y -axis, the results for upstream and downstream are supposed

to be the same. Good agreement is observed for the results between the upstream and downstream. Fig.4.23(d) shows the absorption coefficient as a function of the frequency for the three different configurations. The highest absorption is observed for R2_A+2P.

The orientation of the R2 in the porous material is changed to see the effect. In order to avoid the coupling effect near the slits between two inclusions, the inclusions all orient on the same angle. As shown in Figs. 4.5(a), two other different inclusion distributions R2_0° and R2_90° are considered, the results are given in Fig. 4.24 and Fig. 4.25, respectively. The same as we did before, the effect of the porous material is considered. The same phenomenons as in Fig. 4.23(a) and (b) are observed in Fig. 4.24(a)(b) and Fig. 4.25(a)(b). However, for R2_0°, due to the different distribution of the inclusions at the two interfaces $x = 0$ and $x = L$, the reflection coefficients from upstream and downstream are not the same, which also makes the absorption coefficients different, see Figs. 4.24(c)(d).

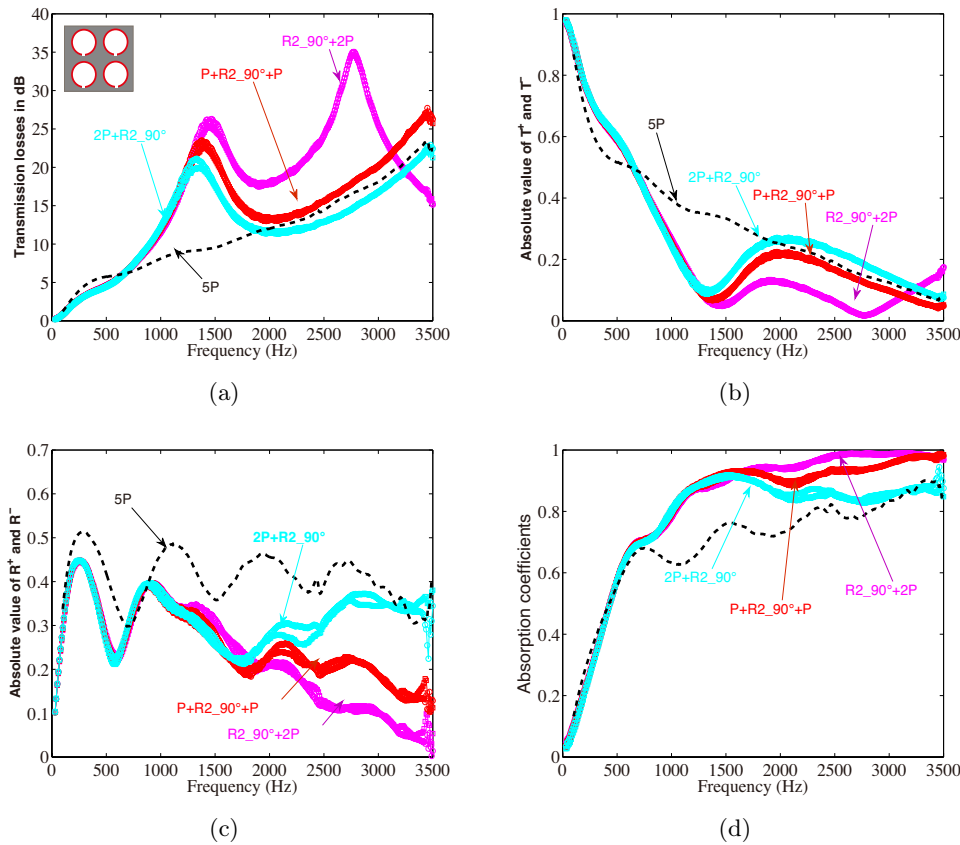


Figure 4.25: The results for the configurations when the resonators 2 are embedded as R2_90° in Fig.4.5(a), and also with different porous material layer arrangements.

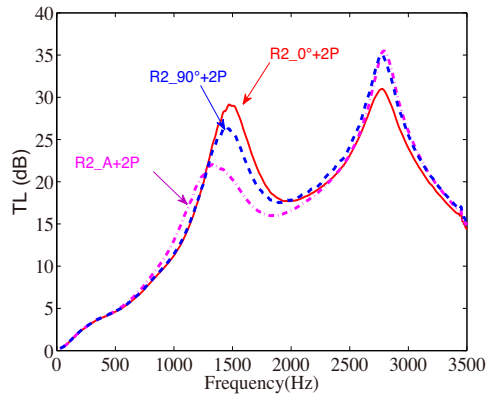


Figure 4.26: TL for different configurations embedded with R2 with the two layers of porous material are under the inclusions.

4.4.4 Comparison between numerical and experimental results

The test sample of P+R1_A+P is shown in Fig.4.4(b). The comparison of the numerical and experimental results for P+R1_A+P and P+R2_A+P are performed, see Figs. 4.27 and 4.28. There is a very good agreement between the numerical and the experimental results, despite a general trend for ACTIPOLE to over-predict the peak of attenuation.

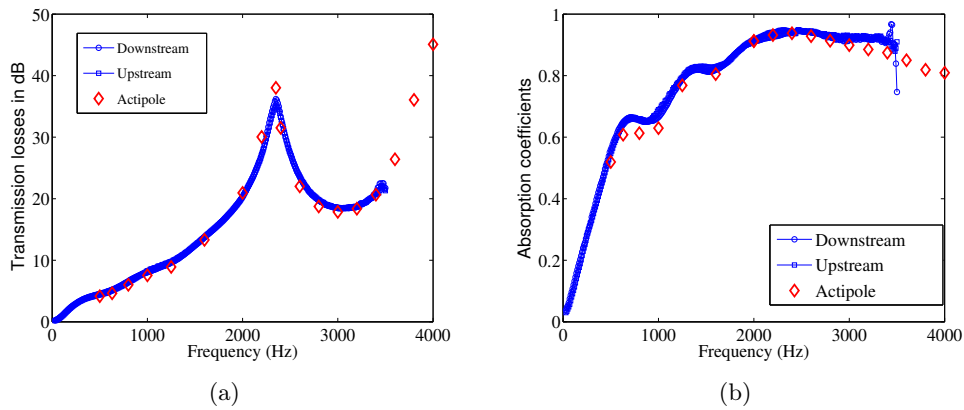


Figure 4.27: Comparisons between Actipole computation and the measurement results for P+R1_A+P (a) transmission loss, and (b) absorption coefficients.

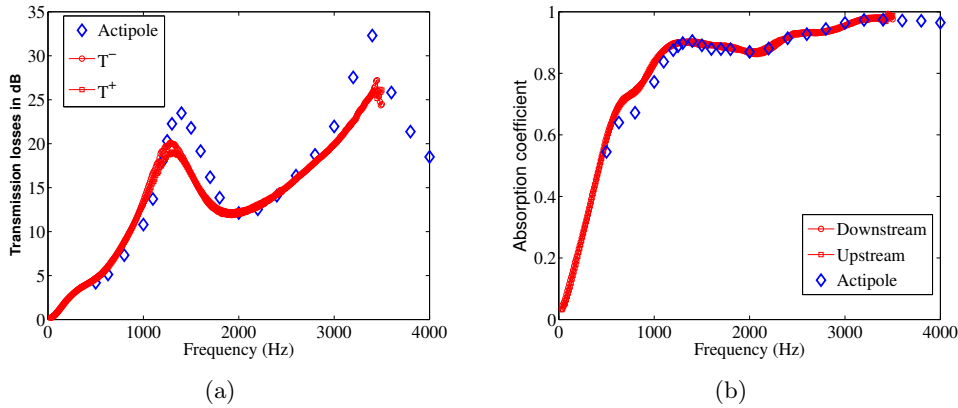


Figure 4.28: Comparisons between Actipole computation and the measurement results for P+R2_A+P (a) transmission loss, and (b) absorption coefficients.

4.5 Conclusions

An analysis of a 2D infinite periodic waveguide with inclusions embedded in porous material is performed by using Floquet-Bloch theorem. A maximum sound attenuation for this infinite periodic waveguide can be reached near the crossing (or avoided crossing) of the mode attenuations between two lower Bloch waves. The avoided crossing is related to the exceptional point. A coupling between acoustic mode and localized mode is happened near this crossing. This is the second strategy we presented in this chapter.

The influence of the periodical array of 3D inclusions embedded in the porous material on the transmission loss of an acoustic duct is studied numerically and experimentally. Two different inclusion shapes are considered, an open cylinder and a Helmholtz resonator. When the rigid inclusions are embedded in the porous material, the low frequency behaviours of the transmission loss can be significantly changed, peaks are observed in the mid-frequency range. The effects of the inclusion position on the TL peak frequency are different for different inclusion shapes. For the configurations with open cylinder, the frequency of the TL peak becomes lower when the open cylinders are moved away from the centre. The peaks can also be explained by the crossing phenomenon, due to the mode coupling of the Bloch waves. For the configurations with Helmholtz resonator, the frequency of the first TL peak increases with increasing the distance between the inclusions and the rigid backing, while the frequency of second peak decreases. The second TL peak is due to the localized mode observed between the rigid bottoms of the resonator and the rigid backing.

Good agreements are observed between the experimental and numerical results, which opens the way to the optimisation of metaporous material for better sound attenuation at low frequencies.

Appendix

4.A Equivalent fluid model

The porous material we used here is a metallic foam. Rigid frame porous material is modelled using the Johnson-Champoux-Allard model. The dynamic compressibility κ_{eq} and dynamic density ρ_{eq} are [27, 28]

$$\rho_{eq} = \frac{\rho_a \alpha_\infty}{\Phi} \left(1 + \frac{1}{jx} \left[1 + \frac{M}{2} jx \right] \right),$$

$$\kappa_{eq} = \frac{\gamma P_0}{\Phi} \left(\gamma - (\gamma - 1) \left(1 + \frac{1}{jx'} \left[1 + \frac{M'}{2} jx' \right]^{1/2} \right)^{-1} \right)^{-1},$$

with

$$x = -\frac{\omega \alpha_\infty k_0}{\nu \phi}, M = \frac{8k_0 \alpha_\infty}{\Phi \Lambda^2}, x' = -\frac{\omega \text{Pr} k'_0}{\nu \phi}, \text{ and } M' = \frac{8k_0}{\Phi \Lambda'^2}.$$

Here, Φ is the porosity, α_∞ is the Johnson Koplik & Dashen tortsity factor [29], k_0 is Darcy's viscous permeability, Λ is the Johnson Koplik & Schwartz pore size parameter [29], k'_0 (which can be approximated by $k'_0 = \Phi \Lambda'^2 / 8$) is the Lafarge et. al. thermal permeability [27] and Λ' is the Champoux & Allard pore size parameter [30]. Thermodynamic properties of the saturating air are given by: ρ_a the ambient density, γ is the air specific heat ratio, P_0 is the atmospheric pressure, Pr is the Prandtl number. The relation between the resistivity σ and the kinematic viscosity ν can be written as $\sigma = \rho_a \nu / k_0$.

4.B Eigenvalue problem in a porous lined duct

For a uniform infinite waveguide filled by air (with height h_a) and porous materials (with height h_p), the eigenvalue problem can be solved by Finite Difference Method (FDM). The principle of the FDM is that: Derivatives in the partial differential equation are approximated by linear combinations of function values at the grid points. There are $N_a = h_a / \Delta h$ and $N_p = h_p / \Delta h$ discrete points in the air and porous mediums, respectively, we denote $N_2 = N_a + N_p$, where Δh is the spacing between interior points, and the first and last points are taken $\Delta h / 2$ from the the duct walls. The pressure values at different discrete points are

$$P_i = P(y_i), \quad i = 1, 2, \dots, N_2,$$

Without resistance sheet, we have

$$G_a = \frac{2\rho_a}{\rho_a + \rho_{eq}} \left(\frac{\rho_{eq}}{2\rho_0} + \frac{2}{3} \right), G_b = \frac{2\rho_a}{\rho_a + \rho_{eq}} \left(-\frac{\rho_{eq}}{2\rho_0} - 2 \right), G_c = \frac{2\rho_a}{\rho_a + \rho_{eq}} \frac{3}{2}, G_d = \frac{2\rho_a}{\rho_a + \rho_{eq}} \left(\frac{1}{2} - \frac{2}{3} \right)$$

and

$$M_a = \frac{2\rho_{eq}}{\rho_a + \rho_{eq}} \left(\frac{1}{2} - \frac{2}{3} \right), M_b = \frac{2\rho_{eq}}{\rho_a + \rho_{eq}} \frac{3}{2}, M_c = \frac{2\rho_{eq}}{\rho_a + \rho_{eq}} \left(-\frac{\rho_a}{2\rho_{eq}} - 2 \right), M_d = \frac{2\rho_{eq}}{\rho_a + \rho_{eq}} \left(\frac{\rho_a}{2\rho_{eq}} + \frac{2}{3} \right).$$

4.C Scattering matrix of a unit cell

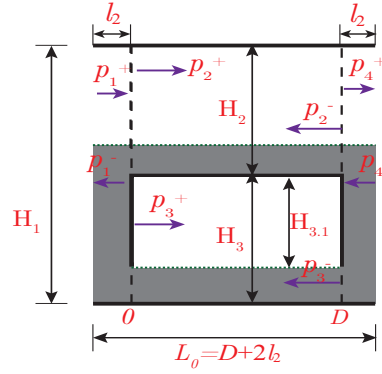


Figure 4.29: Geometry of one elementary cell.

To obtain the scattering matrix S of one elementary cell, the cell is divided into 4 segments (see Fig. 4.29), according to Eq. (4.11), the pressures at different segments can be written as

$$\mathbf{p}_1(x) = X_1 E_1(x) C_1^+ + X_1 E_1(-x) C_1^-, \quad (4.22)$$

$$\mathbf{p}_2(x) = X_2 E_2(x) C_2^+ + X_2 E_2(D-x) C_2^-, \quad (4.23)$$

$$\mathbf{p}_3(x) = X_3 E_3(x) C_3^+ + X_3 E_3(D-x) C_3^-, \quad (4.24)$$

$$\mathbf{p}_4(x) = X_1 E_1(x-D) C_4^+ + X_1 E_1(D-x) C_4^-, \quad (4.25)$$

where 1, 2, 3, and 4 are used to label the 4 segments, and D is the width of the inclusion.

The continuity conditions of the \mathbf{p} and $\partial\mathbf{p}/\partial x$ at the interfaces $x = 0$ and $x = D$ lead to

$$\begin{aligned} X_1^1(C_1^+ + C_1^-) &= X_2(C_2^+ + E_{2D}C_2^-), \\ X_1^3(C_1^+ + C_1^-) &= X_3^2(C_3^+ + E_{3D}C_3^-), \\ X_1^1K_{1x}(C_1^+ - C_1^-) &= X_2K_{2x}(C_2^+ - E_{2D}C_2^-), \\ X_1^3K_{1x}(C_1^+ - C_1^-) &= X_3^2K_{3x}(C_3^+ - E_{3D}C_3^-), \\ X_1^2K_{1x}(C_1^+ - C_1^-) &= 0, \\ 0 &= X_3^1K_{3x}(C_3^+ - E_{3D}C_3^-), \end{aligned}$$

and

$$\begin{aligned} X_1^1(C_4^+ + C_4^-) &= X_2(E_{2D}C_2^+ + C_2^-), \\ X_1^3(C_4^+ + C_4^-) &= X_3^2(E_{3D}C_3^+ + C_3^-), \\ X_1^1K_{2x}(C_4^+ - C_4^-) &= X_2K_{2x}(E_{2D}C_2^+ - C_2^-), \\ X_1^3K_{1x}(C_4^+ - C_4^-) &= X_3^2K_{3x}(E_{3D}C_3^+ - C_3^-), \\ X_1^2K_{1x}(C_4^+ - C_4^-) &= 0, \\ 0 &= X_3^1K_{3x}(E_{3D}C_3^+ - C_3^-). \end{aligned}$$

These continuity equations can be rewritten in a matrix form

$$M_1 \begin{pmatrix} C_1^- \\ C_4^+ \\ C_2^+ \\ C_2^- \\ C_3^+ \\ C_3^- \end{pmatrix} = M_2 \begin{pmatrix} C_1^+ \\ C_4^- \end{pmatrix}, \quad (4.26)$$

where M_1 and M_2 are the matrices used to relate the amplitudes at different segments. The scattering matrix (denoted as S_D) between $x = 0$ and D , which relates incoming (C_1^+ and C_4^-) and outgoing (C_1^- and C_4^+) modes, can be truncated from matrix $M_1^{-1}M_2$ by

$$S_D = M_1^{-1}M_2(1 : 2N_2, 1 : 2N_2).$$

For an porous lined duct with length l_2 , the scattering matrix is

$$S_{l_2} = \begin{bmatrix} 0 & E_1(l_2) \\ E_1(l_2) & 0 \end{bmatrix}. \quad (4.27)$$

With the addition of two uniform duct of finite length l_2 on both sides, the scattering matrix S of a elementary cell in Figs. 4.6 and 4.29 is obtained by

$$S = S_{l_2} \otimes S_D \otimes S_{l_2}. \quad (4.28)$$

Following Furnell and Bies [31] the operation \otimes can be defined by

$$\mathbf{S}^{(1+2)} = \mathbf{S}_1 \otimes \mathbf{S}_2 = \begin{bmatrix} \mathbf{R}^{(1+2)} & \mathbf{t}^{(1+2)} \\ \mathbf{T}^{(1+2)} & \mathbf{r}^{(1+2)} \end{bmatrix}$$

with

$$\begin{aligned} \mathbf{T}^{(1+2)} &= \mathbf{T}_2 \mathbf{E} \mathbf{T}_1, \mathbf{t}^{(1+2)} = \mathbf{t}_1 \mathbf{F} \mathbf{t}_2, \\ \mathbf{R}^{(1+2)} &= \mathbf{R}_1 + \mathbf{t}_1 \mathbf{F} \mathbf{R}_2 \mathbf{T}_1, \mathbf{r}^{(1+2)} = \mathbf{r}_2 + \mathbf{T}_2 \mathbf{E} \mathbf{r}_1 \mathbf{t}_2, \\ \mathbf{E} &= (\mathbf{I} - \mathbf{r}_1 \mathbf{R}_2)^{-1}, \mathbf{F} = (\mathbf{I} - \mathbf{R}_2 \mathbf{r}_1)^{-1}, \end{aligned}$$

where \mathbf{I} is the identity matrix, and $(\mathbf{T}_1, \mathbf{t}_1, \mathbf{R}_1, \mathbf{r}_1)$ and $(\mathbf{T}_2, \mathbf{t}_2, \mathbf{R}_2, \mathbf{r}_2)$ are the elements of matrices \mathbf{S}_1 and \mathbf{S}_2 , respectively.

Bibliography

- [1] H. H. Hubbard, *Aeroacoustics of Flight Vehicles: Theory and Practice, Vol. 2, Noise Control*. NASA Reference Publication 1258, pp. 165–205, 1991.
- [2] J.-F. Allard, *Propagation of Sound in Porous Media: Modeling Sound Absorbing Materials*. (Chapman and Hall, New York), pp 280, 1993.
- [3] O. Tanneau, J. B. Casimir, and P. Lamary, “Optimization of multilayered panels with poroelastic components for an acoustical transmission objective,” *The Journal of the Acoustical Society of America*, vol. 120, no. 3, pp. 1227–1238, 2006.
- [4] L. Brekovskikh, *Waves in Layered Media*. (Academic, New York), 1960.
- [5] Z. Liu, X. Zhang, Y. Mao, Y. Zhu, Z. Yang, C. Chan, and P. Sheng, “Locally resonant sonic materials,” *Science*, vol. 289, pp. 1734–1736, Sept. 2000.
- [6] Z. Liu, C. Chan, and P. Sheng, “Analytic model of phononic crystals with local resonances,” *Phys. Rev. B*, vol. 71, Jan. 2005.
- [7] N. Fang, D. Xi, J. Xu, M. Ambati, W. Srituravanich, C. Sun, and X. Zhang, “Ultrasonic metamaterials with negative modulus,” *Nat Mater*, vol. 5, pp. 452–456, June 2006.
- [8] J. Groby, O. Dazel, A. Duclos, L. Boeckx, and L. Kelders, “Enhancing the absorption coefficient of a backed rigid frame porous layer by embedding circular periodic inclusions,” *J. Acoust. Soc. Am.*, vol. 130, no. 6, p. 3771, 2011.
- [9] B. Nennig, Y. Renou, J.-P. Groby, and Y. Aurégan, “A mode matching approach for modeling two dimensional porous grating with infinitely rigid or soft inclusions,” *J. Acoust. Soc. Am.*, vol. 131, no. 5, pp. 3841–3852, 2012.
- [10] J.-P. Groby, C. Lagarrigue, B. Brouard, O. Dazel, V. Tournat, and B. Nennig, “Using simple shape three-dimensional rigid inclusions to enhance porous layer absorption,” *The Journal of the Acoustical Society of America*, vol. 136, no. 3, pp. 1139–1148, 2014.

-
- [11] B. Nennig, Y. Renou, and Y. Aurégan, “On the use of periodic inclusions embedded in porous lining to enhanced attenuation in waveguides,” *Société Française d’Acoustique*, Apr. 2012.
- [12] C. Engström, C. Hafner, and K. Schmid, “Computations of lossy bloch waves in two-dimensional photonic crystals,” *J. Comput. Theor. Nanosci.*, vol. 6, pp. 775–783, 2009.
- [13] C. E. Bradley, “Time harmonic acoustic bloch wave propagation in periodic waveguides. part i. theory,” *The Journal of the Acoustical Society of America*, vol. 96, no. 3, pp. 1844–1853, 1994.
- [14] A. Duclos, D. Lafarge, and V. Pagneux, “Transmission of acoustic waves through 2d phononic crystal: visco-thermal and multiple scattering effects,” *Eur. Phys. J. Appl. Phys.*, vol. 45, no. 3, p. 11302, 2009.
- [15] F. Barra, A. Maurel, V. Pagneux, and J. Zuñiga, “Number of propagating modes of a diffusive periodic waveguide in the semiclassical limit,” *Phys. Rev. E*, vol. 81, p. 066210, Jun 2010.
- [16] Y. Aurégan and D. Kumar Singh, “Experimental observation of a hydrodynamic mode in a flow duct with a porous material,” *J. Acoust. Soc. Am.*, vol. 136, no. 2, pp. 567–572, 2014.
- [17] Y. Aurégan and M. Leroux, “Failures in the discrete models for flow duct with perforations: an experimental investigation,” *Journal of Sound and Vibration*, vol. 265, no. 1, pp. 109–121, 2003.
- [18] G. Ajello, *Mesures acoustiques dans les guides d’ondes en presence d’écoulement: mise au point d’un banc de mesure*. PhD thesis, Université du Maine, Le Mans, Dec. 1997.
- [19] A. Delnevo, S. L. Saint, G. Sylvand, and I. Terrasse, “Numerical Methods: Fast Multipole Method for Shielding Effects,” in *11th AIAA/CEAS Aeroacoustics Conference*, Aeroacoustics Conferences, pp. AIAA Paper 2005–2971, American Institute of Aeronautics and Astronautics, May 2005.
- [20] J.-F. Allard and N. Atalla, *Propagation of Sound in Porous Media: Modeling Sound Absorbing Materials*. (Wiley, Chichester), CHap. 5, pp 73-107, 2009.
- [21] J. D. Joannopoulos, R. D. Meade, and J. N. Winn, *Photonic Crystals: Molding the Flow of Light, 2nd ed.* (Princeton University Press, New Jersey), pp 286, 2008.
- [22] L. Brillouin, *Wave Propagation in Periodic Structures*. McGraw-Hill, New York, Jan. 1946.

-
- [23] B. Tester, “The optimization of modal sound attenuation in ducts, in the absence of mean flow,” *Journal of Sound and Vibration*, vol. 27, no. 4, pp. 477 – 513, 1973.
- [24] L. Cremer, “Theory of sound attenuation in a rectangular duct with an absorbing wall and the resultant maximum attenuation coefficient,” *Acustica*, vol. 2, pp. 249–263, Jan. 1953.
- [25] W. Bi and V. Pagneux, “New insights into mode behaviours in waveguides with impedance boundary conditions,” *ArXiv e-prints*, *arXiv:1511.05508 [quant-ph]*, Nov. 2015.
- [26] B. Nenning, “The use of metamaterials in duct acoustics : Comparison with bloch waves.,” *Internal report*, pp. 1–5, 2015.
- [27] D. Lafarge, P. Lemarinier, J. F. Allard, and V. Tarnow, “Dynamic compressibility of air in porous structures at audible frequencies,” *The Journal of the Acoustical Society of America*, vol. 102, no. 4, pp. 1995–2006, 1997.
- [28] D. L. Johnson, J. Koplik, and R. Dashen, “Theory of dynamic permeability and tortuosity in fluid-saturated porous media,” *Journal of Fluid Mechanics*, vol. 176, pp. 379–402, 3 1987.
- [29] D. L. Johnson, J. Koplik, and L. M. Schwartz, “New pore-size parameter characterizing transport in porous media,” *Phys. Rev. Lett.*, vol. 57, pp. 2564–2567, Nov 1986.
- [30] Y. Champoux and J. Allard, “Dynamic tortuosity and bulk modulus in air saturated porous media,” *Journal of Applied Physics*, vol. 70, no. 4, pp. 1975–1979, 1991.
- [31] G. D. Furnell and D. A. Bies, “Matrix analysis of acoustic wave propagation within curved ducting systems,” *Journal of Sound and Vibration*, vol. 132, no. 2, pp. 245 – 263, 1989.

Chapter 5

Acoustical behavior of purely reacting liners

This chapter¹ investigates the acoustical behaviors of a rectangular duct lined with a purely locally-reacting liner in both absence and presence of flow. Multi-Model Method is proposed to solve the problem in the absence and presence of uniform flow. The results exhibit an unusual acoustical behavior: for a certain range of frequencies, no wave can propagate against the flow. The effect of shear flow is investigated by using Chebyshev Spectral Method, which provides detailed information near the walls. A negative group velocity is found in a certain range of frequencies and a *zero* group velocity is found at two critical frequencies. It is demonstrated that the sound can be slowed down and even stopped.

5.1 Introduction

Nowadays, acoustical liner are widely used to reduce aircraft engine noise emission by damping the acoustic modes propagating within the inlet or the exhaust ducts. Typically, the lining is usually assumed to be locally-reacting liner. Commonly, the interaction of acoustics with the lining is characterized by the impedance of the liner, which then is used as the boundary condition to construct the eigenvalue problem. In the absence of flow, the problem is straightforward. The acoustic transmission coefficient in a rigid duct partially lined with the locally-reacting liner has a minimum value at the resonant frequency of the liner impedance (when the depth of the liner is $(2n + 1)\lambda/4$ with n a integer). In presence of the flow, an instability can appear.

1. Part of this work is presented and published in 19th AIAA/CEAS Aeroacoustics Conference (AIAA 2013-2077): Y. Aurégan, L. Xiong, and W. Bi, “Acoustical behaviour of purely reacting liner”.

The instability was demonstrated experimentally by Aurégan *et al.* [1] [2]: There is an increase in the transmission coefficient at the resonant frequency, and the authors explained that this behavior was caused by the hydrodynamic instability over the liner. Rienstra [3] analyzed the behavior of the acoustic modes of a lined duct with and without uniform mean flow, it is shown that there exists three types of modes: genuine acoustic modes, acoustic surface waves and hydrodynamic surface waves. Subsequently, Brambley and Peake [4] further investigated the behavior of the surface modes. It's well known that when the flow exists, the viscosity effects cannot be omitted especially near the walls, and so the boundary layer has to be considered. The Ingard-Myers [5] [6] boundary condition, which is derived under the assumption that the partial displacement is continuous across the vorticity sheet [6], is commonly used for the analytical prediction of sound propagation in ducts with flow. But then, Aurégan *et al.* [7] pointed out that depending on the ratio of the acoustic and stationary boundary layer thicknesses, the kinematic wall condition changes gradually from continuity of normal acoustic displacement to continuity of normal acoustic mass velocity. Renou [8] performed an experimental investigation, the results show that the Ingard-Myers boundary condition fails to predict with accuracy the acoustic behavior in a lined duct with flow.

For the past few years, the investigators have done lots of work about the modes existing in the lined duct in the presence of flow, especially the *surface modes*, and the instability problem caused by the coupling of the flow and the lining. In the present work, we focus our attention on the propagation problem in a two-dimensional acoustic partially lined duct with presence of flow, the liner is purely reactive. For a certain range of frequencies and Mach numbers, no wave can propagate against the flow. In Sec. 5.2, the case without flow is first reviewed, in the vicinity of the resonant frequency, a zero in the transmission coefficient is observed. In Sec. 5.3, in the presence of uniform flow, the modes in the liner and the transmission coefficient in two directions are investigated. In Sec. 5.4, the modes in the rigid duct with shear flow are first investigated. Attention is focused on the modes in the lined duct with shear flow and the transmission behaviour.

5.2 Propagation in the reacting lined ducts without flow

5.2.1 Modes in the lined ducts without flow

Statement of the problem

First, we consider the modes in an infinite lined duct without flow. For the infinite duct, the upper wall is rigid and the lower wall is lined with a locally-reacting liner, see Fig. 5.1. The acoustic pressure expression in the 2D coordinate can be written as

$$p(x, y) = \psi(y)e^{(-j\omega t + jkx)}, \quad (5.1)$$

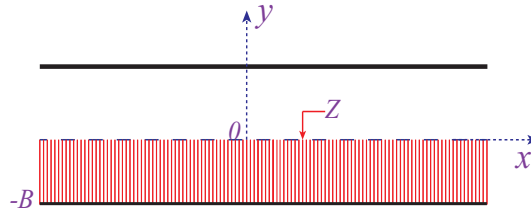


Figure 5.1: Scheme of the infinite reacting lined duct. Z is the impedance of the liner with B the thickness.

and $\psi(y)$ satisfies the Helmholtz equation

$$\frac{d^2\psi(y)}{dy^2} + \beta^2\psi(y) = 0, \quad (5.2)$$

where $\beta^2 = \omega^2 - k^2$ is the eigenvalues of the transverse modes in the lined duct. It is noted that the equations are written in a dimensionless form with the pressure p normalized by ρc_0^2 , x and y by width H , t by H/c_0 , where ρ is the air density and c_0 is the sound velocity. Then $\omega = \frac{2\pi f}{c_0}H$ is the dimensionless frequency or Helmholtz number. Time dependence is $\exp(-j\omega t)$, and will be omitted in the following.

The solution of Eq. (5.2) is given by

$$\psi(y) = A_1 \cos(\beta y) + B_1 \sin(\beta y), \quad (5.3)$$

where A_1 and B_1 can be computed from boundary conditions. The boundary conditions have to be applied to solve the eigenvalue problem. For the rigid wall, $y = 1$, the acoustic particle velocity normal to the wall vanishes, i.e.

$$\left. \frac{d\psi}{dy} \right|_{y=1} = 0. \quad (5.4)$$

For the lined wall, $y = 0$, the admittance boundary condition

$$\left. \frac{d\psi}{dy} \right|_{y=0} = -j\omega Y(\omega)p|_{y=0} \quad (5.5)$$

has to be used, where Y is the normalized admittance of the lined wall. It can be obtained by $Y(\omega) = 1/Z(\omega)$. Since purely reacting liner is considered here, we can derive the expression of the impedance analytically (see Appendix 5.A). With the consideration of the dissipation, the impedance of the liner in Fig. 5.1 can be approximately by

$$Z(\omega) = R + j \cot(\omega b), \quad (5.6)$$

where $b = B/H$ is the normalized thickness of the liner, and R is the normalized resistance. In the following, we assume $R = 0$, which leads to

$$Y(\omega) = -j \tan(\omega b). \quad (5.7)$$

Substituting the pressure expression, Eq. (5.3), into the boundary conditions, Eqs. (5.4) and (5.5), results in $B_1 = 0$ and the eigenvalue equation

$$\beta \tan \beta = -\omega \cdot \tan(\omega b). \quad (5.8)$$

In the limit of low frequency ($\omega \ll 1$ and $\beta \ll 1$), from Eq.(5.8), we can have $\beta^2 = -b\omega^2$ and $\psi(y) = A \cosh(\beta y)$, and then the wavenumber in x -direction is approximated by $k/\omega = \pm(1 + b)^{1/2}$. The reduced phase velocity $c_\phi = \omega/k$ is then smaller than 1, which demonstrates that the phase velocity c_ϕ is smaller than the sound velocity c_0 . The propagative waves are kind of waves which propagate in x -direction along with a exponentially decrease away from the lined wall.

Multimodal Method

In order to calculate the eigenvalues and eigenfunctions of the transverse modes in the lined duct more quickly and efficiently, in the present paper, the Multi-Model Method [9] is proposed to solve the dispersion relation and to obtain the transmission coefficient. For a rigid rectangular duct, the eigenvalues and the eigenfunctions are well known, namely,

$$\phi_n(y) = \Lambda_n \cos(\alpha_n y), \quad \Lambda_n = \begin{cases} 1 & n = 0 \\ \sqrt{2} & n \neq 0 \end{cases}, \quad (5.9)$$

where $\alpha_n = n\pi$, $n = 0, 1, 2, 3 \dots$.

The eigenfunction $\psi(y)$ in the lined duct is projected on the complete basis of functions $\phi_n(y)$ by

$$\psi(y) = \sum_{n=0}^N A_n \phi_n(y) = \vec{\Phi}^T \vec{A}, \quad (5.10)$$

where \vec{A} and $\vec{\Phi}$ are column vectors, their elements are the coefficients A_n of the basis functions and the basis function $\phi_n(y)$, respectively. N is the truncation number. The superscript “ T ” indicates the transpose.

Multiplying by $\vec{\Phi}(y)$ on both sides of Eq.(5.2), and integrating over y coordinate, we can have

$$\int_0^1 \vec{\Phi}(y) (\omega^2 - k^2) \psi(y) dy + \int_0^1 \vec{\Phi}(y) \frac{\partial^2 \psi(y)}{\partial y^2} dy = 0. \quad (5.11)$$

The rigid eigenfunction $\phi_m(y)$ is orthogonal

$$\int_0^1 \phi_m(y)\phi_n(y)dy = \begin{cases} 1 & m = n \\ 0 & m \neq n \end{cases}.$$

With the help of the boundary conditions Eqs.(5.4)(5.5) and Eq.(5.10), the second integral term in Eq.(5.11) can be solved by

$$\begin{aligned} \int_0^1 \vec{\Phi} \frac{\partial^2 \psi(y)}{\partial y^2} dy &= \vec{\Phi} \frac{\partial \psi(y)}{\partial y} \Big|_0^1 - \int \frac{\partial \vec{\Phi}}{\partial y} \frac{\partial \psi(y)}{\partial y} dy \\ &= 0 - \vec{\Phi}(0) \frac{\partial p(0)}{\partial y} - \left(\frac{\partial \vec{\Phi}(y)}{\partial y} \psi(y) \Big|_0^1 - \int \frac{\partial^2 \vec{\Phi}(y)}{\partial y^2} \psi(y) dy \right), \\ &= j\omega Y \vec{\Phi}(0) p(0) - \vec{\alpha}^2 \int \vec{\Phi}(y) \psi(y) dy \\ &= j\omega Y \mathbf{N}_1 \vec{A} - \mathbf{N}_2 \vec{A} \end{aligned} \quad (5.12)$$

where \mathbf{I} is the identity matrix, $\vec{\alpha}$ is a column vector with elements α_n , and the elements of matrix \mathbf{N}_1 can be obtained by

$$\mathbf{N}_{1m,n} = \phi_m(0)\phi_n(0).$$

The matrices \mathbf{N}_1 and \mathbf{N}_2 are written as

$$\mathbf{N}_1 = \begin{pmatrix} 1 & \sqrt{2} & \sqrt{2} & \cdots \\ \sqrt{2} & 2 & 2 & \cdots \\ \sqrt{2} & 2 & 2 & \cdots \\ \vdots & & & \cdots \end{pmatrix}, \quad \mathbf{N}_2 = \begin{pmatrix} \alpha_0^2 & 0 & \cdots \\ 0 & \alpha_1^2 & \\ \vdots & & \ddots \end{pmatrix}.$$

Equation (5.11) can be reformulated as a matrix eigenvalue problem

$$k^2 \mathbf{I} \vec{A} = [\omega^2 \mathbf{I} + \omega \tan(\omega b) \mathbf{N}_1 - \mathbf{N}_2] \vec{A}. \quad (5.13)$$

By computing the matrix generalized eigenvalue problem of Eq.(5.13), for a given ω , we can obtain the eigenvalues λ and the corresponding eigenvectors X . The axial wavenumbers are calculated by $k^2 = \lambda$. A purely reacting liner is considered here, so the wavenumber k is either purely real or purely imaginary values.

The eigenvalues β and eigenfunctions $\psi(y)$, Eq. (5.10), in the transverse direction can be obtained by solving the following eigenproblem

$$\beta^2 \mathbf{I} \vec{A} = [\mathbf{N}_2 - j\omega Y \mathbf{N}_1] \vec{A}. \quad (5.14)$$

In Fig. 5.2, we plot the motions of the eigenvalues β as a function of frequency ω with $b = B/H = 50/15$ m. The dashed lines in Fig. 5.2(a) label the eigenvalues of transverse modes in rigid duct, i.e. $\alpha_n = n\pi$. Due to the purely imaginary value of the admittance Y , the eigenvalues β are purely real or imaginary values. The eigenvalue of the plane

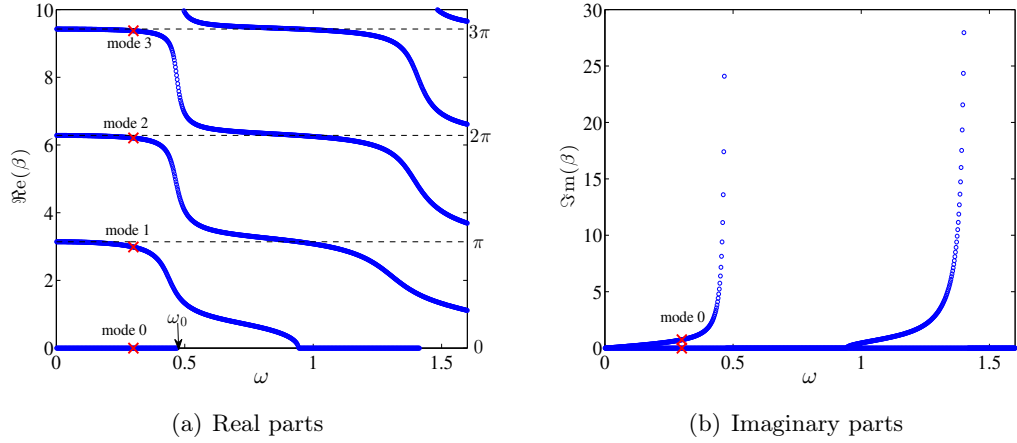


Figure 5.2: Trajectories of the (a) real parts and (b) imaginary parts of β as a function of frequency ω with $b = B/H = 50/15$ m.

mode in the rigid duct, $\alpha_0 = 0$, turns to be purely imaginary value for $0 < \omega < \omega_R$, where ω_R is the quarter-wavelength resonant frequency of the liner, i.e. $\omega_R b = \pi/2$. From the eigenfunction profile (solid line in Fig. 5.3(a)) of the mode 0, the amplitude decreases away from the lined wall, $y = 0$. If the frequency ω is closer to ω_R , the amplitude of the mode 0 decreases faster, the wave becomes more and more concentrated near the lined wall, so-called surface mode [3]. This is also illustrated in Fig. 5.6 where the pressure field is computed. The profiles of the other three modes are also shown in the same Fig. 5.3(a). They can be classified by the number of the pressure node in transverse direction.

By Eq. (5.13), we also plot the dispersion curves of the first mode in x -direction, see Fig. 5.3(b), the real and imaginary parts of the wavenumber k as a function of ω are shown. Purely real values of k indicate the propagative modes. $\Re(k) > 0$ indicates that the mode propagates in $+x$ -direction. It shows that there exists a frequency *band gap*, in which no mode can propagate. In fact, at this frequency range, the values of k become purely imaginary (see the bottom figure in Fig. 5.3(b)), they become the evanescent modes in x direction. The band gap starts with the resonant frequency ω_R , quarter-wavelength frequency of the locally reacting liner, at which the wavenumber becomes infinite. Since $k = 2\pi/\lambda_x$, then the wavelength in x direction, λ_x , tends to be *zero*. These can also be explained by the expression of the admittance, Eq. (5.7), when $0 < \omega b < \pi/2$, $\Im m(Y) < 0$; when $\omega b = \pi/2$, $\Im m(Y) \rightarrow \infty$; and when $\pi/2 < \omega b < \pi$, $\Im m(Y) > 0$.

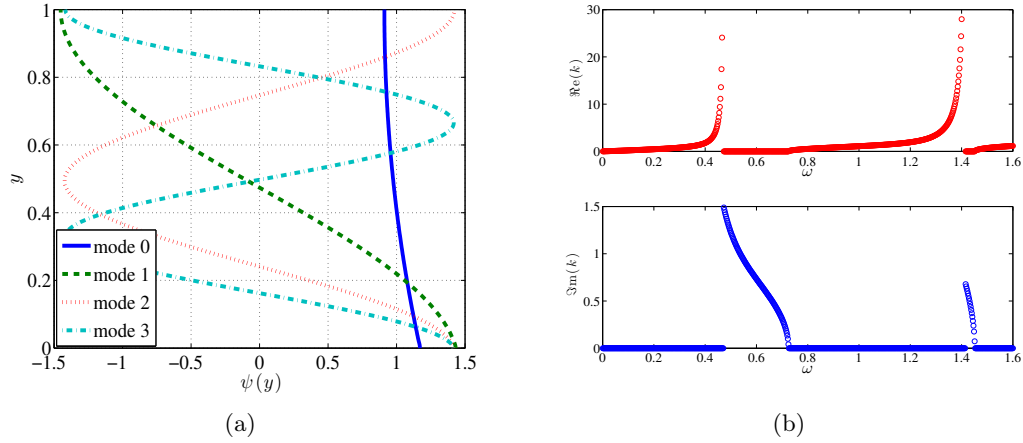


Figure 5.3: (a) The eigenfunction profiles of the first 4 transverse modes in the lined duct with $\omega = 0.3$ and $b = B/H = 50/15$ m, their eigenvalues are labelled by ‘ \times ’ in Fig. 5.2. (b) The real(upper) and imaginary(bottom) parts of the eigenvalue for the lowest mode in x -direction as a function of frequency ω .

5.2.2 Scattering matrix

For the sound propagation problem in the waveguide partially lined with a locally reacting liner, the scattering matrix S needs to be constructed to calculate the transmission coefficient. By using the previously obtained wavenumbers k and the eigenvectors X , the similar method as in Ref. [9] was used here to calculate the transmission coefficients and the pressure field. The configuration is shown in Fig. 5.4, the amplitudes of

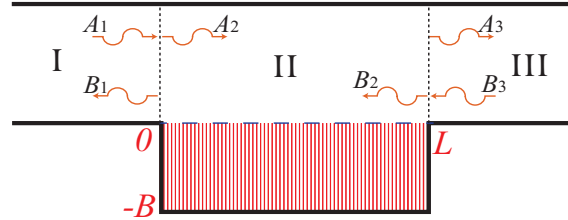


Figure 5.4: The configuration for constructing the scattering matrix, L is the length of the liner, normalized by duct width H , \vec{A}_i, \vec{B}_i ($i = 1, 2, 3$) are all vectors, indicating the pressure amplitude of each mode in $+x$ -direction and $-x$ -direction, respectively. The total pressure consists of the $+x$ and $-x$ -direction sound pressures.

the incoming waves, A_1 and B_3 , are linked to the amplitudes of outgoing waves, A_3 and B_1 , by a scattering matrix

$$\begin{pmatrix} \vec{A}_3 \\ \vec{B}_1 \end{pmatrix} = S \begin{pmatrix} \vec{A}_1 \\ \vec{B}_3 \end{pmatrix}, \quad \text{where } S = \begin{bmatrix} T & r \\ R & t \end{bmatrix}. \quad (5.15)$$

Being aware of the eigenvalues and the eigenvectors in Eq. (5.13), the pressure in the lined part can be written as a sum of the transverse modes in the lined duct,

$$p_2(x, y) = \vec{\Phi}^T \left[\mathbf{X}D^+(x)\vec{A}_2 + \mathbf{X}D^-(x)\vec{B}_2 \right], \quad (5.16)$$

where $D^+(x)$ and $D^-(x)$ are diagonal matrices with elements $e^{jk_n x}$ and $e^{-jk_n(x-L)}$, respectively, and \mathbf{X} is a matrix with the column vectors are eigenvectors X . For simplicity, we assume that there are multimodes incident from the left side of the waveguide, i.e. $B_3 = 0$. The sound pressures in regions I and III can be written as

$$p_1(x, y) = \vec{\Phi}^T \left[D_R(x)\vec{A}_1 + D_R(-x)\vec{B}_1 \right] \quad (5.17)$$

and

$$p_3(x, y) = \vec{\Phi}^T \left[D_R(x-L)\vec{A}_3 \right], \quad (5.18)$$

respectively, where $D_R(x)$ is diagonal matrix with elements $e^{jk_n^R x}$, and $k_n^R = \sqrt{(\omega^2 - \alpha_n^2)}$ are the axial wavenumbers in the rigid wall.

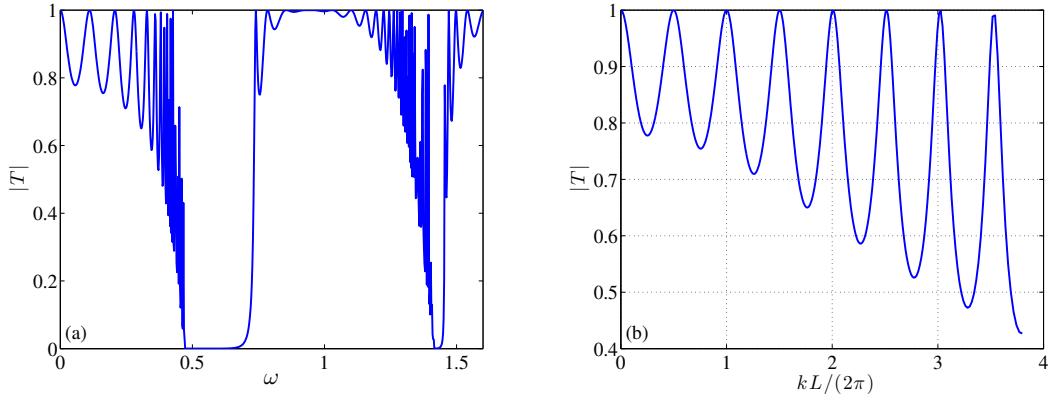


Figure 5.5: (a) Transmission coefficient of the plane mode as a function of (a) ω and (b) the ratio of the liner length L to the wavelength with $B = 50\text{mm}$, $H = 15\text{mm}$, $L = 200\text{mm}$ and $R = 0$. Figure (b) is corresponding to the range $0 < \omega < 0.4$ in figure (a).

As given in Appendix 5.B , we can have the transmission coefficient by

$$\mathbf{T} = \mathbf{t} = (\mathbf{F}\mathbf{D}_L - \mathbf{G}\mathbf{F}^{-1}\mathbf{G}\mathbf{D}_L)(\mathbf{F} - \mathbf{G}\mathbf{D}_L\mathbf{F}^{-1}\mathbf{G}\mathbf{D}_L)^{-1}, \quad (5.19)$$

where $\mathbf{D}_L = \mathbf{D}^+(L) = \mathbf{D}^-(0)$. Only plane wave is considered here, so the transmission coefficient is $\mathbf{T}(1, 1)$. The transmission coefficient as a function of frequency with $B = 50\text{mm}$, $H = 15\text{mm}$, $L = 200\text{mm}$ is shown in Fig. 5.5(a). It shows that there exists a specific frequency range, at which no wave can transmit through the lined part, the transmission coefficient is *zero*, it can also be revealed in the bottom figure of Fig. 5.3(b).

At the frequency around $\omega = 0.7$, the transmission coefficient starts to increase, and from Fig. 5.3(b) we can find that the mode appears again at that frequency. To see the effect of the liner length on the transmission behavior at low frequencies, we also plot the transmission coefficient as a function of the ratio of the length L to the wavelength in x direction, the results are shown in Fig. 5.5(b). We demonstrate that when the length L equals to the integer multiple of the half wavelength, the transmission coefficient achieves to maximum; When the length equals to the integer multiple of the quarter wavelength, the coefficient achieves to minimum. From Fig. 5.3(b), around the resonant frequency $\omega_R = 0.471$, the wavenumber k in x direction tends to be infinite, resulting in the wavelength $\lambda_x = \frac{2\pi}{k}$ tends to be *zero*, since $\lambda_x = \frac{c}{f_x}$, the oscillate frequency f_x tends infinite, as shown in Fig. 5.5(a).

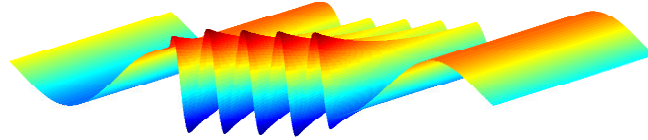


Figure 5.6: Pressure field distribution in the waveguide at $\omega = 0.412$ with $B = 50\text{mm}$, $H = 15\text{mm}$, and $L = 200\text{mm}$

From the pressure field distribution in the waveguide (see Fig. 5.6), we can find that the pressure field is concentrated on the liner, only surface wave is found, provided that the frequency is low enough that only plane wave exists in the rigid parts. Because of the rigid-lined interface, not all the sound can propagate through the lined part, some sound waves is reflected.

Thus in a lined duct with a purely reacting impedance, the sound propagates slower than in a rigid duct. It can be imagined that, if the sound is slow enough, a counter flow can stop the sound even if the Mach number is smaller than 1. That is what we are going to investigate in the next sections.

5.3 Propagation in the lined ducts with uniform flow

5.3.1 Basic equations

The problem considered in the present section is the sound propagation in an acoustic lined rectangular duct with the presence of fluid flow. To reduce the complexity of the problem, the geometry will be confined to two dimensions, and the mean shear flow will be in the x -direction and assumed to be only a function of y , as shown in Fig. 5.7. The upper wall ($y = H$) is rigid. The lower wall is treated with a purely locally liner for $0 < x < L$ and rigid elsewhere. Neglecting the viscosity, considering the isotropic fluid,

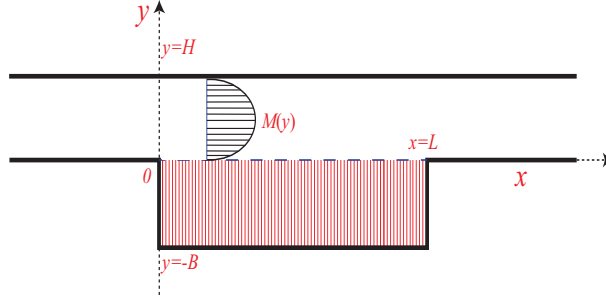


Figure 5.7: Geometry of the problem

the governing equations are written as follows:

$$\rho^* \frac{D\vec{v}^*}{Dt} = -\nabla \vec{p}^*, \quad \frac{1}{\rho^*} \frac{D\rho^*}{Dt} = -\vec{\nabla} \cdot \vec{v}^*, \quad c^2 \frac{D\rho^*}{Dt} = \frac{Dp^*}{Dt}, \quad (5.20)$$

where $\frac{D}{Dt} = \frac{\partial}{\partial t} + \vec{v} \cdot \vec{\nabla}$, ρ^* is the mass density, p^* is the pressure, \vec{v}^* is the velocity vector and c is the speed of sound. The acoustic equations are obtained by considering small perturbations on a mean state ρ_0, p_0 , and so that

$$\rho^* = \rho_0 + \rho, \quad p^* = p_0 + p,$$

and $\vec{v}^* = U(y)\vec{e}_x + u\vec{e}_x + v\vec{e}_y$, with \vec{e}_x, \vec{e}_y unit vectors in x - and y -direction, and $U(y)$ the shear flow profile.

At first order in the perturbation, the acoustics equations are

$$\frac{\partial u}{\partial t} + U \frac{\partial u}{\partial x} + v \frac{\partial U}{\partial y} = -\frac{1}{\rho_0} \frac{\partial p}{\partial x}, \quad (5.21)$$

$$\frac{\partial v}{\partial t} + U \frac{\partial v}{\partial x} = -\frac{1}{\rho_0} \frac{\partial p}{\partial y}, \quad (5.22)$$

$$\frac{1}{\rho_0 c_0^2} \left(\frac{\partial}{\partial t} + U \frac{\partial}{\partial x} \right) p = - \left(\frac{\partial u}{\partial x} + \frac{\partial v}{\partial y} \right). \quad (5.23)$$

The quantities are normalised by $p \rightarrow p/c_0^2$, $u, v \rightarrow u/c_0, v/c_0$, Mach number $M(y) = U(y)/c_0$, $t \rightarrow \frac{t}{H/c_0}$, and $\omega = \frac{2\pi f}{c_0} H$. We can obtain the dimensionless acoustic equations

$$\frac{D^2 p}{Dt^2} - \left(\frac{\partial^2 p}{\partial x^2} + \frac{\partial^2 p}{\partial y^2} \right) = 2 \frac{dM}{dy} \frac{\partial v}{\partial x}, \quad (5.24)$$

$$\frac{Dv}{Dt} = -\frac{\partial p}{\partial y}, \quad (5.25)$$

with

$$\frac{D}{Dt} = \left(\frac{\partial}{\partial t} + M \frac{\partial}{\partial x} \right). \quad (5.26)$$

If the pressure is written in the form of $p(x, y) = F e^{-j\omega t + jkx}$, then we can obtain the ordinary differential equation

$$\frac{d^2 F}{dy^2} + \frac{2kM'}{\omega - Mk} \frac{dF}{dy} + [(\omega - Mk)^2 - k^2] F = 0, \quad (5.27)$$

where prime “ ’ ” refers to the first derivative with respect to y . It is the well known Pridmore-Brown equation [10].

Concerning the boundary condition, for the lined wall in the presence of flow, we have to be careful, the effect of the boundary layer has to be considered. In the present work, the classical Ingard-Myers [5] [6] [8] boundary condition

$$\left. \frac{\partial p}{\partial y} \right|_{y=0} = \frac{D^2}{Dt^2} \left(\frac{Y}{-j\omega p} \right) \Big|_{y=0} \quad (5.28)$$

is used (see Appendix 5.C)

5.3.2 Uniform flow

With uniform flow, M is independent of y , then the governing equation Eq.(5.24) becomes more simple, the right term of the equal vanishes. The pressure can be projected on the complete basis of functions $\phi_n(y)$ which are transverse modes in the rigid duct. Thus, $p(x, y)$ can be written:

$$p(x, y) = \sum_{n=0}^{\infty} p_n(x) \phi_n(y) = \vec{\Phi}^T \vec{P},$$

where \vec{P} and $\vec{\Phi}$ are column vectors, with P the mode coefficients, and Φ the basis functions $\phi_n(y)$, which are given by Eq. (5.9).

Applying the same procedures as we did before (see Eqs. (5.11)(5.12)): substituting the pressure expression into the governing equation, Eq. (5.24), multiplying the resulting equation by $\vec{\Phi}$, integrating over the y axis, and using the boundary conditions, Eqs. (5.4)(5.28), we have

$$\frac{D^2}{Dt^2} \left(\vec{P} + \frac{Y(x)}{-j\omega} \mathbf{N}_1 \vec{P} \right) - \frac{\partial^2 \vec{P}}{\partial x^2} + \mathbf{N}_2 \vec{P} = 0, \quad (5.29)$$

where N_1, N_2 are shown as before in Sec. 5.2.1. Equation (5.29) can be written as

$$M_1 \frac{d^2 \vec{P}}{dx^2} = M_2 \frac{d\vec{P}}{dx} + M_3 \vec{P},$$

the above equation results in

$$\frac{d^2 \vec{P}}{dx^2} = M_1^{-1} M_2 \frac{d\vec{P}}{dx} + M_1^{-1} M_3 \vec{P}, \quad (5.30)$$

where $M_1 = 1 - M_0^2 \left(1 + \frac{Y}{-j\omega} N_1\right)$, $M_2 = -2j\omega M_0 \left(1 + \frac{Y}{-j\omega} N_1\right)$, $M_3 = \left[N_2 - \omega^2 \left(1 + \frac{Y}{-j\omega} N_1\right)\right]$. We define $\vec{Q} = \frac{d\vec{P}}{dx}$, then Eq. (5.30) can be written in a matrix form of

$$\frac{d}{dx} \begin{pmatrix} \vec{P} \\ \vec{Q} \end{pmatrix} = \begin{pmatrix} 0 & I \\ M_1^{-1} M_3 & M_1^{-1} M_2 \end{pmatrix} \begin{pmatrix} \vec{P} \\ \vec{Q} \end{pmatrix}, \quad (5.31)$$

where 0 and I are the zero and identity matrices.

By computing the eigenvalues λ_n and eigenvectors X_n of the matrix in Eq. (5.31), the wave numbers k of x -direction in the liner can be obtained by $k = -j\lambda_m$. Those wave numbers k and the eigenvectors are split into two sets: k^+ and X^+ when $\Im m(k) > 0$; k^- and X^- when $\Im m(k) < 0$.

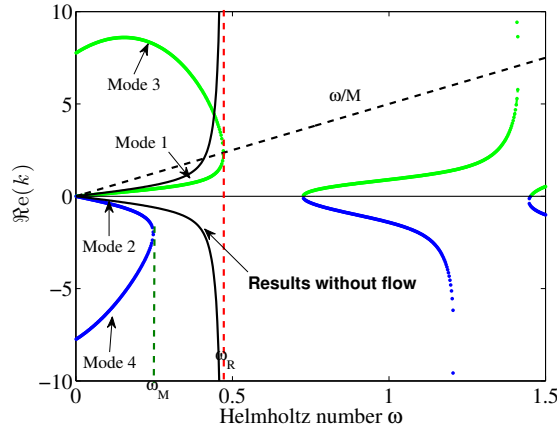


Figure 5.8: Variation of the propagative wave numbers k as a function of the Helmholtz number ω for $b = 10/3$ and $M_0 = 0.2$.

The propagative waves are of interest. The wave numbers with real values are only considered. They are divided into two sets: k^+ and k^- , the signs “+” and “-” indicate the propagation direction. The wavenumbers of the propagative modes as a function of ω are given in Fig. 5.8. It can be seen that the two positive real parts of Mode 1 and Mode 3 merge at the resonant frequency of the liner ($\omega = \omega_R$). When they merge, the

wave number is equal to ω/M . The two negative solutions, merge at a frequency ω_M which is lower than ω_R .

The Mode 1 and the Mode 2 are close to the 2 propagative waves without flow (solid lines). At low frequencies, their wavenumbers can be found by $k/\omega = \pm\sqrt{1+b}/(1 \mp \sqrt{1+b}M)$ which converges to the no-flow solution when $M \rightarrow 0$. Thus they can be seen as ‘‘acoustical modes’’. The other two modes (3 and 4) exist only with flow. The Mode 4 is a mode with a negative phase velocity but with a positive group velocity ($c_g = d\omega/dk$ is linked to the slope of the curves in Fig. 5.8). Thus this mode propagates in the positive direction (direction of the flow). At low frequencies, the phase and the group velocities of the mode 3 are positive and this mode also propagates in the positive direction. Aurégan and Pagneux [11] demonstrate that in this frequency range, this mode is a Negative Energy Wave.

It can be noticed that when $M > 1/\sqrt{1+b}$, the Mode 2 and 4 do not exist and in this case, only two waves going in the positive direction exist at low frequencies. It means that no wave can propagate against the flow even at very low frequencies.

The singular change between the case of a rigid duct (2 propagative waves) and the lined part of a duct (4 propagative waves) for low Mach number and low frequencies, can lead to mathematical problem when we try to compute the scattering of a finite length liner connected to two rigid ducts in the uniform flow case. To avoid these potential problems, we will study in the next section a shear flow with a vanishing velocity at the lined wall to avoid the use of the Ingard-Myers condition which is suspected to be responsible of this singular behavior.

5.4 Propagation in the lined ducts with shear flow

With the presence of shear flow, the governing equations are Eqs. (5.24)(5.25). For the sake of simplification, the flow profile we considered here is symmetrical about the central line of the duct, it can be expressed as

$$M(y) = M_0 \frac{2n+1}{2n} (1 - y^{2n}), \quad (5.32)$$

where the parameter n is used to regulate the gradient of the flow, the bigger n is, the closer the shear flow is to the uniform flow. The original point of the coordinate is located at the central line of the duct. All the length quantities in the geometry, see Fig. 5.7, are all normalized by half of the channel width, i.e. $H/2$, such that the dimensionless analytical width interval of the duct is $[-1, 1]$. An example of the flow profiles is given in Fig. 5.9 under different values of n with $M_0 = 0.2$.

The flow velocities on the walls are *zero*, resulting in the boundary condition on the

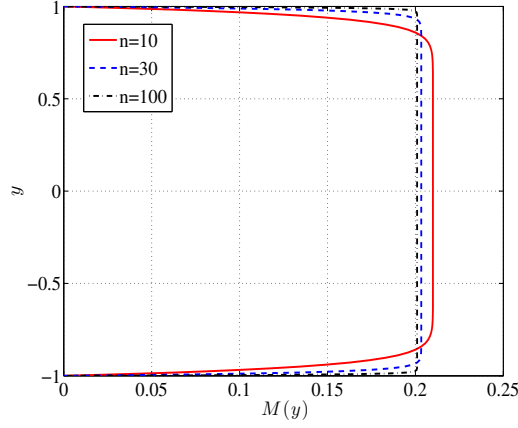


Figure 5.9: The profiles of the shear flow under different values of n in Eq. (5.32), with $M_0 = 0.2$.

lined wall

$$\left. \frac{\partial p}{\partial y} \right|_{y=-1} = -j\omega Y p|_{y=-1}. \quad (5.33)$$

Furthermore, harmonic waves in the x -direction are assumed, giving the following complex forms,

$$\begin{aligned} p &= P(y)e^{j(-\omega t + kx)}, \\ v &= V(y)e^{j(-\omega t + kx)}, \\ q &= Q(y)e^{j(-\omega t + kx)}, \end{aligned} \quad (5.34)$$

with

$$q = -j \frac{\partial p}{\partial x}, \quad (5.35)$$

where k is the dimensionless axial wavenumber.

The spectral method [12, 13] is proposed to solve the problem. Therefore, discretization in the y -coordinate is employed by the Chebyshev collocation points, the MATLAB program *chebdf.m* [13] generates these points for the interval $[-1, 1]$. The interpolation points on this interval are

$$y_i = \cos\left(\frac{(i-1)\pi}{N-1}\right), \quad i = 1, 2, \dots, N, \quad (5.36)$$

where N is the number of the discrete points in y -direction. We can note that these points in this interval are not evenly spaced but are clustered at the ends of the interval, which provides more detailed information near the wall.

Chebyshev points used to discretize an unknown function $f(y)$ interpolated at N

nodes $f(y_k)$ can be approximated by using interpolant polynomials $\phi_k(y)$:

$$f(x) \approx \sum_{k=1}^{N+1} f(x_k) \phi_k(y). \quad (5.37)$$

Thus, taking l th derivative of $f(y)$ and evaluating the result at the nodes y_i , results in

$$f(y_i)^{(l)} \approx \sum_{k=1}^N \frac{d^l}{dy^l} (\phi_k(y_i)) f(y_k). \quad (5.38)$$

The derivative operator may be represented by a matrix $D^{(l)}$, the differentiation matrix, with entries

$$D_{i,k}^{(l)} = \frac{d^l}{dy^l} (\phi_k(y_i)). \quad (5.39)$$

Finally, the numerical differentiation can be written as the matrix-vector product

$$\mathbf{f}^{(l)} = D^{(l)} \mathbf{f}. \quad (5.40)$$

Whereas differentiation matrices provided by Weideman and Reddy [13] are used to approximate the differential operator. Then Eqs. (5.24)(5.25)(5.35) can be written in the form of matrix

$$k \begin{pmatrix} 1 - M^2(y) & -2jM'(y) & 0 \\ 0 & jM(y) & 0 \\ 0 & 0 & 1 \end{pmatrix} \begin{pmatrix} \vec{Q} \\ \vec{V} \\ \vec{P} \end{pmatrix} = \begin{pmatrix} -2\omega M(y) & 0 & \omega^2 1 + D_2 \\ 0 & j\omega 1 & -D_1 \\ 1 & 0 & 0 \end{pmatrix} \begin{pmatrix} \vec{Q} \\ \vec{V} \\ \vec{P} \end{pmatrix}, \quad (5.41)$$

where 1 is the identity matrix. D_1 and D_2 are differential matrices giving the first respectively, second-order differential operator with respect to y , which can be obtained by Chebyshev polynomials interpolation [13]. $\vec{Q}, \vec{V}, \vec{P}$ are the column vectors whose elements are $Q(y_i), V(y_i)$, and $P(y_i)$, respectively.

In order to construct the eigenvalue problem, the boundary conditions are introduced in the matrix (5.41). The 1 th, $(N + 1)$ th, $(2N + 1)$ th rows of Eq. (5.41) indicate the rigid wall, while N th, $(2N)$ th, $(3N)$ th rows indicate the lined wall. The 1 th and N th rows are used to introduce rigid wall condition and lined wall condition, respectively.

5.4.1 Modes in the rigid duct with shear flow

For the rigid wall with $Y = 0$, the boundary conditions is

$$D_1 \mathbf{P}|_{y=1,-1} = 0. \quad (5.42)$$

By the combinations of the boundary condition and the matrix Eq. (5.41), we can obtain eigenvalues k and eigenvectors $\vec{Q}, \vec{V}, \vec{P}$ in which each column corresponds to each k . In total, 3 types of modes are found, which can generally be divided in acoustic modes propagating (or decaying) in the $+x$ -direction, acoustic modes propagating (or decaying) in the $-x$ -direction, and hydrodynamic modes in the direction of the mean flow. The effects of Mach number on the modes are shown in Figs. 5.10. It can be seen that the hydrodynamic modes depend significantly on the Mach number.

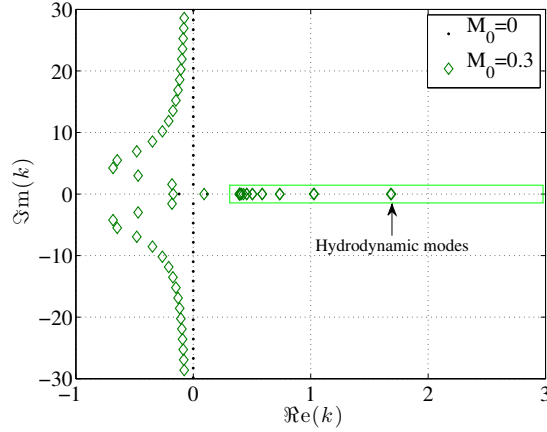


Figure 5.10: Axial wave numbers distributions in the complex k plane for different mach number M_0 with $\omega = 0.24$ and $n = 30$. The duct is rigid.

From Eq. (5.27), the hydrodynamic modes verifies $\omega - kM = 0$. As $M \in [0, M_{max}]$, it means that $k \in [\omega/M_{max}, \infty]$ and that the hydrodynamic modes form a continuum of mode that is discretized by taking a finite number of point N in the section.

5.4.2 Modes in the lined duct with shear flow

To study the modes in the lined duct with shear flow, the boundary conditions are applied to calculate the wave numbers in the lined duct. In vectorial form, the boundary conditions can be expressed as

$$D_1 \vec{P} \Big|_{y=1} = 0, \quad \text{and} \quad (D_1 + i\omega Y_1) \vec{P} \Big|_{y=-1} = 0, \quad (5.43)$$

where the admittance of the liner here is $Y = -j \tan(\omega b)$.

Performing a similar procedures as done for rigid duct with shear flow, the eigenvalues in the lined duct are shown below (Fig. 5.11). From the comparisons of Fig. 5.11 with Fig. 5.10, the first propagative modes in $+x$ and $-x$ -direction dependent significantly on the Mach number, this is because there exists the coupling between the flow and the liner.

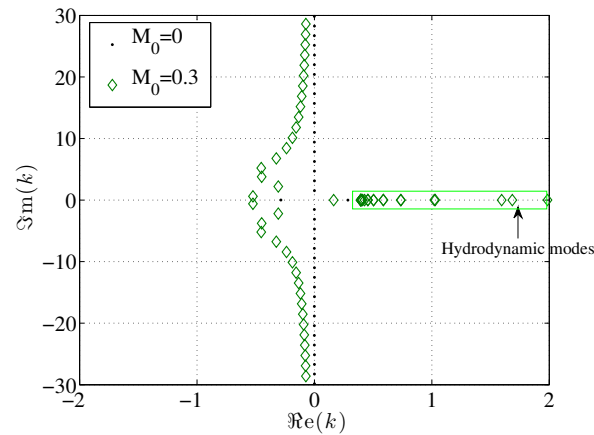


Figure 5.11: Axial wave numbers distributions in the complex k/ω plane for different mach number M_0 with $\omega = 0.24, n = 30$. The duct is lined.

5.4.3 The effect of the boundary layer thickness

The Mode 1 for which $0 < k < \omega/M_0$ is practically unchanged by the presence and the shape of the boundary layer. A big difference between the uniform and shear flow cases is the presence of a continuum of hydrodynamic modes. $k = \omega/M$ is a singular solution of Eq. (5.27) for all M between 0 and M_0 . Thus all $k > \omega/M_0$ are solutions of the hydrodynamic modes, and Mode 3 is now embedded in the continuum.

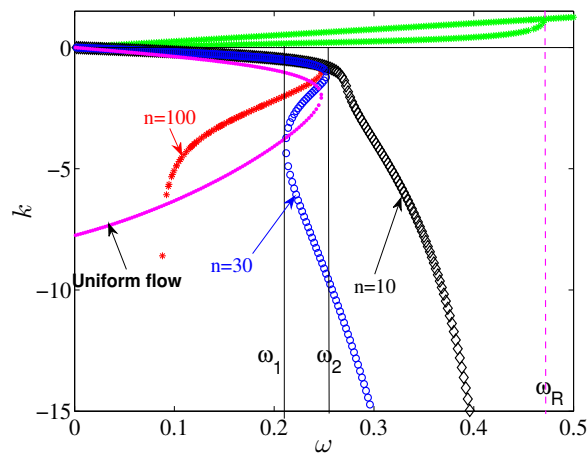


Figure 5.12: Wave number as a function of ω for 3 different values of n with $b = 10/3$ and $M_0 = 2$. The black “ \diamond ” indicates $n = 10$, the blue “ \circ ” $n = 30$, and the red “ $*$ ” $n = 100$. For comparison, the results with uniform flow are given by “.” The flow profiles for the three corresponding n are shown in Fig. 5.9.

The behavior of the propagative waves against the shear flow is further investigated. To have a comparison with Fig. 5.8, the wave number as a function of ω for 3 different values of n is plotted in Fig. 5.12. The waves propagating against the flow are very sensitive to the shape of the boundary layer. The number of propagative modes is changed by the effect of the boundary layer. This effect has been already noted by Brambley [14]. For the shear flow with $n = 30$, there is only one propagative mode for $0 < \omega < \omega_1$. This wave is close to the Mode 2 in Fig. 5.8 with uniform flow (also shown by “.” in Fig. 5.12). There are three propagative waves exist for $\omega_1 < \omega < \omega_2$. Two of them are close to the mode 2 and 4 in the uniform case and another wave appears with large value of k . For $\omega_2 < \omega < \omega_R$, there is only one wave with large ω .

By the definition of the group velocity $c_g = \frac{\partial \omega}{\partial k}$, we can find the group velocities at the two critical frequencies, ω_1 and ω_2 , are *zero*. The negative group velocity is also found for $n = 30$ and 100. As n increases, the shear flow profile tends to uniform flow, and the dispersion curve (the “*” in Fig. 5.12) becomes similar with the uniform flow case (the “.” in Fig. 5.12). When the boundary layer thickness increases (n decreases), the wave for which the group and the phase velocities are opposite in sign (Mode 4) will disappear (see the case $n = 10$ in Fig. 5.12). In this case, the points with a zero group velocity also disappear.

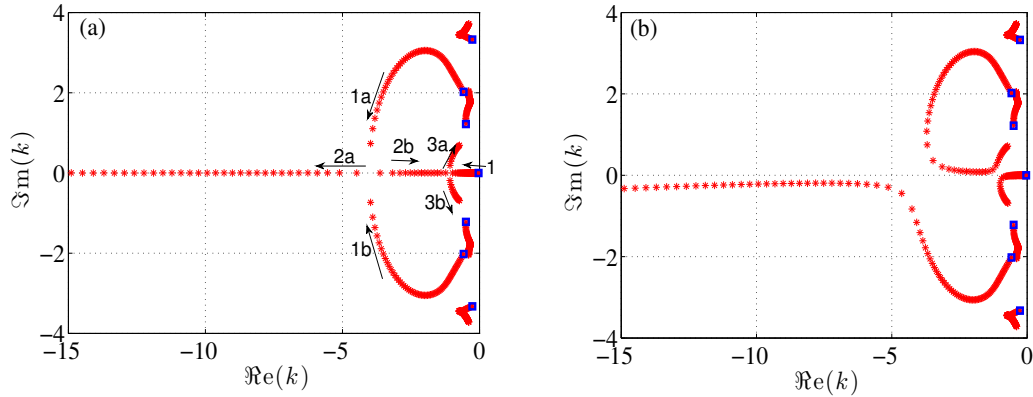


Figure 5.13: Trajectories of the waves propagate in $-x$ direction as a function of frequency, $0.02 < \omega < 0.3$. The \rightarrow indicates the moving direction of the waves, with “□” the starting point. The numbers “1”, “2”, and “3” indicate their emerging order. With the flow parameter $n = 30$ and $M_0 = 0.2$. Chebyshev points $N = 100$. (a) Without dissipation, (b) with dissipation, $Re = 0.01$.

Varying the frequency ω , trajectories of wave number for the wave in $-x$ -direction are plotted in complex k -plane, as shown in Fig. 5.13. By observing the movements, at low frequencies, one propagative mode exists (indicated by 1). With increasing the frequency, two evanescent modes (1a and 1b) move in opposite direction, and approach

to the $\Re(k)$ axial. At the critical frequency ω_1 , they have the same value. But then they repel each other, and split into two propagative modes (2a and 2b). Continuing increasing the frequency, two modes move along x -axis in opposite direction, shown as arrows 2a and 2b. When the frequency reach to another critical frequency ω_2 , the same phenomenon happens again, waves 1 and 2b meet and become evanescent modes 3a and 3b. Finally only one mode maintains (2a). The results are corresponding to Fig. 5.12, $n = 30$. Comparing Fig. 5.13(a) and (b), due to the consideration of the dissipation on the impedance, there exists obvious avoided crossing between the two modes.

5.4.4 Transmission and reflection in the lined liner with shear flow

We already calculated the transmission coefficient for the lined duct in the absence of flow, here we will study the effects of the shear flow on the transmission behavior. At the interfaces, i.e. $x = 0$ and $x = L$, the continuity of the pressure and normal velocity disturbance as well as continuity of the parameter $q = \frac{\partial p}{\partial x}$ are used to construct the scattering matrix.

The whole waveguide can be divided into 3 parts, the pressure expression in each part is consist of the incident and reflected waves, which can be written as

$$p_1 = \sum \vec{A}_1 \mathbf{P}_R^+ e^{jk_R^+ x} + \vec{B}_1 \mathbf{P}_R^- e^{jk_R^- x}, \quad (5.44)$$

$$p_2 = \sum \vec{A}_2 \mathbf{P}_Y^+ e^{jk_Y^+ x} + \vec{B}_2 \mathbf{P}_R^- e^{jk_Y^-(x-L)}, \quad (5.45)$$

and

$$p_3 = \sum \vec{A}_3 \mathbf{P}_R^+ e^{jk_R^+(x-L)} + \vec{B}_3 \mathbf{P}_R^- e^{jk_R^-(x-L)}, \quad (5.46)$$

respectively, where superscript “+” indicates the modes propagating in $+x$ -direction (acoustic and hydrodynamic), “-” the opposite.

The continuity conditions at the two interfaces are applied, for $x = 0$, we have

$$\mathbf{Q}_R^+ \vec{A}_1 + \mathbf{Q}_R^- \vec{B}_1 = \mathbf{Q}_Y^+ \vec{A}_2 + \mathbf{Q}_Y^- \mathbf{D}^- \vec{B}_2, \quad (5.47)$$

$$\mathbf{V}_R^+ \vec{A}_1 + \mathbf{V}_R^- \vec{B}_1 = \mathbf{V}_Y^+ \vec{A}_2 + \mathbf{V}_Y^- \mathbf{D}^- \vec{B}_2, \quad (5.48)$$

$$\mathbf{P}_R^+ \vec{A}_1 + \mathbf{P}_R^- \vec{B}_1 = \mathbf{P}_Y^+ \vec{A}_2 + \mathbf{P}_Y^- \mathbf{D}^- \vec{B}_2, \quad (5.49)$$

and

$$\mathbf{Q}_Y^+ \mathbf{D}^+ \vec{A}_2 + \mathbf{Q}_R^- \vec{B}_2 = \mathbf{Q}_R^+ \vec{A}_3 + \mathbf{Q}_R^- \vec{B}_3, \quad (5.50)$$

$$\mathbf{V}_Y^+ \mathbf{D}^+ \vec{A}_2 + \mathbf{V}_R^- \vec{B}_2 = \mathbf{V}_R^+ \vec{A}_3 + \mathbf{V}_R^- \vec{B}_3, \quad (5.51)$$

$$\mathbf{P}_Y^+ \mathbf{D}^+ \vec{A}_2 + \mathbf{P}_R^- \vec{B}_2 = \mathbf{P}_R^+ \vec{A}_3 + \mathbf{P}_R^- \vec{B}_3, \quad (5.52)$$

for $x = L$. \mathbf{D}^- and \mathbf{D}^+ are diagonal matrices with elements $\exp(-jk_Y^- L)$ and $\exp(jk_Y^+ L)$,

respectively. A relation between ingoing and outgoing waves can be constructed by

$$\underbrace{\begin{pmatrix} 0 & -Q_R^- & Q_Y^+ & Q_Y^- D^- \\ 0 & -V_R^- & V_Y^+ & V_Y^- D^- \\ 0 & -P_R^- & P_Y^+ & P_Y^- D^- \\ -Q_R^+ & 0 & Q_Y^+ D^+ & Q_Y^- \\ -V_R^+ & 0 & V_Y^+ D^+ & V_Y^- \\ -P_R^+ & 0 & P_Y^+ D^+ & P_Y^- \end{pmatrix}}_{S_1} \begin{pmatrix} A_3 \\ B_1 \\ A_2 \\ B_2 \end{pmatrix} = \underbrace{\begin{pmatrix} Q_R^+ & 0 \\ V_R^+ & 0 \\ P_R^+ & 0 \\ 0 & Q_R^- \\ 0 & V_R^- \\ 0 & P_R^- \end{pmatrix}}_{S_2} \begin{pmatrix} A_1 \\ B_3 \end{pmatrix}. \quad (5.53)$$

The transmission and reflection coefficients of the plane wave can be obtained by the matrix $S = S_1^{-1} S_2$. They are defined by

$$T^+ = \frac{A_3}{A_1}, \quad R^+ = \frac{B_1}{A_1}, \quad T^- = \frac{B_1}{B_3}, \quad \text{and} \quad R^- = \frac{A_3}{B_3}. \quad (5.54)$$

From the upper definitions and the matrix S , the propagation behavior is discussed. Figure 5.14 shows an example of the transmission and reflection coefficients of the plane wave as a function of frequency f , with $M_0 = 0.3$, $n = 30$, $L = 200\text{mm}$, and $B = 50\text{mm}$. The height of the duct is $H = 15\text{mm}$. The dissipation of the impedance is considered by taking $Re = 0.1$. In Fig. 5.15, the mach number M_0 and the resistance Re are changed, the experimental results are also shown in the same figure.

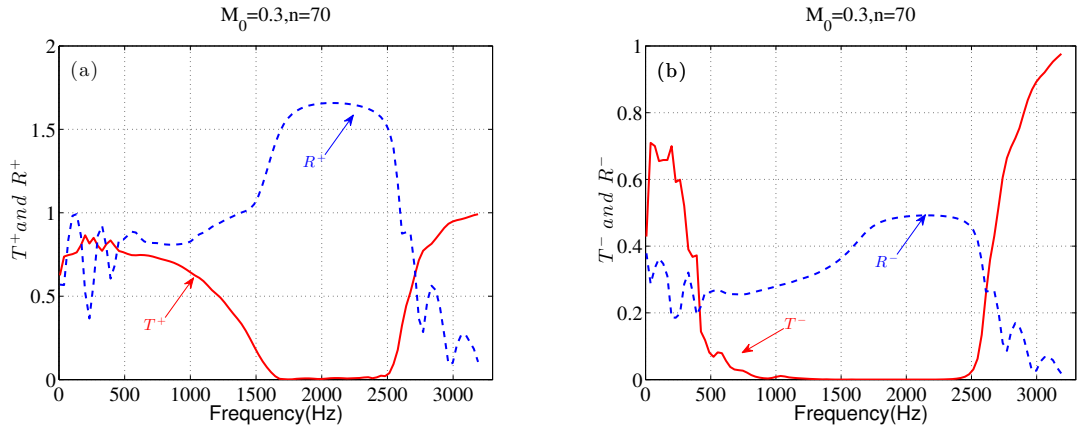


Figure 5.14: Absolute values of the transmission and reflection coefficients of the plane wave with $M_0 = 0.3$, $n = 70$ and $Re = 0.1$.

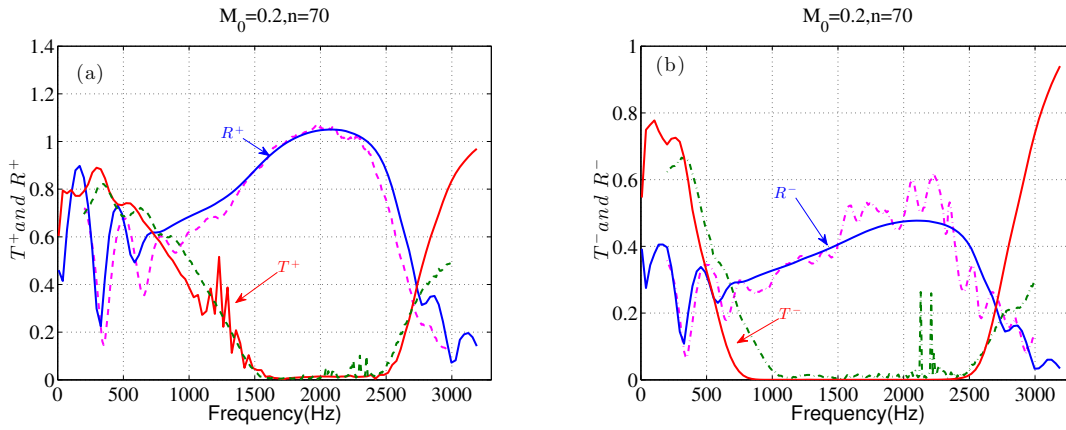


Figure 5.15: Absolute values of the transmission and reflection coefficients of the plane wave with $M_0 = 0.2$, $n = 70$ and $Re = 0.3$. Solid line: computation results; dashed line: experimental results.

5.5 Conclusion

The modes in a duct lined with locally reacting liner are computed and discussed, in both absence and presence of flow. The purely reacting liners produce surface waves which are concentrated along the liner. When a uniform flow is added the waves that propagate against the flow can be cut off. This will produce a large frequency band with transmission zero. Hydrodynamic modes are also observed. In the presence of shear flow, at a specific frequency band $[\omega_1, \omega_2]$, there are three propagative modes against the flow direction. Negative group velocity can be induced. What the most important is, at the two critical frequencies, the group velocity is *zero*. This phenomenon is very sensitive to the thickness of the boundary layer. For the wave propagates through a lossless medium, the group velocity can be thought as the the velocity at which energy is conveyed along the wave. So it indicates that the energy cannot propagate, which might be used to slow down and even stop the sound.

Appendix

5.A The admittance of the liner

The liner we considered here is a honeycomb layer which is locally reactive and backed by a rigid wall. In the single tube, the pressure satisfies the Helmholtz equation

$$\frac{\partial^2 p(y)}{\partial y^2} + \omega^2 p(y) = 0, \quad (5.55)$$

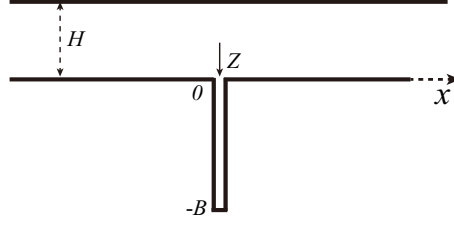


Figure 5.16: The geometry of the problem.

where $\omega = 2\pi fH/c_0$ is the normalised frequency. In the following, all quantities are non-dimensionalized: lengths with the waveguide height H , velocities with sound speed c_0 , densities with the ambient density ρ_0 , and pressures with $\rho_0 c_0^2$. Time dependence is $\exp(-j\omega t)$.

The solution of the above equation can be written as

$$p(y) = C_1 \cos(\omega y) + C_2 \sin(\omega y). \quad (5.56)$$

Since

$$\frac{\partial v}{\partial t} = -\frac{\partial p}{\partial y},$$

we have the expression of the acoustic velocity

$$\mathbf{v} = \frac{1}{j\omega} (-C_1 \omega \sin(\omega y) + C_2 \omega \cos(\omega y)). \quad (5.57)$$

Here $v(y)$ is in $+y$ -direction. At the bottom of the tube, i.e. $y = -b = -B/H$, where $B = 50\text{mm}$ is the thickness of the liner, the velocity vanishes, namely $v(-b) = 0$. This results in

$$\frac{C_1}{C_2} = -\frac{1}{\tan(\omega b)}. \quad (5.58)$$

For a locally reacting liner, its impedance Z is expressed as

$$Z = \frac{p(y)}{\mathbf{v} \cdot \mathbf{n}}, \text{ at } y = 0, \quad (5.59)$$

where \mathbf{n} is the outward normal vector pointing into the liner. By Eqs. (5.56)(5.57)(5.58), the impedance without dissipation can be written as

$$Z(\omega) = j \cot(\omega b). \quad (5.60)$$

5.B Scattering matrix S

The amplitudes of incoming waves \vec{A}_1, \vec{B}_3 are linked to the amplitudes of the outgoing waves \vec{A}_3, \vec{B}_1 by a scattering matrix,

$$\begin{pmatrix} \vec{A}_3 \\ \vec{B}_1 \end{pmatrix} = \mathbf{S} \begin{pmatrix} \vec{A}_1 \\ \vec{B}_3 \end{pmatrix}, \quad \text{where } \mathbf{S} = \begin{bmatrix} \mathbf{T} & \mathbf{r} \\ \mathbf{R} & \mathbf{t} \end{bmatrix}. \quad (5.61)$$

In order to solve the matrix, Mode-Matching method is proposed. Multiplying Eqs. (5.16) (5.17) (5.18) by $\vec{\Phi}$, we can obtain the corresponding equations as below

$$x \leq 0 \quad \vec{P}_1 = \mathbf{D}_R(x)\vec{A}_1 + \mathbf{D}_R(-x)\vec{B}_1, \quad (5.62)$$

$$0 < x \leq L \quad \vec{P} = \mathbf{X}\mathbf{D}^+(x)\vec{A}_2 + \mathbf{X}\mathbf{D}^-(x)\vec{B}_2, \quad (5.63)$$

$$x > L \quad \vec{P}_3 = \mathbf{D}_R(x-L)\vec{A}_3 + \mathbf{D}_R(L-x)\vec{B}_3. \quad (5.64)$$

where $\mathbf{D}^+(x)$, $\mathbf{D}^-(x)$ and $\mathbf{D}_R(x)$ are diagonal matrices with elements $e^{jk_n x}$, $e^{-jk_n(x-L)}$ and $e^{jk_n^R x}$, respectively, and \mathbf{X} is matrix with columns the eigenvectors in Eq. (5.13)

Using the continuity conditions of the pressure and velocity at $x = 0$ and $x = L$, we can have

$$\vec{A}_1 + \vec{B}_1 = \mathbf{X}(\vec{A}_2 + \mathbf{D}_L\vec{B}_2), \quad (5.65)$$

$$\mathbf{K}_R(\vec{A}_1 - \vec{B}_1) = \mathbf{X}\mathbf{K}_Y(\vec{A}_2 - \mathbf{D}_L\vec{B}_2), \quad (5.66)$$

$$\vec{A}_3 + \vec{B}_3 = \mathbf{X}(\mathbf{D}_L\vec{A}_2 + \vec{B}_2), \quad (5.67)$$

$$\mathbf{K}_R(\vec{A}_3 - \vec{B}_3) = \mathbf{X}\mathbf{K}_Y(\mathbf{D}_L\vec{A}_2 - \vec{B}_2). \quad (5.68)$$

where $\mathbf{D}_L = \mathbf{D}^+(L) = \mathbf{D}^-(0)$, and \mathbf{K}_R , \mathbf{K}_Y are diagonal matrices with elements the axial wave numbers k_n^R and k_n , respectively.

Since the duct is infinite and symmetric about x , we can have $\mathbf{T} = \mathbf{t}$ and $\mathbf{R} = \mathbf{r}$. For simplicity, we assume that there are only multimodes incident from the left side, i.e. $\vec{B}_3 = 0$. We denote

$$\mathbf{F} = \mathbf{X} + \mathbf{K}_R^{-1}\mathbf{X}\mathbf{K}_Y,$$

$$\mathbf{G} = \mathbf{X} - \mathbf{K}_R^{-1}\mathbf{X}\mathbf{K}_Y.$$

From Eqs. (5.67)(5.68), we have

$$\vec{B}_2 = -\mathbf{F}^{-1}\mathbf{G}\mathbf{D}_L\vec{A}_2. \quad (5.69)$$

By the summations of Eqs. (5.75) and (5.76) and of Eqs. (5.67) and (5.68), with the help of Eq.(5.69), we obtain

$$2\vec{A}_1 = (\mathbf{F} - \mathbf{G}\mathbf{D}_L\mathbf{F}^{-1}\mathbf{G}\mathbf{D}_L)\vec{A}_2, \quad (5.70)$$

$$2\vec{A}_3 = (\mathbf{F}\mathbf{D}_L - \mathbf{G}\mathbf{F}^{-1}\mathbf{G}\mathbf{D}_L)\vec{A}_2. \quad (5.71)$$

Finally, we can have the transmission matrix $\mathbf{T}(\mathbf{t})$ by

$$\mathbf{T} = \mathbf{t} = (\mathbf{F}\mathbf{D}_L - \mathbf{G}\mathbf{F}^{-1}\mathbf{G}\mathbf{D}_L)(\mathbf{F} - \mathbf{G}\mathbf{D}_L\mathbf{F}^{-1}\mathbf{G}\mathbf{D}_L)^{-1}. \quad (5.72)$$

By the difference of Eq.(5.75) and Eq.(5.76), with the help of Eq.(5.69), we can have

$$2\mathbf{B}_1 = (\mathbf{G} - \mathbf{F}\mathbf{D}_L\mathbf{F}^{-1}\mathbf{G})\mathbf{A}_2, \quad (5.73)$$

it results in

$$\mathbf{R} = \mathbf{r} = (\mathbf{G} - \mathbf{F}\mathbf{D}_L\mathbf{F}^{-1}\mathbf{G})(\mathbf{F} - \mathbf{G}\mathbf{D}_L\mathbf{F}^{-1}\mathbf{G}\mathbf{D}_L)^{-1}. \quad (5.74)$$

5.C Ingard-Myers boundary condition

The expression of the impedance is given in Eq. (5.59). As there is no flow at the lined wall, v is linked to the acoustic displacements δ_w at the wall by

$$\mathbf{v} \cdot \mathbf{n} = \frac{\partial \delta_w}{\partial t} \cdot \mathbf{n}, \text{ at } y = 0. \quad (5.75)$$

Assuming a thin shear layer close to the lined wall, the continuity conditions of the normal displacement and the acoustic pressure across the boundary layer need to be considered. Then, the transverse kinematic condition is written as

$$\begin{aligned} \mathbf{v}_\varepsilon \cdot \mathbf{n} &= \left(\frac{\partial}{\partial t} + M \frac{\partial}{\partial x} \right) \delta_\varepsilon \cdot \mathbf{n} \\ &= \left(\frac{\partial}{\partial t} + M \frac{\partial}{\partial x} \right) \delta_w \cdot \mathbf{n}, \end{aligned} \quad (5.76)$$

where \mathbf{v}_ε and δ_ε denote the velocity and the displacement just above the thin boundary layer. From Eqs. (5.59)(5.75), we can have

$$\delta_w \cdot \mathbf{n} = \frac{1}{-j\omega Z} p.$$

When the thickness of the layer tends to zero, then $\mathbf{v}(x, y = 0) \cdot \mathbf{n} \rightarrow \mathbf{v}_\varepsilon \cdot \mathbf{n}$ and $p(0) \rightarrow p_\varepsilon = p_w$ leading to the lined wall boundary condition

$$\mathbf{v}(x, y = 0) \cdot \mathbf{n} = \left(\frac{\partial}{\partial t} + M \frac{\partial}{\partial x} \right) \left(\frac{Y}{-j\omega} p(x, 0) \right), \quad (5.77)$$

where $-j\omega$ refers to the time derivative for an harmonic time dependence $e^{-j\omega t}$. Using the Euler equation in the y -direction, results in the boundary condition Eq. (5.28).

Bibliography

- [1] Y. Aurégan and M. Leroux. Experimental evidence of an instability over an impedance wall in a duct with flow. *Journal of Sound and Vibration*, 317(3-5):432–439, November 2008.
- [2] David Marx, Yves Aurégan, Hélène Bailliet, and Jean-Christophe Valière. PIV and LDV evidence of hydrodynamic instability over a liner in a duct with flow. *Journal of Sound and Vibration*, 329(18):3798–3812, August 2010.
- [3] Sjoerd W. Rienstra. A classification of duct modes based on surface waves. *Wave Motion*, 37(2):119 – 135, 2003.
- [4] E.J. Brambley and N. Peake. Classification of aeroacoustically relevant surface modes in cylindrical lined ducts. *Wave Motion*, 43(4):301–310, April 2006.
- [5] M.K. Myers. On the acoustic boundary condition in the presence of flow. *Journal of Sound and Vibration*, 71(3):429–434, August 1980.
- [6] Uno Ingard. Influence of Fluid Motion Past a Plane Boundary on Sound Reflection, Absorption, and Transmission. *The Journal of the Acoustical Society of America*, 31(7):1035, 1959.
- [7] Yves Aurégan, Rudolf Starobinski, and Vincent Pagneux. Influence of grazing flow and dissipation effects on the acoustic boundary conditions at a lined wall. *The Journal of the Acoustical Society of America*, 109(1):59–64, January 2001.
- [8] Ygäl Renou and Yves Aurégan. Failure of the Ingard–Myers boundary condition for a lined duct: An experimental investigation. *The Journal of the Acoustical Society of America*, 130(1):52, 2011.
- [9] W.P. Bi, V. Pagneux, D. Lafarge, and Y. Aurégan. Modelling of sound propagation in a non-uniform lined duct using a Multi-Modal Propagation Method. *Journal of Sound and Vibration*, 289(4-5):1091–1111, February 2006.
- [10] D. C. Pridmore-Brown. Sound propagation in a fluid flowing through an attenuating duct. *Journal of Fluid Mechanics*, 4(04):393, August 1958.

-
- [11] Yves Aurégan and Vincent Pagneux. Slow sound in lined flow ducts. *The Journal of the Acoustical Society of America*, 138(2):605–613, 2015.
- [12] A. T. I. Adamou and R. V. Craster. Spectral methods for modelling guided waves in elastic media. *The Journal of the Acoustical Society of America*, 116(3):1524, 2004.
- [13] J. A. C. Weideman and S. C. Reddy. A MATLAB differentiation matrix suite. *ACM Transactions on Mathematical Software*, 26(4):465–519, December 2000.
- [14] E.J. Brambley. Surface modes in sheared boundary layers over impedance linings. *Journal of Sound and Vibration*, 332(16):3750 – 3767, 2013.

Chapter 6

Conclusions

In this thesis, two different strategies are presented to enhance the sound attenuation in acoustic ducts by using the mode coupling effects. Trapped mode and transmission loss peak are observed near the avoided crossing of eigenvalues between two neighbored (Bloch) modes. We have shown that this avoided crossing is closely related to the Exceptional Point in the parameter plane.

First, the wave propagation problems in an acoustic duct-cavity system and a waveguide with a portion of its wall lined by a locally reacting material is studied by the R-matrix method. We have shown that the acoustic scattering matrix can be efficiently described with the help of an effective matrix \mathbf{H}_{eff} , whose eigenvalues give the poles of the scattering matrix. The real poles are in the vicinity of the exceptional points of matrix \mathbf{H}_{eff} . Using this effective matrix, the original acoustic resonances problem in the infinite waveguide is reduced to an equivalent eigenvalue problem of matrix \mathbf{H}_{eff} , which describes the eigenvalue problem defined in the scattering region. When a plane mode is incident, a transmission zero is present when the real resonance frequency is equal to the incident frequency. This transmission zero occurs - due to the interference of the incoming propagative mode with the trapped mode, which is also called the Fano resonance. This is the idea of the first strategy. The trapped mode is formed by the interferences of two neighbored modes with complex resonance frequencies. With the aid of the eigenvalues and eigenfunctions of matrix \mathbf{H}_{eff} , the traditional acoustic resonance scattering formula is extended to include the coupling effects between the scattering region and the rigid parts of the waveguide.

Second, the mode coupling due to the embedment of the rigid inclusions in the porous material is used to enhance the sound attenuation in an acoustic lined duct at low frequencies. This strategy is validated numerically and experimentally in a 3D waveguide lined with periodic inclusions embedded in porous material. Two different inclusion shapes are considered, an open cylinder and a Helmholtz resonator. When rigid inclusions are embedded in the porous material, the low frequency behaviours of the transmission loss can be significantly changed, peaks are observed in the mid-frequency

range. The effects of the inclusion position on the frequency of the TL peak are different for different inclusion shapes. Good agreements are observed between the experimental and numerical results, which opens the way to the optimisation of metaporous material for better sound attenuation at low frequencies.

An analysis of a 2D infinite periodic waveguide with inclusions embedded in porous material is performed by using Floquet-Bloch theorem. A maximum sound attenuation for this infinite periodic waveguide can be reached near the crossing (or avoided crossing) of the mode attenuations between two lower Bloch waves, and it is related to the exceptional point. A coupling between acoustic mode and localized mode is happened near this crossing.

Finally, the acoustical behaviors of a purely reacting liner in a rectangular duct in both absence and presence of flow are investigated. Multi-Model Method is proposed to solve the problem in the absence and presence of uniform flow. The results exhibit an unusual acoustical behavior: for a certain range of frequencies, no wave can propagate against the flow. The effect of shear flow is investigated by the Chebyshev Spectral Method, which provides detailed information near the walls. A negative group velocity is found in a certain range of frequencies, and it is demonstrated that the sound can be slowed down and even stopped.



THÈSE DE DOCTORAT

Lei XIONG

Use of mode coupling to enhance sound attenuation in acoustic ducts

Résumé

Deux stratégies sont présentées à utiliser des effets de couplage de modes pour l'amplification de l'atténuation du son dans les conduits acoustiques. La première est de coupler le mode incident propagatif avec un mode localisé, aussi appelé résonance de Fano. Cette stratégie est présentée et validée dans un système conduit-cavité et un guide d'onde partiellement traité en paroi avec un matériau à réaction locale. La méthode "R-matrix" est introduite pour résoudre le problème de propagation d'onde. Une annulation de la transmission se produit quand un mode piégé (qui est formé par les interférences de deux modes voisins) est excité dans le système ouvert. Ce phénomène est aussi lié au croisement évité des valeurs propres et à un point exceptionnel. Dans la seconde stratégie, un réseau d'inclusions rigides périodiques est intégré dans une couche poreuse pour améliorer l'atténuation du son à basse fréquence. Le couplage de modes est dû à la présence de ces inclusions. Le théorème de Floquet-Bloch est proposé pour analyser l'atténuation du son dans un guide d'onde périodique en 2D. Un croisement de l'atténuation de deux ondes de Bloch est observé. Ce phénomène est utilisé pour expliquer le pic de pertes en transmission observé expérimentalement et numériquement dans un guide 3D partiellement traité par un matériau poreux avec des inclusions périodiques. Enfin, le comportement acoustique d'un liner purement réactif dans un conduit rectangulaire avec et sans écoulement est étudié. Dans une certaine gamme de fréquence, aucune onde ne peut se propager à contre sens de l'écoulement. Par analyse des différents modes à l'aide de la relation de dispersion, il est démontré que le son peut être ralenti et même arrêté.

Mots clés

Méthode R-matrix, Mode piégé, Résonance de Fano, Croisement évité, Point exceptionnel, Atténuation du son, Ondes de Bloch, Son lent

Abstract

Two strategies are presented to use the mode coupling effects to enhance sound attenuation in acoustic ducts. The strategy is to couple the incoming propagative mode with the localized mode, which is also called Fano resonance. This strategy is presented and validated in a duct-cavity system and a waveguide partially lined with a locally reacting material. The R-matrix method is introduced to solve the propagation problems. A zero in the transmission is present, due to the excitation of a trapped mode which is formed by the interferences of two neighbored modes. It is also linked to the avoided crossing of the eigenvalues and exceptional point. In the second strategy, a set of periodic rigid inclusions are embedded in a porous lining to enhance sound attenuation at low frequencies. The mode coupling is due to the presence of the embedded inclusions. Floquet - Bloch theorem is proposed to investigate the attenuation in a 2D periodic waveguide. Crossing is observed between the mode attenuations of two Bloch waves. The most important and interesting figure is that near the frequency where the crossing appears, an attenuation peak is observed. This phenomenon can be used to explain the transmission loss peak observed numerically and experimentally in a 3D waveguide partially lined by a porous material embedded with periodic inclusions. Finally, the acoustical behaviours of a purely reacting liner in a duct in absence and presence of flow are investigated. The results exhibit an unusual acoustical behaviour : for a certain range of frequencies, no wave can propagate against the flow. a negative group velocity is found, and it is demonstrated that the sound can be slowed down and even stopped.

Key Words

R-matrix method, Trapped mode, Fano resonance, Avoided crossing, Exceptional point, Sound attenuation, Bloch wave, Slow sound